Continuous-Flow Synthesis and Materials Interface Engineering of Lead Sulfide Quantum Dots for Photovoltaic Applications

Dissertation by

Ala'a O. El-Ballouli

In Partial Fulfillment of the Requirements

For the Degree of

Doctor of Philosophy

King Abdullah University of Science and Technology

Thuwal, Kingdom of Saudi Arabia

The dissertation of Ala'a O. El-Ballouli is approved by the examination committee.

Committee Chairperson Prof. Osman Bakr

Committee Member Prof. Omar Mohammed

Committee Member Prof. Enzo Difabrizio

Committee Member Prof. Irshad Hussain

ABSTRACT

Continuous-Flow Synthesis and Materials Interface Engineering of Lead Sulfide Quantum Dots for Photovoltaic Applications

Ala'a O. El-Ballouli

Harnessing the Sun's energy via the conversion of solar photons to electricity has emerged as a sustainable energy source to fulfill our future demands. In this regard, solution-processable, size-tunable PbS quantum dots (QDs) have been identified as a promising active materials for photovoltaics (PVs). Yet, there are still serious challenges that hinder the full exploitation of QD materials in PVs. This dissertation addresses two main challenges to aid these QDs in fulfilling their tremendous potential in PV applications.

First, it is essential to establish a large-scale synthetic technique which maintains control over the reaction parameters to yield QDs with well-defined shape, size, and composition. Rigorous protocols for cost-effective production on a scale are still missing from literature. Particularly, previous reports of record-performance QD-PVs have been based on small-scale, manual, batch syntheses. One way to achieve a controlled large-scale synthesis is by reducing the reaction volume to ensure uniformity. Accordingly, we design a droplet-based continuous-flow synthesis of PbS QDs. Only upon separating the nucleation and growth phases, *via* a dual-temperature-stage reactor, it was possible to achieve high-quality QDs with high photoluminescence quantum yield (50%) in large-scale. The performance of these QDs in a PV device was comparable to batch-

synthesized QDs, thus providing a promise in utilizing automated synthesis of QDs for PV applications.

Second, it is crucial to study and control the charge transfer (CT) dynamics at QD interfaces in order to optimize their PV performance. Yet, the CT investigations based on PbS QDs are limited in literature. Here, we investigate the CT and charge separation (CS) at size-tunable PbS QDs and organic acceptor interfaces using a combination of femtosecond broadband transient spectroscopic techniques and steady-state measurements. The results reveal that the energy band alignment, tuned by the quantum confinement, is a key element for efficient CT and CS processes. Additionally, the presence of interfacial electrostatic interaction between the QDs and the acceptors facilitates CT from large PbS QD (bandgap < 1 eV); thus enabling light-harvesting from the broad near-infrared solar spectrum range.

The advances in this work– from automated synthesis to charge transfer studies– pave new pathways towards energy harvesting from solution-processed nanomaterials.

ACKNOWLEDGEMENTS

I would like to take this opportunity to thank all those who helped and supported me throughout my years of Ph.D. study. I am thankful to my advisors, Prof. Osman Bakr and Prof. Omar Mohammed, for their assistance, guidance and valuable suggestions that have contributed greatly to the completion of this endeavor. I would also like to acknowledge Prof. Enzo Difabrizio and Prof. Irshad Hussain for their helpful feedback.

I am indebted to the efforts of our collaborators, Prof. Edward Sargent and his team members from the University of Toronto; Prof. Alain Goriely and Dr. Victor Burlakov from the University of Oxford; Prof. Marco Bernardi from the University of California at Berkeley; and Prof. Aram Amassian, Dr. Errki Alarouso, Dr. Jun Pan, Dr. Alec LaGrow, Dr. Ahmed Abdelhady and Ahmad Kirmani from King Abdullah University of Science and Technology (KAUST). I highly appreciate the efforts of the lab managers and staff of the Solar and Photovoltaic Research Center and Core Laboratories; for serving research at KAUST and providing training and maintenance for various instruments and equipment. Additionally, I present my sincere thanks to FuNL group members and to my friends at KAUST for making my years here a great memorable experience.

Furthermore, I owe my deepest gratitude to my caring parents, my loving husband, and my thoughtful siblings for their continuous encouragement, patience, and support. Their great confidence in me was always a vast impulsion in my academic life. Thank you all for your support and inspiration; this dissertation in every bit is as much your accomplishment as it is mine.

TABLE OF CONTENTS

LIST OF ABBREVIATIONS

Abs	absorbance
AM1.5G	air mass 1.5 global
ASTM	American Society for Testing and Materials
CB	conduction band
CR	charge recombination
CS	charge separation
CT	charge transfer
DMSO	Dimethyl sulfoxide
DMSO-d_6	deuterated dimethyl sulfoxide
EQE	external quantum efficiency
ESA	Excited State Absorption
FF	fill factor
fs	femtosecond
FTO	fluorine-doped tin oxide
FWHM	full-width-at-half-maximum
GSB	Ground State Bleach
HWHM	half-width-at-half-maximum
I-V	current-voltage
ITO	tin-doped indium oxide
MEG	multiple exciton generation
MPA	3-mercaptopropionic acid
MPP	maximum power point
NCs	nanocrystals
NREL	National Renewable Energy Laboratory
NIR	near-infrared
OA	oleic acid
OD	optical density
ODE	1-octadecene
PCBM	phenyl-C_{61}-butyric acid methyl ester
PCE	power conversion efficiency
PFA	perfluoroalkoxy
PL	photoluminescence
PLQE	photoluminescence quantum efficiency
ps	picosecond
PTFE	polytetrafluoroethyelene
PV	photovoltaic
QDs	quantum dots
SV	Stern-Volmer plot
VB	valence band
TA	Transient absorption

TDPA	tetradecylphosphonic acid
TG	Thioglycerol
TMPyP	tetra(N-methyl-4-pyridyl)porphyrin tetrachloride
TMS	bis(trimethylsilyl) sulfide
TPyP	tetra(4-pyridyl)porphyrin
TEM	Transmission electron microscopy
UHV	ultrahigh vacuum
UPS	Ultraviolet photoelectron spectroscopy
WLC	white light continuum
XPS	X-ray photoelectron spectroscopy

LIST OF SYMBOLS

a_b	exciton bohr radius
d	diameter
E_g	bandgap
ε	dielectric constant
e	elementary charge
$\hbar$	Dirac's constant
τ	carrier lifetime
λ	wavelength
R_c	critical radius
t	time
T_N	nucleation temperature
T_G	growth temperature
t_R	residence time
V_{oc}	open-circuit voltage
V_{MPP}	maximum power point voltage
I_{sc}	short-circuit current
I_{MPP}	maximum power point current
η	power conversion efficiency
ΔG	Gibbs free energy
ΔA	change in absorption

LIST OF ILLUSTRATIONS

LIST OF TABLES

Chapter 1. INTRODUCTION

1.1 Outlook of Solar Energy

1.1.1 *Current Energy Challenge*

The world's population is projected to reach 9.4 billion by the year 2050, which implies an additional 2.1 billion people will need energy compared to the year 2015.[1] At this growth rate, the global annual energy consumption is estimated to reach around 30 terawatts in the coming 35 years.[1,2] Currently, the world is overwhelmingly dependent on fossil fuels such as oil, natural gas, and coal. Burning such fossil fuels causes significant pollution and climate changes,[1,2] in addition to being non-renewable energy sources that are diminishing gradually. Moreover, such fossil fuels are concentrated in a limited number of countries which makes their transport and availability worldwide more expensive. Therefore, there exists an urgent need to develop economically-sustainable, and environmentally-clean, alternative energy technologies that can easily span wide geographical areas. This need had motivated significant research to identify and optimize useful strategies for the extraction of renewable energy which is derived from natural processes that are replenished constantly. Such renewable energy sources include extracting energy which is stored in water waves, wind, biomass, and solar radiation.[3,4]

Importantly, the sunlight energy which strikes the Earth's surface within one hour exceeds our energy consumption for an entire year.[4,5] In fact, 120,000 terawatts of solar energy reaches the Earth's surface,[6] which vastly exceeds the forecasted energy demands. This abundant resource surpasses all other renewable and fossil-based energy resources

combined; provided it is harvested efficiently.[5] Accordingly, the conversion of solar energy into electricity—*via* the photovoltaic (PV) effect—is receiving incredible attention as a potentially widespread approach to sustainable energy production. The technology is generally based on p-n junctions which are formed by joining n-type (electron-rich) and p-type (electron-poor) semiconductor materials; thus forming an electric field. Upon shining light energy, electrons are knocked loose from the atoms in the semiconductor material and can thus be captured in the form of an electric current.

Currently, crystalline silicon-based modules constitute a huge market share within the global PV industry.[7,8] Whilst these PVs have shown relatively high efficiencies[9] and long durability[10], their high fabrication and installation costs limit wide-scale deployment. In fact, the low absorption coefficient of silicon necessitates the use of thick films (exceeding hundred micrometer) for efficient light absorption.[11,12] The large amount of material required for these devices, along with the sophisticated vacuum processing required for production, arise the need for alternative low-cost and light-weight technologies.[10] Therefore, continued research and development of inexpensive PV technologies is necessary to establish more sustainable energy methods which are cost-competitive to current conventional energy sources.

1.1.2 *Why Solution-Processable Photovoltaics?*

According to the recent state of the PV research posted by the National Renewable Energy Laboratory (NREL),[9] several technologies that are compatible with solution-processing fabrication techniques have emerged promising in light-harvesting devices. Solution-processed materials are those dispersed in a solvent which evaporates during the

photovoltaic manufacturing process.[12] By employing solution-phase material, scalable fabrication techniques like inkjet-printing[13] and spray-coating[14] become possible, which can be combined with roll-to-roll processing for continuous-coating rather than sequential wafer handling.[11,12,15] Such fabrication methods enable large-scale deposition at low temperatures; thus contributing to a substantial reduction in fabrication costs.[6] Moreover, by utilizing active material with higher absorption coefficients than conventional silicon, thinner films could be achieved on light-weight and flexible substrates which minimizes installation costs.[6,11] Among the emerging solution-processable technologies are: organic photovoltaics, dye-sensitized solar cells, solution-processed bulk inorganic photovoltaics, and colloidal quantum dot solar cells.[6] Research on colloidal quantum dot PVs is currently a hot research topic as it revealed significant improvement and promising potential for energy production since the first certified quantum dot-based PV reported in the year 2010.[9,16]

1.2 Colloidal Quantum Dots

1.2.1 *Quantum Confinement*

Colloidal quantum dots (QDs) are small semiconductor nanocrystals (NCs) that are composed of an inorganic core (1-10 nm) and a coating layer of ligands/surfactants which stabilizes them in solution.[17] The first discovery of these NCs in colloidal solution was made by Louis Brus in the early 1980s.[18] Later, Mark A. Reed introduced the term "quantum dot" in 1988 to describe the three-dimensional confinement of these NCs.[19]

In bulk (unconfined) semiconductors, electron-hole pairs (excitons) are typically bound within a characteristic length called the exciton Bohr radius, a_b,[20,21] where

$$a_b = \frac{\hbar^2\,\varepsilon}{e^2}\left(\frac{1}{m_e}+\frac{1}{m_h}\right) \quad (1)$$

$\hbar$ is Dirac's constant, ε is the dielectric constant of the material, e is the elementary charge, m_e and m_h are the electron and hole effective masses, respectively.[21] Within the semiconductor's lattice, the bound electron-hole pairs are usually delocalized over a length much longer than the lattice constant of the material, and they experience a screened Coulombic interaction.[21,22] As the size of the semiconductor decreases below the length-scale of a_b, the charge carrier's wave-functions feel the boundaries of their "container" due to the strong spatial confinement within a potential well. This effect is termed "quantum confinement", and it is a key feature which results in changing the semiconductor's properties as summarized below.

First, the QD would experience increased Columbic interaction energy which significantly alters the allowed energy levels and results in discrete, size-dependent, atomic-like, electronic structures.[15,20] Therefore, unlike a bulk semiconductor which possesses continuous conduction and valence bands (CB and VB) separated by a bandgap (E_g), the QDs exhibit three-dimensional quantum confinement of charge carriers into well-separated energy levels labelled using atomic-like notations such as 1S, 1P, 1D, *etc*. as illustrated in Figure 1.1.[15,20,23] Accordingly, charge carrier relaxation rates and mechanisms are modified from their bulk counterparts.

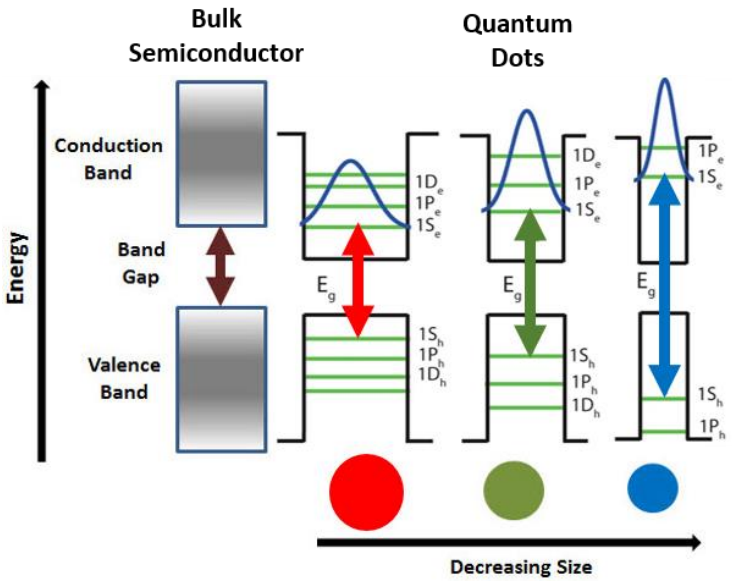

Figure 1.1 Schematic showing discrete atomic-like states and size-dependent bandgaps in semiconductor QDs, compared to a bulk semiconductor. Modified from Semonin *et al.*.[23]

Second, since in this regime the QDs' dimensions define the electronic energy levels, this enables continuous bandgap tunability and renders QDs size-tunable optical and electrical properties. In fact, the QD's size-dependent bandgap, $E_{g(QD)}$, relates to the bulk semiconductor bandgap, $E_{g(bulk)}$, by the following expression:

$$E_{g(QD)} = E_{g(bulk)} + \frac{\hbar^2 \pi^2}{2\ R^2}\left(\frac{1}{m_e} + \frac{1}{m_h}\right) - \frac{1.8e^2}{\varepsilon\ R} \qquad (2)$$

where R is the radius of the nearly-spherical QDs, $\hbar$ is Dirac's constant, ε is the dielectric constant of the material, e is the elementary charge, m_e and m_h are the electron and hole effective masses respectively.[21,24,25] On the right-hand side of equation 2, the second term represents the particle-in-a-box quantum confinement energy for electrons and holes (proportional to R^{-2}), while the third term is the Coulomb interaction between

electrons and holes within a small crystal (proportional to R^{-1}).[21,24,25] Accordingly, as the QD size decreases (*R* declines), the QD's bandgap increases, leading to a blue shift of both the emission wavelength and the spectral onset of optical absorption.[20,22] Thus, by using this effect, one can engineer the QD size to tune the desired optical properties which makes QDs research an attractive field of nanotechnology.

1.2.2 *Synthesis of Quantum Dots*

Since 1993, Murray, Norris, and Bawendi pursued the synthesis of colloidal QDs with narrow size distributions.[26,27] Their research efforts revealed a successful method for the synthesis of monodisperse CdX (X= S, Se, Te) QDs ranging from 2-10 nm in diameter.[26,27] Importantly, the high versatility of the method enabled successive application for the syntheses of other colloidal QDs as well. The synthetic technique was largely inspired by the classic studies by LaMer and Dinegar that show that the production of monodisperse colloids requires the occurrence of temporally discrete events: (1) the nucleation of colloids followed by (2) the controlled growth of existing nuclei, Figure 1.2A.[28]

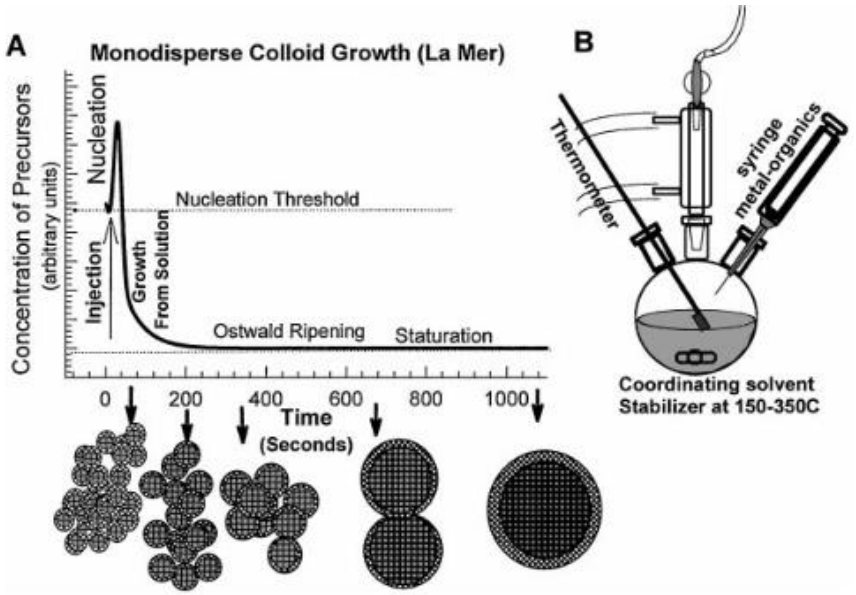

Figure 1.2 A) Schematic depicting the nucleation and growth of colloidal NCs in which various sizes of crystals can be isolated at different time. B) Representation of the synthetic apparatus employed in the preparation of monodisperse QDs.[27]

In fact, a controllable nucleation and growth for the formation of monodisperse QDs was demonstrated by Bawendi *et al.* through the "Hot-Injection" method, Figure 1.2B.[26,27] The synthetic technique involves the rapid injection of a reactive precursor into a hot solution containing the other precursor with long surfactant molecules that inhibit QDs coagulation (*e.g.* alkyl carboxylic acids, alkyl phosphonic acids, alkyl thiols, alkyl amines, or alkyl phosphines).[11,17,27] Accordingly, the thermal decomposition of the reagents takes place and the precursor concentration is raised above the nucleation threshold, Figure 1.2A. Once a supersaturation level is reached, it results in burst nucleation, *i.e.* formation of many QD nuclei in a short burst, to be relieved.[11] As the precursor concentration is lowered below the critical nucleation concentration, no new

nuclei are formed and diffusion-controlled growth proceeds homogeneously across the solution.[11] During this diffusion-limited growth, large particle grow at a slower rate than smaller ones which narrows the size distribution via size-focusing.[29-31] Further reduction of the concentration leads to Ostwald[32] ripening, wherein small particles—that process high surface energy—sacrifice themselves for the growth of larger ones; thus increasing the average particle size with time.[11,15,31] In fact, variations in the reaction time, reaction temperature, and surfactant concentration can be used to synthesize QDs of different sizes and thus different bandgaps.[15] Clearly, this "Hot-Injection" process is successful in providing good control over the size and size-distribution by providing a short nucleation stage followed by a growth stage in which no further nucleation or coagulation of particles occurs. In fact, several mechanistic investigations confirmed that the predicted reaction coordinate in Figure 1.2A is fulfilled for the syntheses of different QDs.[33,34]

1.3 Quantum Dots in Photovoltaics

1.3.1 *Fundamentals of Photovoltaics*

A PV device utilizes a semiconductor material which absorbs the incoming solar photons and converts them into electron-hole pairs, depending on the bandgap (E_g) of the material. In principle, photons whose energy is less than the E_g do not contribute to the photo-generation.[35] On the other hand, photons with an energy greater than the E_g can contribute to the photo-generation process with an energy equivalent to the E_g, while the excess energy is rapidly lost by thermalization.[35] Since a traditional PV can only

harvest a fixed amount of energy from a given solar photon, an optimum bandgap is desired (between 1.1 eV-1.4 eV) for maximum energy utilization.[11,36,37] In fact, the theoretical efficiency limit for a single p-n junction with such an optimal bandgap was predicted by Shockley and Queisser to be around 31%.[36,38]

After the photo-generation, the electrons and holes should be separated and drifted to different electrodes to facilitate the energy conversion process, Figure 1.3A. Accordingly, the PV performance relies greatly on the existence of a smooth interfacial charge transfer (CT) and a long-lived charge separation (CS) state. Specifically, an effective current generation necessitates the occurrence of CT at the donor−acceptor interface on a time scale much shorter than the lifetime of the excited state of the absorber.[39] The rate of the CT may be controlled by tuning the interfacial band alignment and electronic coupling between the donor and acceptor, thus affecting the overall driving force for the charge separation.[40]

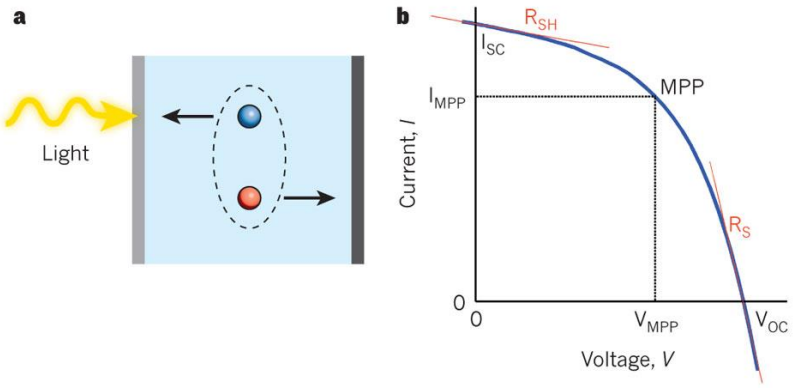

Figure 1.3 A) Schematic describing the light absorption, electron-hole pair generation, and the subsequent charge separation within a photovoltaic device. B) Typical current-voltage curve of a solar cell.[6]

The maximum power which can be retrieved from a solar cell is determined by the maximum power point (*MPP*) on the current-voltage (I-V) curve where the product of the current density and voltage is maximized, Figure 1.3B. The quality of the I-V curve could be defined by the fill-factor (*FF*) which is the ratio of the maximum obtained power to the product of the open-circuit voltage (V_{oc}) and short-circuit current (I_{sc}) as shown in equation 3:[10,11]

$$FF = \frac{I_{MPP}V_{MPP}}{I_{sc}V_{oc}} \quad (3)$$

I_{sc} is the current that flows in a solar cell when its contacts are shorted *i.e.* there is no applied voltage; and it is primarily dependent on the efficiency of light absorption, exciton diffusion, exciton dissociation, and charge collection.[10] On the other hand, V_{oc} is the maximum potential that can be generated when no current flows within the solar cell.[10,11] V_{oc} is mainly determined by the difference in the quasi-Fermi levels of the p-type and n-type junctions, and by the extent of charge recombination.[10,11] The primary figure of merit for PVs is the power conversion efficiency (PCE, η) which is the ratio of the maximum generated electrical power to the optical power incident on the device as described in equation 4:[10,11]

$$\text{PCE } (\eta) = \frac{I_{sc}V_{oc}FF}{P_{in}} \times 100\% \quad (4)$$

1.3.2 *Why Infrared Sensitive Photovoltaics?*

The Sun's radiation which enters the Earth's atmosphere spans the ultraviolet, visible, and infrared regions of the electromagnetic spectrum.[41] Before reaching the Earth's surface, further losses occur at distinct bands due to the absorption from atmospheric gases, moisture, and dust. The additional alterations from absorption and scattering result in a modified solar spectrum which is known as the AM1.5G (air-mass 1.5 global) with an integrated power density of 100 W/m^2.[42] The AM1.5G spectrum was developed by the American Society for Testing and Materials (ASTM) for standard use in characterizing and comparing photovoltaic technologies.[42] Figure 1.4A shows the AM1.5G broadband spectrum spanning from ~280 nm in the ultraviolet to ~4000 nm in the mid-infrared region; with nearly half of the integrated power intensity residing in the infrared beyond 700 nm.[37,43] The figure is juxtaposed with the bandgaps of a variety of inorganic bulk semiconductors revealing that the optimal bandgap for a single-junction solar cell (~1100 nm-850 nm) coincides well with the bandgaps of bulk silicon, InP, and CdTe.[37] In such single-junction PV cells, the photovoltaic response is limited to the portion of the Sun's spectrum whose energy is above the bandgap of the absorbing material, and thus lower-energy photons are not utilized.[35] The inefficient capture of long-wavelength (low-energy) photons restricts the PCE of these solar cells to the Shockley-Queisser limit of 31 %.[36,38]

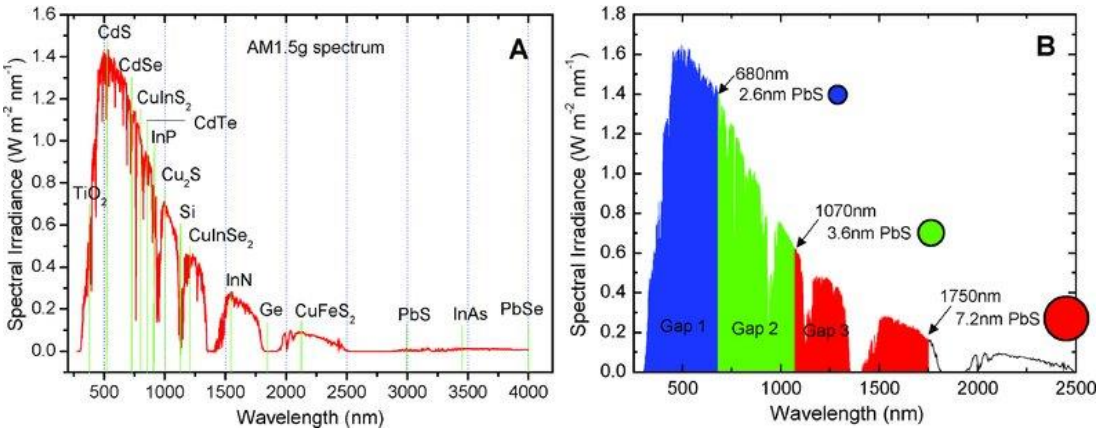

Figure 1.4 A) AM1.5G solar spectrum juxtaposed with bulk bandgap energies of some common bulk semiconductors. B) Bandgap tuning of PbS quantum dots can be employed to build triple-junction solar cells.[37]

A possible approach to avoid this limitation is to stack two or more p-n junctions which are made of materials that absorb different wavelengths of light (*i.e.* have different bandgaps). These are referred to as "tandem" or "multi-junction" solar cells which are designed to have one cell absorb higher-energy photons only to provide a large V_{oc}, and the next cells absorb lower-energy photons to provide additive contributions to the V_{oc}.[43] Accordingly, multi-junction PVs can harvest the Sun's broad solar spectrum more efficiently to provide PCEs that could exceed the Shockley-Queisser limit and reach up to 68%.[6,12,44,45]

The desire for solution-processable material, along with the necessity for the absorption of the Sun's broad spectrum, arise interest in tunable colloidal QDs. Wide-bandgap semiconductors like InP and CdTe have their $E_{g(bulk)}$ in the near-infrared (NIR) spectral range, which limits their quantum confinement tunability towards the visible

spectral region.[37] Accordingly, such material could be employed in one junction within a multi-junction PV, but cannot offer wide spectral spanning along the entire solar spectrum.[37] On the other hand, narrow-bandgap semiconductors like PbS, PbSe, and InAs have their $E_{g(bulk)}$ in the mid-infrared region which lies to the red of even the longest-wavelength junction required in multi-junction PVs.[37] Accordingly, quantum confinement could be utilized on these material to create multi-junction PVs based on a single material strategy.[37] For instance, Figure 1.4B illustrates the ability to tune the bandgap of PbS QDs—by changing their size—to engineer triple-junction solar cells.[37]

1.3.3 *Progress in Lead Sulfide Quantum Dot-Based Photovoltaics*

Here, we focus on PVs based on infrared QDs that offer wide tuning across the solar spectrum. Most intensive recent investigations are based on lead chalcogenide QDs—PbX (X= S, Se, Te)—due to their strong quantum confinement,[46] broad spectral response,[47-50] long exciton lifetimes,[48,51] and versatile synthesis of monodisperse NCs.[49,50] Specifically, lead sulfide (PbS) QD was identified as a promising candidate among other lead-chalcogenides due to its better air-stability,[52,53] and greater earth-abundance.[54] Additionally, its narrow bulk bandgap ($E_{g(bulk)}$ = 0.41 eV)[47] and large Bohr radius (a_b = 20 nm)[46] allow vast QD bandgap tunability between 0.7-2.1 eV which spans the ideal ranges for single- and multi-junction PVs.[55]

The first certified efficiency for a single-junction QD-based PV device employed p-type PbS QD film ($E_{g(QD)}$ = 1.3 eV) and n-type ZnO NCs which approached 3% PCE and revealed promising stability upon 1000-hour constant illumination.[16] Since then,

intensive research was carried out on PbS QD-based PVs and numerous reports showed exciting efficiency enhancements.[56-58] In particular, improvements were based on employing extra surface passivation methods[56,58] and advances in band alignment engineering.[57,58] Importantly, the large surface-to-volume ratio of QDs necessitates effective surface passivation techniques—through ligand control—to reduce charge trapping and recombination losses.[56,58,59] In addition, band offsets between QD layers could be tuned to effectively block electron flow to the anode while facilitating electron extraction.[57,60] Currently, the highest certified PCE for PbS QD-based PVs is 10.6% which was achieved by combining the aforementioned key parameters.[61]

Moreover, the incorporation of lead chalcogenide QDs as light absorbers in PVs revealed promising opportunities for exceeding the theoretical Shockley-Queisser limit, not only through designing multi-junctions by employing their broadly-tunable bandgaps, but also due to their unique ability of utilizing hot electrons[62,63] and generating multiple excitons[64-67] upon the absorption of high-energy photons. In fact, extracting the hot excitons—that have excess energy—before their thermalization is an encouraging approach which enables QD-based PVs in exceeding theoretical efficiency limits.[62,63,68,69] Similarly, multiple exciton generation (MEG) upon the absorption of a single high-energy photon is another approach for recovering some of the wasteful heat energy which exceeds the QD's bandgap.[12,23,36,70] Accordingly, photons having energies greater than the bandgap of the absorbing material do not dissipate their excess energy as heat, but rather produce more electron-hole pairs for higher current

generation.[12,23,36,70] Interestingly, theoretical studies predict that MEG can increase the maximum PCE from ~31% to ~44% for a single-junction solar cell.[71]

In short, PbS QDs hold great potential for low-cost, solution-processed, high-efficiency PVs. Intensive effort on these materials during the past years has raised a number of important basic and applied challenges; some of which will be addressed in this dissertation.

1.4 Objectives and Outline

1.4.1 *Objectives of Dissertation*

This dissertation aims to address two main challenges to aid infrared semiconductor QDs in fulfilling their tremendous potential in PV applications.

First, despite the promising progress of PbS QD-based PVs, there is still a considerable gap between academic studies and industrial applications. This gap is largely attributed to the inability to produce QDs in large quantities while maintaining the uniformity and precise controls of the size and shape. Hence, interest has grown to achieve a scaled-up synthetic procedure of high-quality materials which would be compatible with high throughput fabrication techniques like inkjet-printing and spray-coating methods. Although various batch synthetic procedures had been developed to attain PbS QDs with narrow size distributions,[49,72,73] these standard "Hot-Injection" methods suffer from batch-to-batch variability and scale-up barriers.[74] Since all previous reports of record-performance QD-PVs have been based on small-scale, manual, batch

syntheses,[57,58,75] we aim to design and optimize an automated, continuous-flow, synthetic method for PbS QDs that would allow better reproducibility and higher throughput; which are essential requirements for potential applications.

Second, since an efficient PV device requires fast CT and a long-lived charge separation state, understanding the CT dynamics at QD interfaces is necessary to optimize the PV performance. Yet, CT and CS dynamics investigations at PbS QD interfaces are still limited,[51,76,77] and remain largely unresolved, due in part to the limitations of previous experimental techniques in pumping and detecting with broadband capabilities in the infrared spectral region, where the first exciton absorption peak is located. Here we employ ultrafast, broadband, time-resolved, optical spectroscopy[78,79] which is a powerful technique that provides direct measures of the charge carrier dynamics in photo-excited QDs and enables monitoring the evolution of charge-separated states in donor-acceptor systems having optical features between the visible and infrared regions.[40] We aim to investigate the CT and CS at size-tunable PbS QDs and organic acceptor interfaces using a combination of the femtosecond (fs) broadband transient absorption spectroscopy and steady-state measurements, to evaluate the utility of these material in harvesting the light from the broad infrared solar spectrum. In particular, we address critical questions on how one can engineer efficient CT at interfaces based on PbS QDs by tailoring their size distribution and controlling their surface interactions.

1.4.1 *Outline of Dissertation*

In Chapter 2, we describe the development of a new strategy for flow reactor synthesis of photovoltaic-quality PbS QDs to overcome the current impediment of limited synthetic scale of monodisperse, high-quality materials. The flow-synthetic procedure was optimized to obtain high-quality PbS QDs with $E_g \sim 1.3$ eV, which are of interest for the fabrication of single-junction devices. Furthermore, we test the performance of the flow-synthesized PbS QDs in solar cell devices and compare them to those synthesized by the conventional batch method.

In Chapter 3, we employ different sizes of PbS QDs that absorb in the infrared spectral region (*i.e.* between 800-1500 nm) to investigate the CT and CS dynamics with phenyl-C_{61}-butyric acid methyl ester (PCBM); which is a widely used organic acceptor material in PVs. Through steady-state and ultrafast transient measurements, we investigate the effect of tuning the QD size distribution on the CT and CS mechanisms. In fact, the results reveal that the energy band alignment, tuned by the quantum confinement, is a key element which controls the CT and CS processes. In particular, large PbS QDs ($E_g < 1$ eV) were proven to be ineffective for CT to PCBM, thus limiting the energy harvested from the Sun's broad spectrum.

In Chapter 4, we address the challenge of light-harvesting from large PbS QDs ($E_g <$ 1 eV) in order to facilitate an effective use of different portions of the solar spectrum. Accordingly, we investigate the effect of employing an additional driving force at QD interfaces. Specifically, we study the effect of the presence of interfacial electrostatic

interaction between the negatively-charged PbS QDs and a cationic electron acceptor material. Interestingly, the presence or absence of electrostatic interactions between the negatively-charged large QDs and the positively or neutrally charged acceptors enables tuning the CT from highly efficient and ultrafast (<120 fs) to nearly absent. This approach provides a new pathway for engineering QD-based solar cells that make the best use of the diverse photons making up the Sun's broad infrared spectral range.

Chapter 5 provides a conclusion of this work and gives prospects for future investigations.

Chapter 2. CONTINUOUS-FLOW SYNTHESIS OF QUANTUM DOTS

2.1 Introduction

Colloidal QDs form a flexible material platform for the development of numerous solution-processed optoelectronic devices due to their vast color tunability, high luminescence efficiency, and large surface-area processing.[15] For instance, Samsung had recently launched their QD-based television (JS9500) which provides stunning colors, deep contrast, and incredible brightness, at a cheap cost compared to organic light-emitting diode (OLED) televisions.[80] These devices, and many others, require industrial-scale amounts of high-quality materials with narrow size distributions. Accordingly, scale-up productions of monodispersed colloidal QDs have become an active field of research to facilitate meeting their wide potential application.

The batch synthesis of QDs—within flasks—is traditionally carried out in small volumes, which is suitable for deriving novel synthetic routes and exploring potential applications by developing prove-of-principle device structures. However, these laboratory-scale batch syntheses suffer from significant scale-up limitations. In fact, extending the process to the large-scale is limited by several parameters including: low control over stirring and quenching rates, non-uniformity of temperature, and concentration fluctuations.[81-83]

On the other hand, continuous flow synthesis—within channels/tubings—had emerged as a compelling synthetic technique in the past decade for enabling large-scale

production of chemicals, petrochemicals, and pharmaceuticals without compromising quality or reproducibility.[84,85] Later, the great impact of flow synthesis was extended beyond chemical and medicinal sciences to reach nanotechnology. In 2002, deMello *et al.* proposed the use of narrow channel reactors for NC synthesis and demonstrated that this technique offers distinct advantages over the batch synthetic methods.[86] In particular, conducting the synthesis within narrow channels decreases the velocity dispersion of the reaction mixture, and ensures better thermal and chemical homogeneity throughout the reaction volume.[86] Such well-controlled reaction conditions potentially allow a higher degree of monodispersity.[86,87] Since then, employing flow reactors for the small-scale (≤ 1 g) synthesis of NCs became increasingly popular.[74,82,87-90] For instance, Yang and co-workers utilized a capillary reactor with syringe pumps to synthesize CdSe QDs.[90] By varying the flow rate of the reagents, they controlled the overall residence time in the heated section (i.e. between 2-160 seconds), and hence obtained size-tunability of QDs with photoluminescence quantum efficiencies (PLQE) between 35-55%.[90] More recently, Moghaddam *et al.* designed a scalable continuous-flow approach for obtaining CdSe QDs, in which ~3 g/day could be attained; however, their PLQE was reduced to ~28 %.[91] Accordingly, achieving high-quality nanomaterials on a large-scale remains a challenge.

Some efforts have sought to narrow the particle size distribution *via* segmented flow instead of the traditional laminar flow, Figure 2.1A.[81,92] By segmenting the flow of the reacting phase with an inert immiscible liquid, the reagent dispersion becomes confined

to the volume of the isolated droplets rather than dispersing along the entire length of the channel; thus ensuring better mixing efficiency and a controlled particle size.[89,93] In this case, the immiscible carrier liquid also minimizes the risks of channel clogging/blockage from reagent deposition by preferentially coating the surface of the channel walls.[74,89,94] For example, Chan *et al.* illustrated the utility of a perfluorinated polyether fluid (*i.e.* Fomblin) as a carrier liquid during the synthesis of CdSe QDs within 1-octadecene droplets, and they achieved a stable operation for up to four continuous hours.[92,94] On the other hand, Yen and coworkers compared the quality of CdSe QDs synthesized in a single-phase to those obtained in a segmented flow regime.[81] Single-phase synthesis yielded QDs with significantly broader absorption spectra and broader photoluminescence (PL) full-width-at-half-maximum (FWHM) values, Figure 2.1B,C.[81]

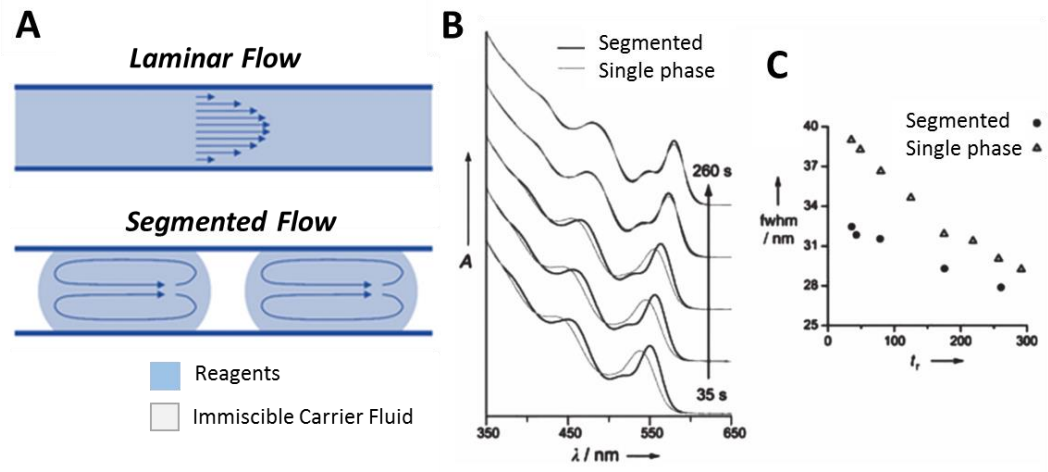

Figure 2.1 A) Schematic illustrating laminar and segmented flow. B) Absorption spectra of CdSe QDs prepared with segmented and laminar flow during different residence times. C) The photoluminescence FWHM of the prepared QDs. Modified from Nightgale *et al.* and Yen *et al.*[81,89]

Essentially, segmented flow synthesis have shown additional control of the size, size distribution, and composition of nanomaterials.[81,87,95] The enhanced control that these reactors can offer, along with their low reagent consumption during optimization, and rapid screening of multiple parameters, make them an attractive alternative to conventional batch reactors.[81,82,93] Moreover, the ease of scaling out the flow reactions by operating identical channels in parallel enables increasing the reaction throughput without any detriment to product quality or yield.[74] This was illustrated recently by employing a five-channel droplet-based reactor, in which the five individual streams enabled increasing the production rate of CdTe QDs to 145 g/day.[96]

Since all previous reports of record-performance QD-PVs have been based on small-scale, manual, batch syntheses,[57,75] we aim to design and optimize a flow-synthetic method for PbS QDs (E_g ~1.3 eV) which are of interest for the fabrication of single-junction devices.[38,53] The synthesis is achieved by reacting the lead precursor (*e.g.* lead oxide) with the sulfur precursor (*e.g.* bis(trimethylsilyl)sulfide, TMS) in a high-boiling point solvent like 1-octadecene (ODE), in the presence of a long-chain stabilizing ligand (*e.g.* Oleic acid, RCOOH where R = $C_{17}H_{33}$).[15,49] After system optimization, we test the performance of the flow-synthesized PbS QDs in solar cell devices and compare them to those synthesized by the conventional batch method.

2.2 Optimizing Continuous-Flow Synthesis

The flow reactor synthesis employed herein was adapted using a commercially available continuous flow reactor, the FlowSyn Multi-X system (Uniqsis Ltd) with

perfluoroalkoxy (PFA) tubing, which is depicted schematically in Figure 2.2. Precursor solutions were prepared in the same manner as in batch[49] synthesis, only deviating by the addition of an inert immiscible fluid (Fluoroinert FC-70)[97] that aids in maintaining clean reaction channels and keeping a consistent reaction volume by segmentation. Further synthesis experimental details are available in Appendix A, section A.3. The reagent bottles were kept under nitrogen overpressure at all times. The precursors were injected through micropumps at different points into the mixing stage whose temperature is set low enough to prevent premature reaction of the precursors. The mixed reactants proceed together to the synthesis stage that is temperature-controlled by a thermocouple in the range of 50 -150 °C. The elevated temperature causes the precursors to react and form nucleation seeds, followed by growth into NCs. The flow rate was changed to control the total residence time. The product was collected in vials containing acetone to quench the reaction followed by a purification procedure similar to the established batch[49,53] synthesis. In short, the precipitate was washed twice with toluene/acetone as solvent/antisolvent mixture, followed by redispering in toluene. Then, the washing procedure was repeated twice again with toluene/methanol mixture, and finally dissolved in octane.

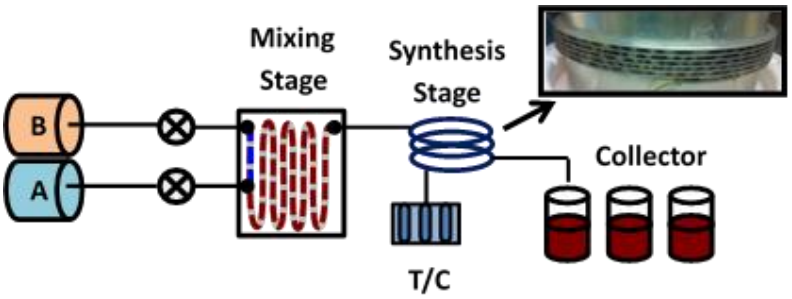

Figure 2.2 Schematic of the single-stage continuous flow reactor synthesis with precursor A (Pb-oleate, ODE, and FC-70), and precursor B (TMS, ODE, and FC-70).[98] Reprinted with permission from reference 98. Copyright 2013 American Chemical Society.

We investigated the absorbance and PL behavior of the QDs produced using this single-temperature stage approach. Importantly, the quality of the QD sample can be evaluated by comparing absorption at both the exciton peak and local minimum, *i.e.* peak-to-valley ratio, which is influenced by the polydispersity in QD size. The PbS QDs synthesized using the single-temperature stage reactor (Figure 2.2) revealed lower quality NCs compared to their conventional batch synthesis counterpart, as seen in the less-defined excitonic feature and notably lower peak-to-valley ratio, Figure 2.3. Additionally, we found that these NCs have a lower PLQE, and a broader FWHM of the PL signal, as summarized in Table 2.1.

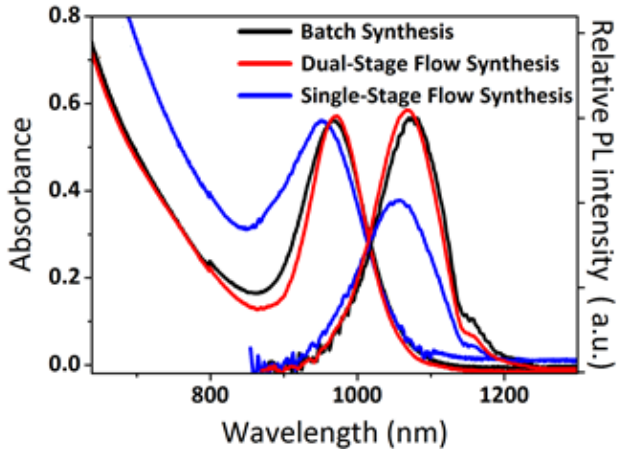

Figure 2.3 Absorbance and PL of PbS QDs synthesized with a single-stage flow approach compared to batch synthesis and dual-stage flow setup.[98] Reprinted with permission from reference 98. Copyright 2013 American Chemical Society.

Table 2.1 Reaction conditions and optical quality assessment of PbS QDs produced by different methods with T_N being the injection temperature to start nucleation in the batch synthesis and in the nucleation stage of a flow reactor, and T_G being the temperature at which growth occurs. Reprinted with permission from reference 98. Copyright 2013 American Chemical Society.

Synthesis Method	T_N / °C	T_G / °C	λ_{Abs} /nm	λ_{PL} /nm	PLQE /%	FWHM /eV
Batch	90	Slow cooling	968	1071	48.8	0.114
Single-Stage Flow	-	75	951	1052	28.2	0.131
Dual-Stage Flow	120	90	970	1065	50.6	0.110

We hypothesized that much greater control over the temperature profile in time/space within the flow reactor would be required to produce high-quality QDs. Distributed temperature zones within a capillary microreactor have been applied in previous work to synthesize narrower size-distribution CdSe QDs.[83] Inspired by this work, we use a dual-temperature-stage coil-reactor (Figure 2.4) to allow the growth phase at a lower temperature than the nucleation temperature; thus leading to a narrower size distribution of the QD population. Table 2.1 summarizes the synthesis conditions and key quality indicators for QDs having E_g ~1.3 eV for three cases: batch, single-stage flow, and dual-stage flow syntheses. QDs made using the dual-stage flow synthesis are superior in their lower Stokes shift, higher PLQE, and narrower PL FWHM compared to single-stage flow synthesis.

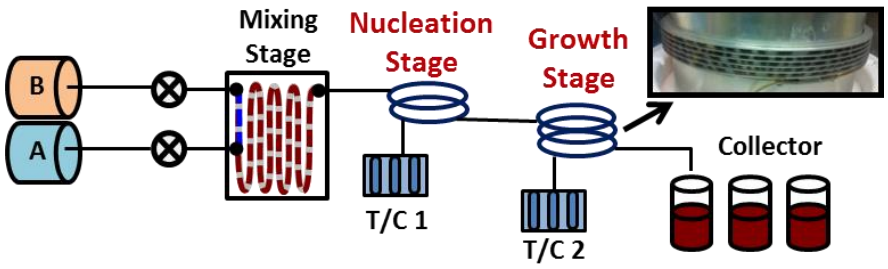

Figure 2.4 Schematic of the dual-stage continuous flow reactor synthesis with precursor A (Pb-oleate, ODE, and FC-70), and precursor B (TMS, ODE, and FC-70).[98] Reprinted with permission from reference 98. Copyright 2013 American Chemical Society.

In a dual-stage reactor, there are at least three main experimental parameters that can be varied independently: the temperature of the nucleation stage (T_N), the temperature of the growth stage (T_G), and the total residence time (t_R). The interplay

between those parameters affects the particle size and distribution in a non-trivial manner. Accordingly, we explored the optimization of the dual-stage approach by separately varying T_N, T_G, and t_R. The main parameters used as indicators of the quality were the half-width-at-half-maximum (HWHM) and the position of the excitonic absorption peak (λ_{Abs}) for each PbS QD sample, Figure 2.5.

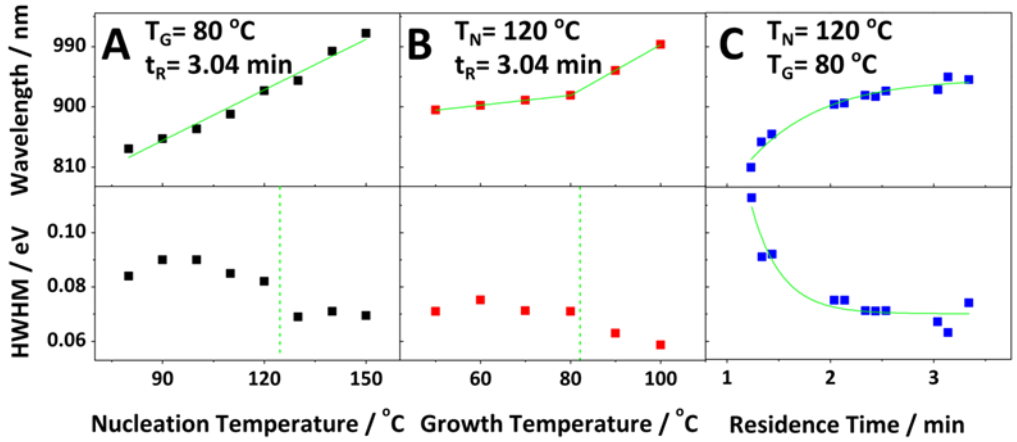

Figure 2.5 Absorbance and HWHM of PbS QDs synthesized with a dual-stage reactor while varying A) nucleation temperature, B) growth temperature, and C) residence time.[98] Reprinted with permission from reference 98. Copyright 2013 American Chemical Society.

By keeping t_R fixed at about 3 minutes we investigated the impact of T_N (Figure 2.5A) on the λ_{Abs} and HWHM at constant T_G= 80 °C. Increasing T_N shifts the QD excitonic peak to higher wavelength, indicating the formation of larger particles. From the HWHM, we find that an optimum T_N is around 120 °C, above which a sudden transition to narrower peak width occurs. We then fixed the nucleation temperature at T_N= 120 °C

in subsequent experiments and varied the growth temperature (Figure 2.5B) and residence time (Figure 2.5C) independently. Accordingly, we optimized T_G and t_R and found that the smallest HWHM for PbS QDs with E_g ~1.3 eV (λ_{Abs} ~950 nm) was achieved using T_G= 80-90 °C and t_R ~3 minutes. These dual-stage flow synthesized QDs revealed compared absorbance peak-to-valley ratio and PLQE to batch-synthesized QDs, Figure 2.3 and Table 2.1.

2.3 Results and Discussion

We then conducted additional spectroscopic and compositional analysis of the optimized dual-stage flow synthesized QDs and compared them to batch-synthesized QDs. In particular, following purification with methanol/toluene mixtures for precipitation/redispersion, the flow reactor QDs remained intact, as seen from the narrow HWHM of excitonic peak and comparable PL amplitude, Figure 2.6.

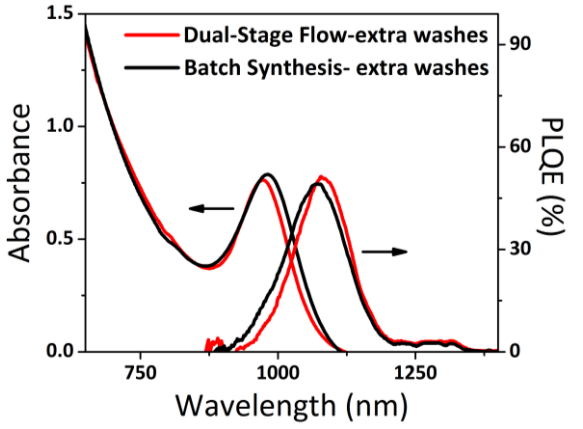

Figure 2.6 Comparison of the absorption spectra and PLQE of QDs after purification.[98]

The elemental compositions of the QDs obtained by the two synthesis methods were compared using X-ray photoelectron spectroscopy (XPS), see appendix A, section A.7 for experimental details. Lead, sulfur, carbon, and oxygen contents of the flow reactor synthesized PbS QDs agreed well with the signature binding energies seen in XPS of batch synthesized QDs, Figure 2.7.

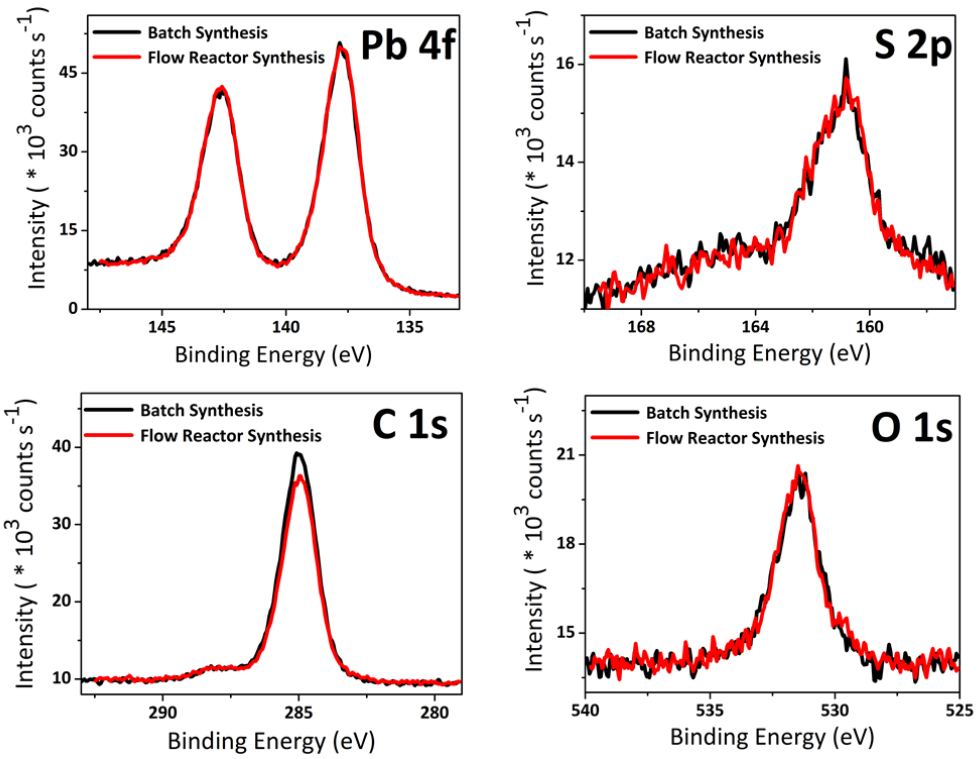

Figure 2.7 XPS data comparing the composition of PbS QDs made by batch synthesis and dual-stage flow synthesis.[98] Reprinted with permission from reference 98. Copyright 2013 American Chemical Society.

Importantly, the scalability of our optimized procedure is manifested by comparing the yield to the traditional batch synthesis. A typical dual-stage flow synthesis of PbS QDs yields approximately 40-42 mg/min which translates to 2.4-2.5 g/hr, compared to

the batch synthesis which yields around 1 g/hr with two reaction setups at the same time.

After validating the quality of the scalable dual-stage flow reactor synthesis, we proceeded to fabricating PV devices with PbS QDs. Originally, the as-synthesized QDs are capped with oleic acid which allows their dispersion in non-polar solvents, *e.g.* octane. This colloidally stable solution of QDs can be easily spin-coated,[47,56] dip-coated,[16,75] or spray-coated[99] onto the desired substrate offering inexpensive film fabrication. Yet, the long oleic acid ligands limit the electronic transport between QDs. Accordingly, a subsequent ligand exchange to shorter ligands is needed to decrease the distance between QDs, and thus decrease the barrier for electron transport.[100]

We employed the spin-coating fabrication technique to deposit PbS QD films in a step-wise addition/spinning process on top of glass substrates topped with fluorine-doped tin oxide (FTO) and TiO_2 NCs film (*i.e.* the n-type electrode). The p-type PbS QD layer was achieved by spin-coating a layer of the oleic acid-capped QDs followed by soaking it with 3-mercaptopropionic acid (MPA) and methanol to achieve solid-state ligand exchange to shorter ligands, as reported in literature.[56,101] The process was repeated until 10 similar layers have been made. Devices were fabricated using PbS QDs synthesized by batch and flow reactor methods for comparison. Further experimental details are available in Appendix A, section A.9.

Figure 2.8 shows the I-V characteristics for the devices based on PbS QDs obtained from batch synthesis, single-stage flow reactor synthesis, and dual-stage flow reactor

synthesis after MPA treatment. Devices made from the dual-stage flow reactor process were superior compared to the single-stage setup and exhibited PCE of 4.1%, V_{oc} of 0.53V, I_{sc} *of* 18mA cm^{-2} and *FF* of 46%; which is comparable with the batch devices. In light of the results reported herein, it is clear that the optimized dual-stage flow reactor approach, with its versatility and rapid screening of multiple parameters, combined with its efficient material utilization, offers an attractive path to scalable and automated synthesis of QDs for PV applications.

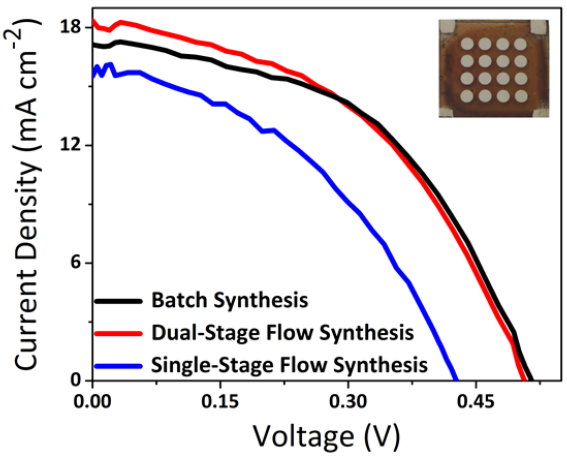

Figure 2.8 Current-voltage characteristics of PV devices based on PbS QDs obtained by batch synthesis, single-stage flow synthesis, and dual-stage flow synthesis.[98] Reprinted with permission from reference 98. Copyright 2013 American Chemical Society.

Chapter 3. EFFECT OF QUANTUM CONFINEMENT ON THE CHARGE TRANSFER

3.1 Introduction

The charge transfer (CT) and separation (CS) across a donor-acceptor interface is a critical step in the solar energy conversion process within any PV device. While the active material must satisfy an efficient light absorption and subsequent charge carrier generation (electrons and holes), without the existence of an efficient CT and CS, the carriers would easily recombine and halt their collection at respective electrodes for current generation.[40] Accordingly, the PV performance relies greatly on the existence of a smooth interfacial CT and a long-lived CS state. In fact, the interfacial CT is driven by the electronic band structure alignment of the donor and acceptor material, Figure 3.1.[40] For instance, a straddling (Type I) band alignment favors the accumulation of both electrons and holes in the narrow bandgap component, which promotes recombination instead of the flow of charges.[40] On the other hand, a staggered (Type II) band alignment enables the separation of electrons and holes into the different components, which is desired for PV applications.[40]

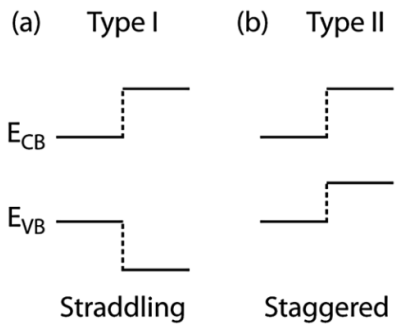

Figure 3.1 Hetero-structure Type I (A) and Type II (B) band alignments.[40]

Importantly, when utilizing bulk materials for solar energy conversion, the materials choice and combinations are limited since the bandgaps and band energy levels that define the interfacial band alignment are material specific.[40] However, quantum-confined QDs provide broader opportunity for controlling bandgaps and band positions through size variations; which enables tuning the interfacial band alignment and, hence, the driving force for CT.[40] In fact, the challenge in realizing an efficient QD-based solar device is utilizing the suitable materials that provide an appropriate energy level alignment which promotes electron injection from QDs to the material (or vice versa), while suppressing back electron transfer to the donor (which leads to the undesirable electron-hole recombination).[102] Hence, understanding the interfacial CT and recombination processes as a function of QD size can clearly support the improvement of the solar device performance, by providing crucial understanding of the photophysical and photochemical processes in donor-acceptor systems.

Ultrafast transient absorption (TA) spectroscopy is a powerful technique that provides direct measures of the charge carrier dynamics in photo-excited QDs and enables monitoring the evolution of charge-separated states in donor-acceptor systems.[40] The method is based upon a pump-probe system in which an ultrashort laser pulse—whose time duration is in the picosecond (ps) or femtosecond (fs) time scale—is directed to excite the sample and create excited charge carriers, followed by a probe pulse (after a controlled delay time) to monitor the CT, CS, and recombination dynamics in the time domain. Additionally, the CS may be elucidated by tracking specific

spectroscopic signature signals representing the electron donor in its oxidized state, or the electron acceptor in its reduced state. In fact, the widely-informative TA spectra are obtained by subtracting the ground state absorption spectrum (before excitation) from the excited state absorption spectrum, at different delay times, to obtain the change in absorption as a function of wavelength and time, $\Delta A(\lambda, t)$.[103] A schematic of the TA setup and an illustrative TA spectra are depicted in Figure 3.2. These TA spectra reveal invaluable information on several dynamical processes upon the occupation of the excited state (*e.g.* charge separation, trapping, radiative recombination, Auger recombination, *etc*.).[103] Such information can be extracted from positive and/or negative signal contributions within the ΔA spectra, which result from different processes including:[103]

a) Ground State Bleach (GSB): corresponds to the depletion of the ground state population upon interaction with a pump pulse. Consequently, a negative signal is observed at the wavelength region of the ground state absorption, due to an increase in the intensity of detected light.
b) Excited State Absorption (ESA): represents the promotion of charge carriers that were previously excited by a pump pulse, to an energetically higher excited state upon interaction with the probe pulse. Accordingly, a positive signal is obtained at the wavelength region of excited state absorption, due to a decrease in the intensity of detected light (*i.e.* photons become absorbed by a sample in a spectral region where they were previously transmitted).

c) Photoproduct Absorption: results from the interaction of newly formed chemical species or long lived excited states (*e.g.* charge-separated states, triplet states) with the probe pulse which promotes them to excited states. Since photons become absorbed by the sample in a spectral region where they were previously transmitted, the intensity of detected light decreases which reveals a positive signal.

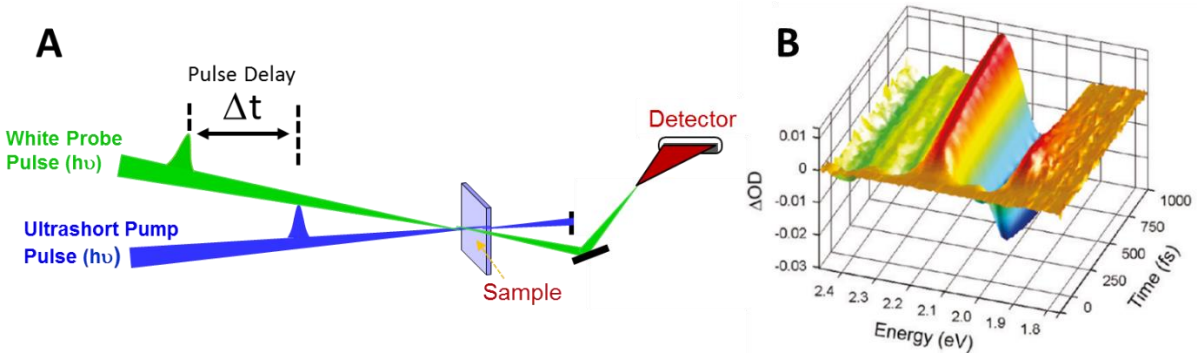

Figure 3.2 A) Schematic of the pump-probe transient absorption spectroscopy setup. B) Illustrative transient absorption spectrum showing commonly observed signals.[104] Reprinted with permission from reference 104. Copyright 2011 American Chemical Society.

Using TA spectroscopy, the CT between various metal chalcogenide QDs (*e.g.* CdSe, CdS, PbS, PbSe) and TiO_2 (different morphologies) had been extensively investigated and gave promise to utilizing QDs in PVs.[62,76,105-110] In particular, Kamat *et al.* have reported electron injection to TiO_2 nanoparticles within the ps and ns timescales from CdS[107] and PbS[110] QDs, respectively. While Lian *et al.* observed an ultrafast electron transfer of ~6 fs from PbS QDs to TiO_2 nanocrystalline thin film,[76] which is competitive with the rate of hot electron relaxation (0.2–6 ps)[111] and exciton-exciton annihilation (10-100 ps)[66], and

was thus argued to be suitable for extracting hot carriers and multiple excitons.[76] Similarly, electron injection from PbSe QDs to TiO_2 single crystal surfaces was estimated to be ~50 fs.[62] The effectiveness of such an ultrafast CT was supported by a model cell which revealed a photo-current enhancement (~170% absorbed photon-to-current conversion efficiency) upon exciting at 3-times the bandgap (i.e. near UV region) and was attributed to the collection of multiple excitons.[64] Additionally, other reports have shown that implementing bandgap tuning *via* QD size variations enables controlling the driving force of CT from QDs to TiO_2, and to other metal oxide acceptors like ZnO and SnO_2.[107,109,110] For example, the CT from excited CdSe QDs into the CB of TiO_2 nanoparticles showed size-dependence and an increase by three orders of magnitude upon decreasing the QD size from 7.5 to 2.4 nm.[109]

Another emerging approach for the fabrication of QD-based PVs is the employment of organic semiconductor materials as electron acceptors and transporters, which is an attractive method since they share some advantages with colloidal QDs including low-cost fabrication, solution-processing, and well-controlled synthesis methods.[112] Yet, low PCE efficiencies have been recorded for such inorganic-organic hybrids, presumably due to low electron injection rates as compared to other competing processes, like carrier recombination.[15,102,112] This has encouraged researchers to elucidate the efficiency of CT between PbS QDs and some organic acceptor material including benzoquinone,[51,113] tetracyanoquinodimethane,[114] and methylene blue,[115] to better understand the promises and limitations of such inorganic-organic hybrids. While others have exerted

sustainable efforts in improving the PCE of devices constituting PbS QDs with fullerene-,[102,116,117] carbon nanotube-,[118] and graphene-[119] based acceptor material. However, although the relative energy levels of the constituents play a crucial role in determining the efficiency of the CT to organic acceptors, only limited studies have discussed the effect of QD size variations with the most promising QDs for PV, namely, PbS QDs.[120] Hence, critical questions remain on how one can engineer efficient CT at interfaces based on PbS QDs by tailoring their size distribution to harvest most of the incident solar spectrum.[40,121] The ability to engineer fast and efficient CT in PbS QDs, or other QDs in general, may result in additional control of PV operation as well as efficiency enhancements.

In this work, we study the CT and CS kinetics at PbS QD/organic acceptor interface upon size-tuning the QDs to absorb different portions of the infrared spectral region. Quantitative data on CT dynamics can be directly resolved, with high precision, by applying broadband pump−probe spectroscopy to excite and detect the wavelengths around the first exciton absorption peak, typically located in the near-infrared region in PbS QDs. Using this approach,[78,79,122,123] we can directly investigate the interfacial charge transfer, separation, and recombination in the time domain. We combine broadband fs-TA spectroscopy and PL quenching measurements to investigate the effect of QD size variations on the dynamics of CT from PbS QDs to phenyl-C_{61}-butyric acid methyl ester (PCBM). PCBM was chosen as the electron acceptor for this study due to its wide use in PVs and its suitable electron affinity of 3.9 eV.[124]

3.2 Synthesis and Characterization

Size-tunable, oleic-acid capped PbS QDs were synthesized by the batch method using lead oleate and TMS as precursors in ODE, as described by Hines and Scholes.[49] Typically, the injection temperature and precursor concentration were varied to tune the QD size; further experimental details are available in Appendix A, section A.2. In the following QD size-dependent study, we refer to the QD samples based on the wavelength of the first exciton absorption peak; *i.e.* the sample with the $1S_h \rightarrow 1S_e$ peak at 880 nm is named PbS-880. This work involved four different QD sizes whose λ_{Abs} ranged between 800-1500 nm; namely, PbS-880, PbS-1080, PbS-1320, and PbS-1470.

The synthesized QDs were characterized by transmission electron microscopy (TEM) to obtain structural and size information; see appendix A, section A.8 for experimental details. These QDs were nearly spherical in shape as indicated by the high resolution TEM images in the top panel of Figure 3.3. The average sizes of the different PbS QD samples were calculated by measuring the diameter of ~300 particles. For instance, the average size for small (PbS-880) and large (PbS-1320) QDs were found to be 2.84 ± 0.27 nm and 4.70 ± 0.36 nm, respectively. These results are in very good agreement with the model proposed by Moreels *et al.*[125] that relates the bandgap and diameter of PbS QDs by the following equation:

$$E_g = 0.41 + \frac{1}{(0.0252d^2 + 0.283d)}$$

where E_g and d are the bandgap and the diameter of PbS QDs, respectively, which suggests a predicted average size of 2.83 nm and 4.81 nm, for PbS-880 and PbS-1320, respectively.

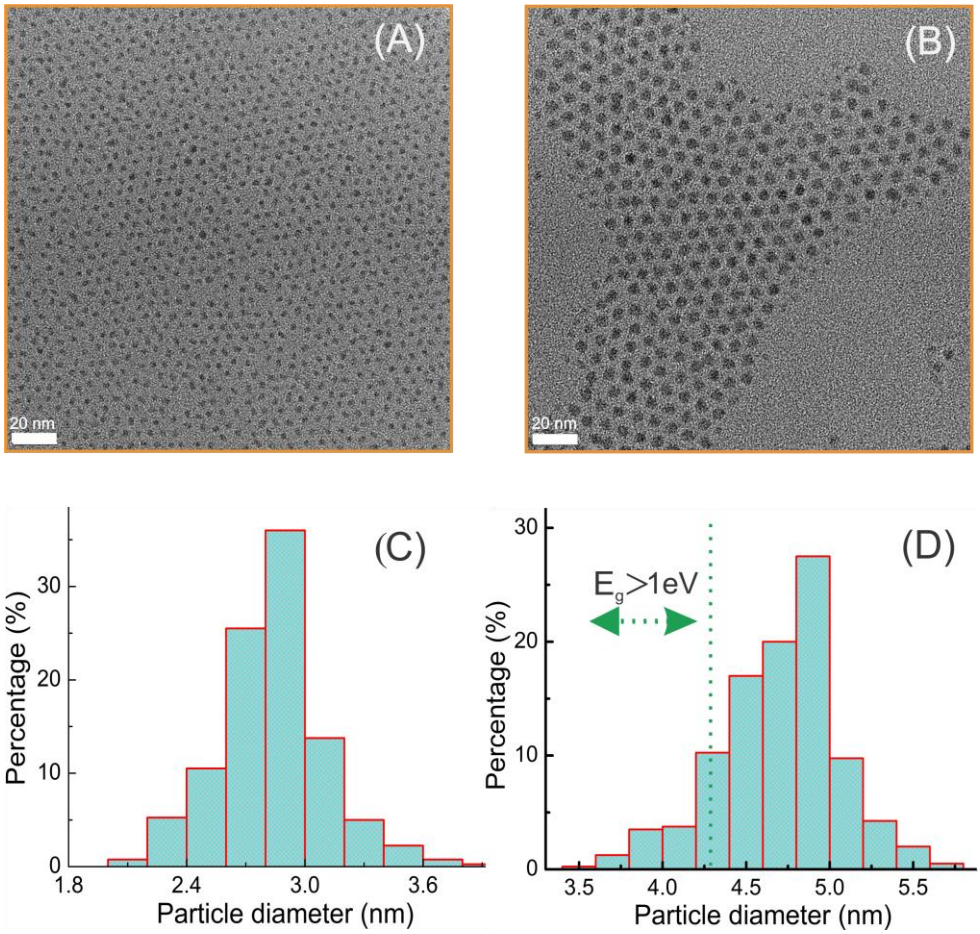

Figure 3.3 The top panel represents TEM images of PbS-880 (A) and PbS-1320 (B) with 20 nm scale bars. The size distributions of PbS-880 (C) and PbS-1320 (D) were determined by measuring the diameter of 300 particles.[126]

Figures 3.4A and B show the steady-state absorption and PL spectra of PbS-880 and PbS-1320, respectively. The well-defined absorption peaks (left panel) correspond to the

$1S_h \rightarrow 1S_e$ transition, while the PL peaks (right panel) have a Gaussian shape with comparable FWHM indicating that the emission is due to a well-defined single quantum state. PbS-880 and PbS-1320 reveal PL emissions at 992 nm and 1347 nm, respectively. Accordingly, the Stokes shift shows strong dependence on the QD size; while 112 nm (0.159 eV) shift is observed for the small QDs, only 27 nm (0.019 eV) shift is recorded for the large QDs. One proposed interpretation for the dependence of Stokes shift on the QD size is based on the presence of a long-living luminescent, size-dependent, in-gap state.[127] In this case, radiative transitions can take place to the ground state either from higher (S_1) or lower (S_2) energy levels; the luminescence of small-size QD arises mainly from S_2, whereas the luminescence from S_1 is predominant in large QDs.[127]

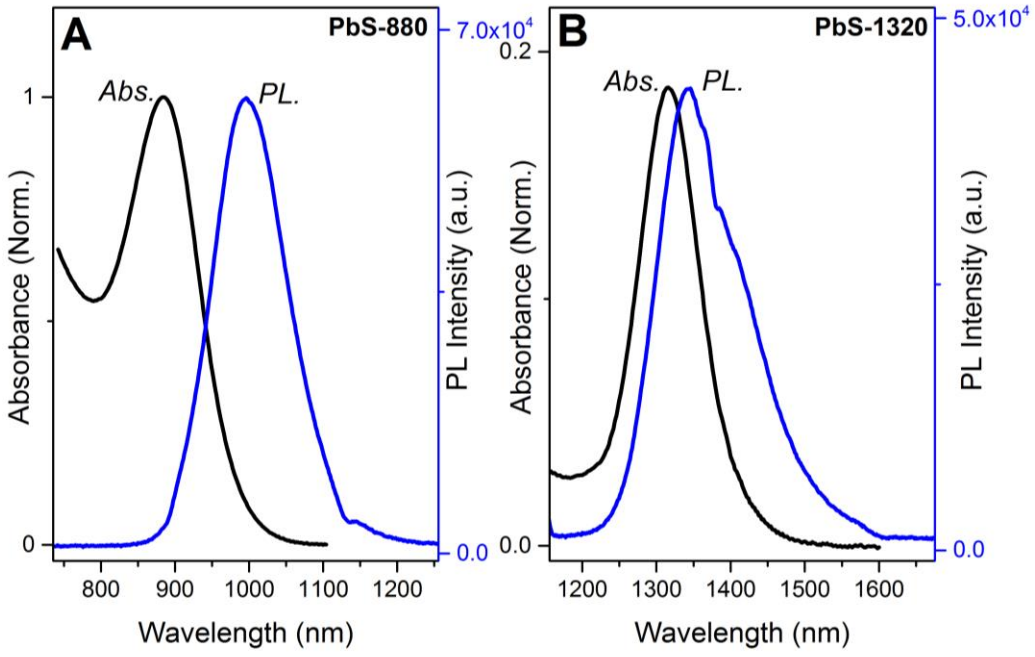

Figure 3.4 Absorbance and PL of PbS-880 (A) and PbS-1320 (B) QDs in 1,2-dichlorobenzene, showing the size-dependent Stokes shift.

3.3 Interfacial Charge Transfer Measurements

For the steady-state quenching measurements, the stock oleic acid-capped PbS QDs dispersions were diluted with 1,2-dichlorobenzene to maintain a constant concentration ($\sim 1.5 \times 10^{-6}$ M), as determined by the optical density at the first exciton absorption peak (*i.e.* $1S_h \rightarrow 1S_e$ transition) within a 1 cm path length quartz cuvette. Alternatively, the stock solutions were diluted with different concentrations of PCBM in 1,2-dichlorobenzene while maintaining a fixed QDs concentration. Further experimental details are available in Appendix A, section A.10.

For the transient absorption measurements, the stock PbS QDs were diluted with extra 1,2-dichlorobenzene, or alternatively PCBM in 1,2-dichlorobenzene, while maintaining a fixed QD concentration ($\sim 1.5 \times 10^{-6}$ M) as determined by the optical density at the first exciton absorption peak within a 2 mm path length cuvette. All TA experiments were conducted at room temperature, with constant sample stirring to avoid the photocharging of the QDs.[128,129] Femtosecond broadband pump−probe spectroscopy was employed to excite and detect the wavelengths around the first exciton absorption peak of PbS QDs; a schematic of the experimental setup is depicted in Figure 3.5.[79] Briefly, the system constitutes a fundamental laser which is provided by a Ti:Sapphire femtosecond regenerative amplifier that produces 35 fs pulses at 800 nm with 4 mJ of energy/pulse, and a repetition rate of 1 kHz. The pump (excitation) beam is tuned by passing 1 mJ of the fundamental (λ=800 nm) through an optical parametric amplifier (TOPAS-C) which can tune the wavelength between 240-2600 nm to excite

certain transitions within the sample. As for the probe beam, a portion of the fundamental is routed *via* a computer-controlled delay line, adjustable pinholes, focusing lens, and variable neutral density filter to a crystal for white light continuum (WLC) generation; and further to the sample *via* a focusing mirror. Following the interaction with the sample, the probe beam is directed towards a spectrometer which can detect in the visible range or near-infrared region.

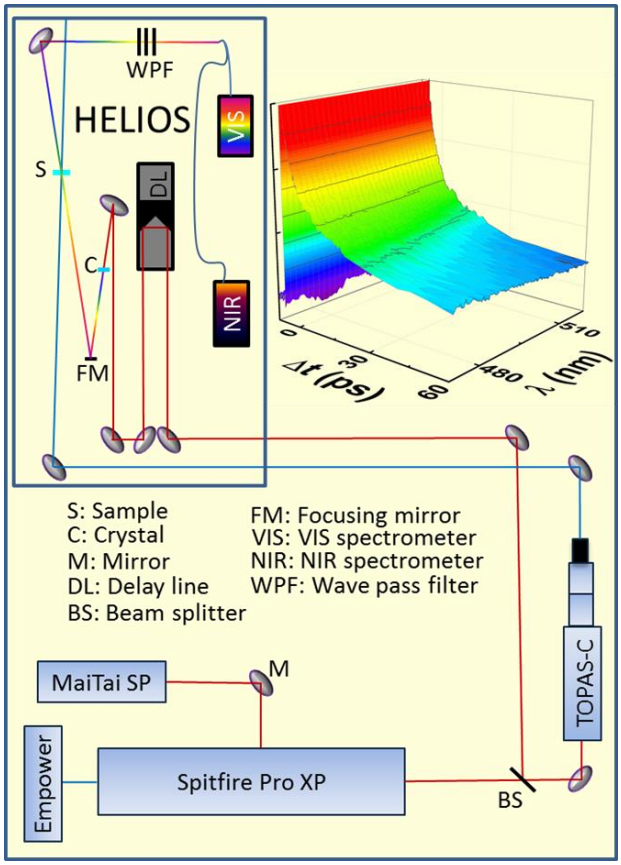

Figure 3.5 Setup schematic for the femtosecond broadband transient absorption spectroscopy employed during measurements. The figure shows the integration of the visible and near-infrared spectrometers with the fs-regenerative amplifier (Spitfire Pro) and optical parametric amplifier (TOPAS-C).[79,126]

For our measurements, the TA spectra were averaged until the desired signal-to-noise ratio was achieved. The absorption spectrum of each sample measured before and after TA experiments did not show any degradation. Further experimental and insrtumental details are available in Appendix A, section A.11.

3.4 Results and Discussion

Figure 3.6 shows the changes in the steady-state absorption and PL spectra of PbS-880 and PbS-1320, upon the addition of different concentrations of PCBM, ([PCBM] = 0-50 mM). The observed PL quenching of PbS QDs upon addition of PCBM indicates the presence of a photo-induced electron transfer between the PbS donor and the PCBM acceptor species.[130,131] While exciton quenching could also occur by energy transfer, here we rule out this mechanism due to the lack of spectral overlap between the absorption of PCBM and the emission of PbS QDs (Appendix B, section B.1). It was previously shown that electron transfer rate from QDs to adsorbed electron acceptors increases with the number of acceptors;[132] hence, a stronger PL quenching is expected as the PCBM concentration increases. For PbS-880, the addition of 25 mM PCBM was sufficient to reduce PL emission to nearly null, Figure 3.6A, thus suggesting that the electron extraction by PCBM competes directly with electron–hole recombination processes. Also, the 25 mM PCBM addition resulted in slight blue shift of the PL peak (~15 nm, 0.019 eV) and first exciton absorption peak (~4 nm, 0.0065 eV); which may originate from the redistribution of electron density, and is characteristic for the ground-state complex formation.[133]

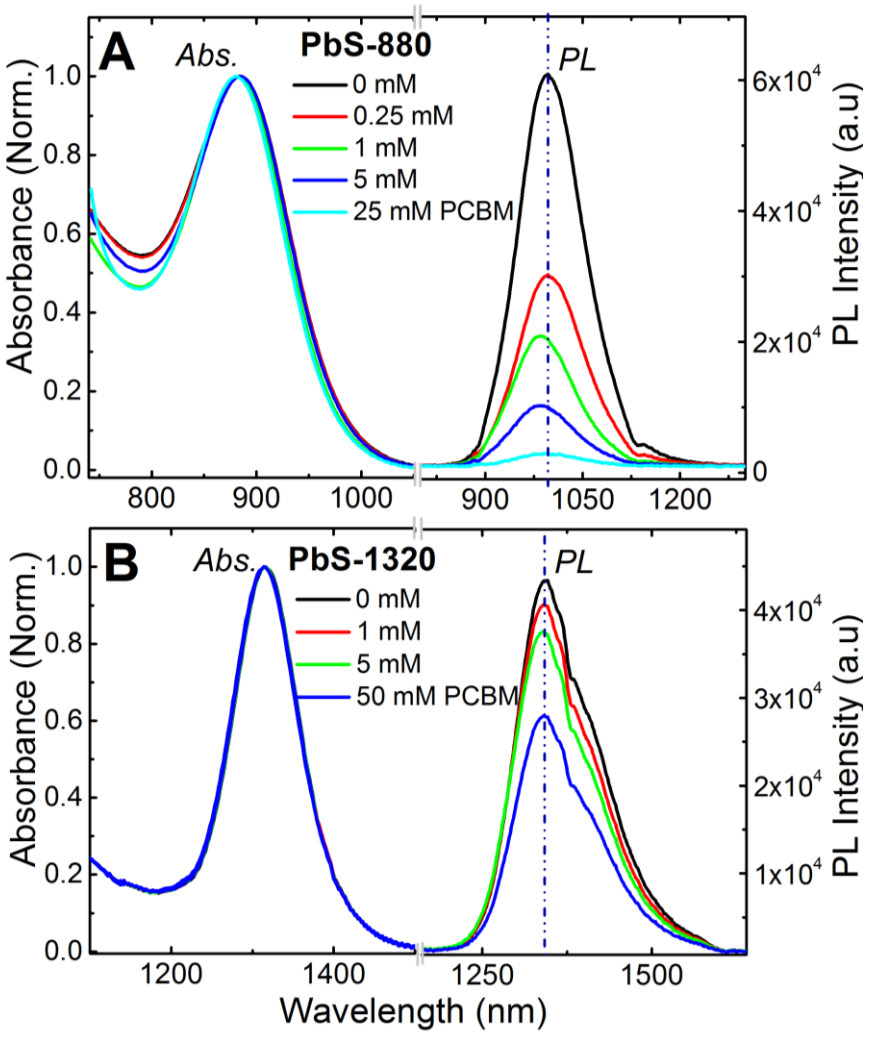

Figure 3.6 Absorbance and PL spectra of PbS-880 (A) and PbS-1320 (B) upon the addition of different concentrations of PCBM, in 1,2-dichlorobenzene. The PL spectra were recorded upon excitation with λ_{ex} = 890 nm and λ_{ex} = 1150 nm, respectively.[126]

On the other hand, the PL quenching behavior is substantially reduced for PbS-1320, even at increased PCBM concentrations, Figure 3.6B. The significant differences in the PL quenching behavior in PbS-880 versus PbS-1320 can be attributed to the band alignment between PbS QDs of different diameters and the PCBM acceptor. Effective CT

at the PbS / PCBM interface requires a Type-II interface band alignment, as commonly found in other donor-acceptor systems.[134] Figure 3.7 shows the band alignment at the PbS / PCBM interface for PbS-880 and PbS-1320 QD samples. To derive the band alignment, we employed an ionization potential of 4.9 eV for PbS,[135] and an electron affinity of 3.9 eV for PCBM.[124] Within this model, a PbS bandgap larger than ~1.0 eV is necessary to achieve Type-II alignment, whereby the CB level of PbS is higher in energy than the LUMO level of PCBM, thus enabling effective electron injection from the excited state of PbS to PCBM. We observe that the bandgaps of PbS-880 and PbS-1320 QDs with ideally monodispersed diameters are $E_g \approx 1.4$ eV and $E_g \approx 0.95$ eV, respectively, thus indicating that only the smaller PbS-880 QDs can effectively inject electrons into PCBM. The PL quenching measurements for our PbS-880 and PbS-1320 solutions mixed with PCBM are consistent with this model, with slight deviations induced by the non-ideally monodispersed size in our samples. In particular, since the critical gap of 1.0 eV corresponds to a 4.3 nm diameter, only QDs with $d < 4.3$ nm can contribute to the CT. The size distribution plots in Figure 3.3 show that all the QDs in the PbS-880 sample satisfy $d < 4.3$ nm and can thus contribute to CT to PCBM, while in the PbS-1320 sample $d < 4.3$ nm holds only for a small-diameter tail of ~13±1% of the QDs, Figure 3.3D.

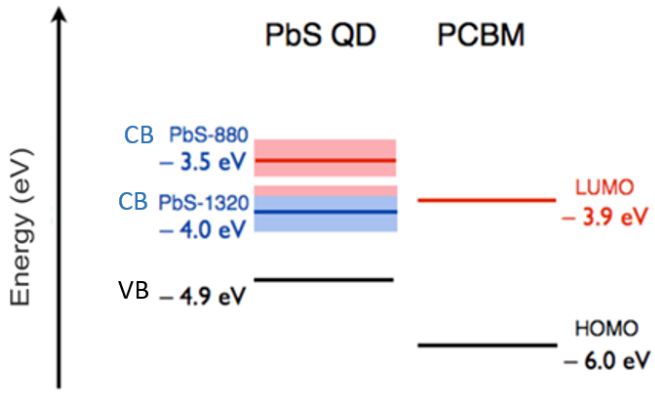

Figure 3.7 Interface band alignment between the two donors PbS-880 and PbS-1320, and the PCBM acceptor. The VB and CB energies for PbS QDs are provided as a range to reflect the size distribution. The states contributing to CT from PbS-880 and the large-bandgap tail of PbS-1320 are shown in red in the PbS donor side, while the states not contributing to CT are shown in blue.[126]

On this basis, we attribute the fast PL quenching observed in the PbS-880 to the presence of CT upon interaction of PbS with PCBM in solution, resulting in the quenching of the PL from the $1S_e \rightarrow 1S_h$ state of PbS. On the other hand, the near-absence of PL quenching in the PbS-1320 QDs is consistent with the absence of Type-II alignment. We propose that the ~13% fraction of QDs with energy gap above ~1 eV are responsible for the residual CT and PL quenching in the PbS-1320 sample, leading to an overall slow rate for PL quenching as observed in our measurements. A quantitative analysis of the PL curves in Figure 3.6 supports this interpretation, as observed in Table 3.1 which shows the relative PL quenching upon the addition of [PCBM]= 0 mM, 1 mM, and 5 mM, to PbS-880 and PbS-1320 solutions; where the 0 mM sample corresponds to

pristine PbS QDs. We remark that while several authors have shown the tunability of the bandgap and photoabsorption in PbS QDs by controlling their size, our measurements highlight the important fact that by tuning the diameter and bandgap of PbS, the interface band alignment can be changed from Type-I (ineffective for CT) to Type-II (effective for CT), similar to what has been found for interfaces of single-walled carbon nanotubes and PCBM.[136]

Table 3.1 Relative PL quenching upon the addition of different concentrations of PCBM to PbS-880 and PbS-1320 solutions.

[PCBM]	*PL Intensity (arbitrary units)*	*Relative PL Quenching*
	PbS-880	
0	60910	--
1	20841	66 %
5	10213	83 %
	PbS-1320	
0	30660	--
1	27943	9 %
5	27242	12 %

A further consideration for donor-accepter systems in the solution phase is whether fluorescence quenching is taking place *via* 1) static quenching whereby a non-luminescent ground-state complex is formed between the ground-state fluorophore and

the quencher, 2) dynamic quenching which involves the collision and subsequent formation of a transient complex between the excited-state fluorophore and the ground-state quencher, or 3) a combination of both mechanisms.[137,138] We have conducted our quenching experiment to cover a large range of PCBM concentrations (0.01-25mM) where a considerable PL quenching was observed with PbS-880. Then, we constructed a Stern-Volmer (SV) plot[137] for the relative emission intensity as function of the quencher concentration, which revealed a downward curvature (Appendix B, section B.2). This curvature is understood in term of a saturation effect at the high concentrations of PCBM onto the PbS QD surface.[139,140] Importantly, the spectral shift in the absorption and emission spectra, along with the ultrafast electron injection to PCBM as inferred from the formation of the anionic species PCBM$\bullet^-$ (explained below), and the charge recombination as inferred from the ultrafast GSB recovery (explained below), provide clear indication for the ground state complexation and subsequently static electron transfer. This is in prefect agreement with the electron transfer observed between QDs (including PbS and CdS) and other molecular acceptors.[51,141]

Next, we employed fs-TA spectroscopy to study the GSB due to the $1S_h \rightarrow 1S_e$ transition in PbS QDs. Since this signal is directly associated with the electron population in the conduction band, we used it as a convenient probe to follow the carrier transfer and recombination dynamics. In particular, we used the GSB recovery to follow the charge recombination dynamics. The TA measurements of different QD sizes (PbS-1470, PbS-1320, PbS-1080, and PbS-880) were recorded following laser pulse excitation at

~1.1 times the bandgap, i.e. 1340 nm, 1200 nm, 960 nm, and 780 nm, respectively. It is worth pointing out that the optical excitation at $1.1E_g$ eV was chosen to avoid any contribution from the scattered light in the GSB signal, assuring high quality data and accurate dynamics for the electron transfer process.

Figure 3.8 compares the TA spectra of the small (PbS-880) and large (PbS-1320) QDs in the absence and presence of different PCBM concentrations. Upon bandgap excitation of these QDs, the GSB signal is evident as a bleaching maxima coinciding with the same wavelength of the first exciton absorption peak. In the absence of PCBM, the GSB reveals a very small decay in the picosecond time scale. This decay may be attributed to state trapping due to an incompletely passivated QD surface, and its amplitude was a few percent lower than the reported value for similarly sized PbS QDs.[115] This state trapping will provide additional recombination pathways.[142] As can be seen in Figure 3.8, the bleaching of the first excitonic peak (*i.e.* 1320 nm for large QDs and 880 nm for small QDs) was monitored upon increasing [PCBM]. It is evident that higher [PCBM] accelerates the GSB recovery (due to charge recombination) of PbS-880 much more than PbS-1320; providing clear indication for the formation of strongly coupled radical ions from effective CT between PCBM and smaller PbS. Such an enhanced GSB recovery further confirm the presence of an alternate deactivation pathway for the charge carriers in smaller PbS, which implies effective electron injection from the CB of PbS to the LUMO of PCBM.[120] Moreover, the GSB feature of PbS-880 revealed a blue shift of a few nanometers upon the addition of PCBM, depending on the

PCBM concentration, in perfect agreement with the shifts observed in the steady-state absorption measurements. Electron injection from PbS-880 to PCBM was additionally monitored by the appearance of an absorption feature at a wavelength of ~1040 nm characteristic for a fullerene radical anion (PCBM•⁻),[143,144] providing conclusive experimental evidence for the CT event. As can be seen in Figure 3.8 inset, the electron injection to PCBM occurs within our temporal resolution of 120 fs; thus confirming efficient electronic coupling between the CB of the PbS QDs and the LUMO of PCBM. Crucially, the PCBM•⁻ feature remained more pronounced for smaller QDs throughout our window frame, and the GSB recovery reached a plateau (no further recovery), providing evidence of the CS in which the radical ion pairs can be dissociated into free ions. This is supported by the energetic considerations which is a convincing argument in favor of the charge separation. Additionally, leveraging on the fact that the photocurrent generation requires CS, our observation of CS is supported by previous photocurrent measurements of PbS-PCBM blends where the photocurrent response was at least two orders of magnitude higher for the smaller PbS QDs compared with larger size.[120] Interestingly, the photocurrent in blends of PbS-1320 did not peak after excitation at the first exciton transition, but at shorter wavelength, a small photocurrent signal was measured and attributed to the smaller size distributions.[120] These observations are fully consistent with our finding in terms of efficient CT and CS tuned by the quantum size effect.

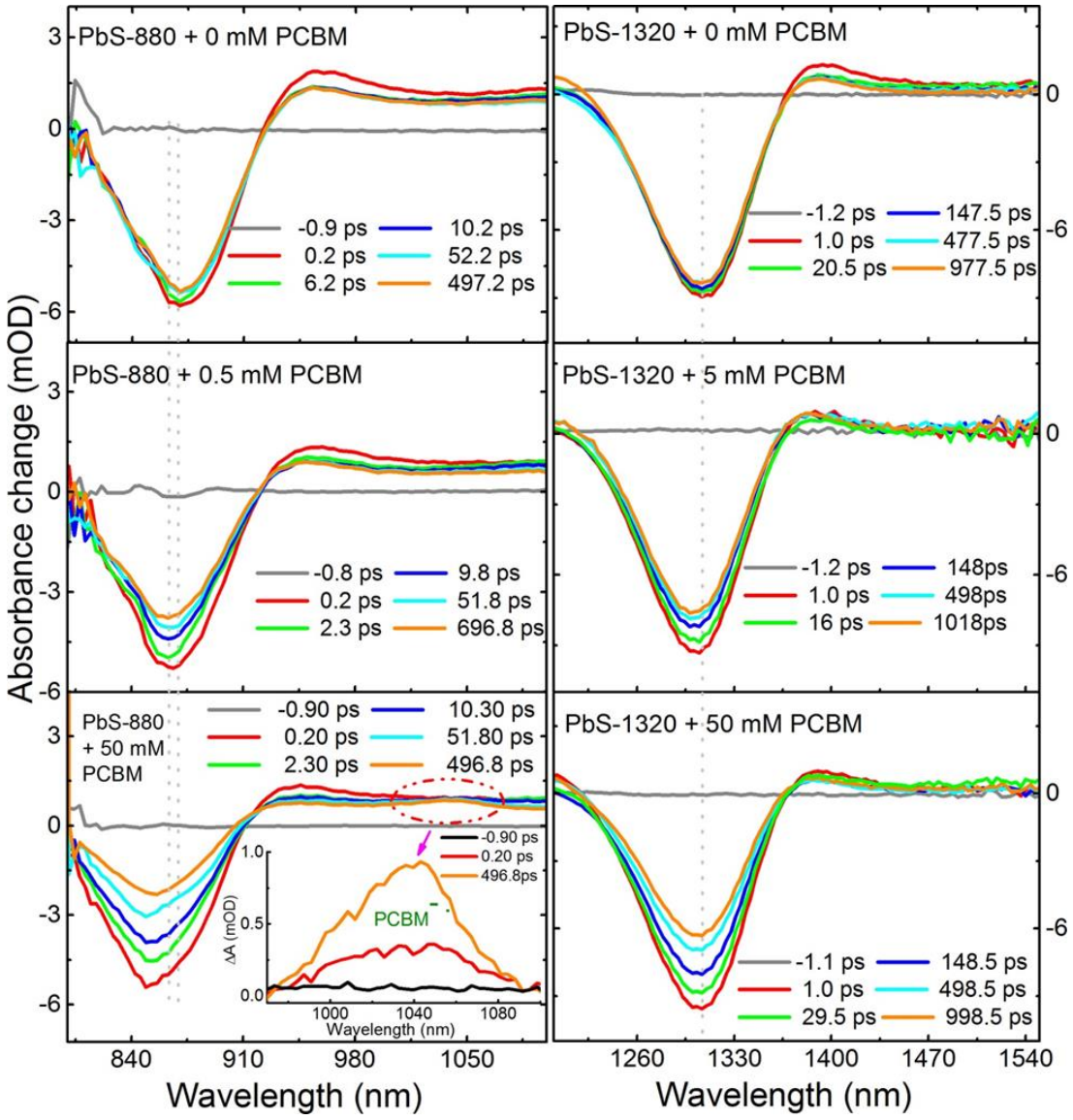

Figure 3.8 Averaged TA spectra at indicated delay time windows following laser pulse excitation at 1.1E_g of PbS QDs, upon increasing concentrations of PCBM.[126]

The fitted GSB recovery kinetics indicate that not only the percentage recovery is highest for the smaller PbS QD size, but also the rate of carrier recombination is affected by both the size of QDs and the PCBM concentration, Figure 3.9. For instance, the recovery time constants for PbS-880 (Figure 3.9A) were fit to double-exponential

functions with time constants of a few ps, and tens-to-hundreds of ps, that shorten at increased PCBM concentration. The observed two components point to the occurrence of two types of donor-acceptor ions pairs with different associated couplings/distances which can be differentiated by their different recombination dynamics.[145,146] The existence of different types of ion pairs upon CT had been reported for other donor-acceptor systems.[145,146] On the other hand, the GSB kinetics for PbS-1320 (Figure 3.9B) revealed significantly slower recombination dynamics which were fit to a single-exponential function, along with lower overall percentage recovery (~30 %) upon PCBM addition; which is induced mainly by ~13% outliers in the size distribution.

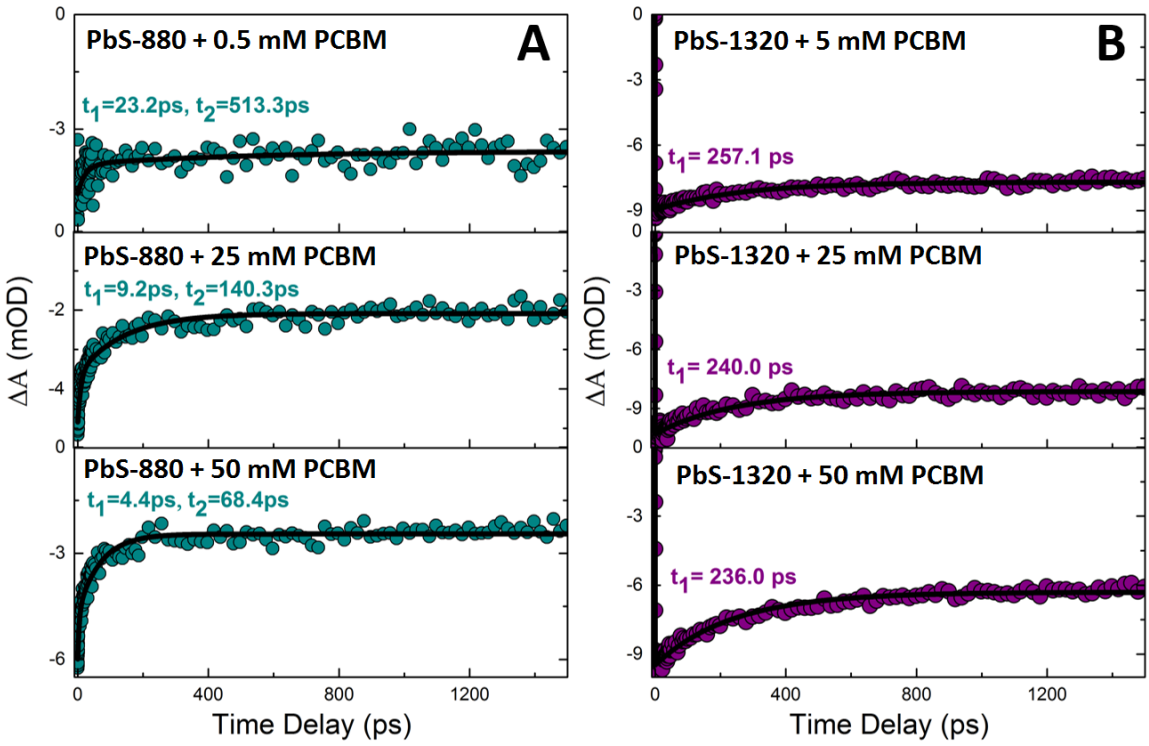

Figure 3.9 Time scales from the TA spectra at the GSB of PbS-880 (A) and PbS-1320 (B), upon the addition of different concentrations of PCBM.

An overall comparison of the GSB recovery kinetics of different PbS QD sizes, upon PCBM addition, is depicted in Figure 3.10. The plots clearly show a fast GSB recovery upon addition of PCBM to PbS-880, followed by a slow component. While the kinetic traces of PbS-1320 show only the slow component upon addition of PCBM. Finally, PbS-1470 (d_{QD} ≈ 5.5 nm) reveals the lack of both components in the dynamics behavior, thus demonstrating that all the size contribution within this sample is inactive for electron transfer to PCBM. This evidence supports the fact that CT can be tuned by the quantum confinement effect (with respective energy-level alignment) and QD size distribution.

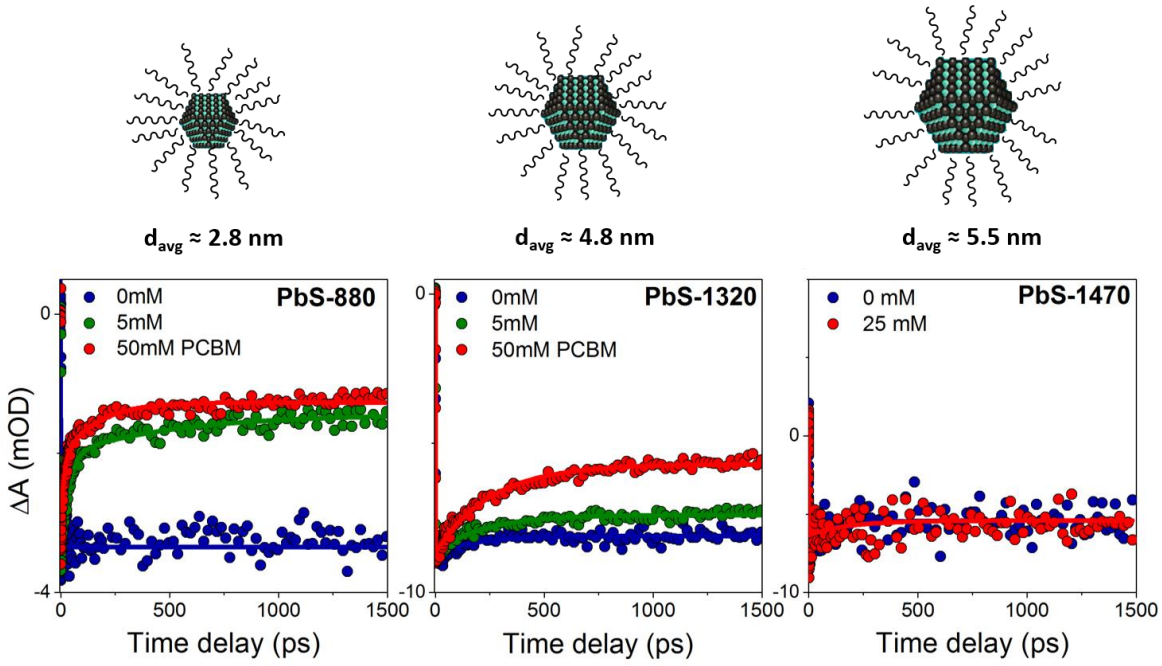

Figure 3.10 The GSB recovery kinetics of different PbS QD sizes (blue traces), and solutions of PbS with low (green traces) and high (red traces) PCBM concentrations. The solid lines are fits of the kinetic traces.

Chapter 4. CHARGE TRANSFER AT LARGE QUANTUM DOTS INTERFACE

4.1 Introduction

One of the most important scientific and technological challenges of this century is the design of cost-effective next-generation PVs that operate efficiently over the broad solar irradiance spectrum range. QD-based solar cells, especially those based on PbS QDs, have emerged as promising candidates because of the QDs' size-tunable bandgaps, high absorptivity coefficients, solution-processability, and facile synthesis. Moreover, these QDs exhibit a unique ability to increase the PCE beyond the theoretical Shockley-Queisser limit by utilizing multiple excitons,[64-67] and designing multi-junction PVs[6,12,44] that harvest different portions of light based on the same material. In particular, stacking junctions of QDs with different bandgaps maximizes the spectral capture efficiency, and raises the PCE ultimate limit from 31% to 42% (for double junctions) and to 49% (for triple junctions), Figure 4.1.[43-45] This technique requires the employment of a transparent interlayer between the junctions which is capable of combining the holes from the bottom cell with the matching electrons from the top cell.[147,148] Accordingly, the absorbed photon spectrum should be equally divided between the adjacent junctions to satisfy current-matching at the recombination layer.[149] Upon optimizing individual cells and satisfying the current-matching condition, an ideal multi-junction should exhibit an additive V_{oc}, which equals to the sum of open-circuit voltages produced by the constituent cells.[149]

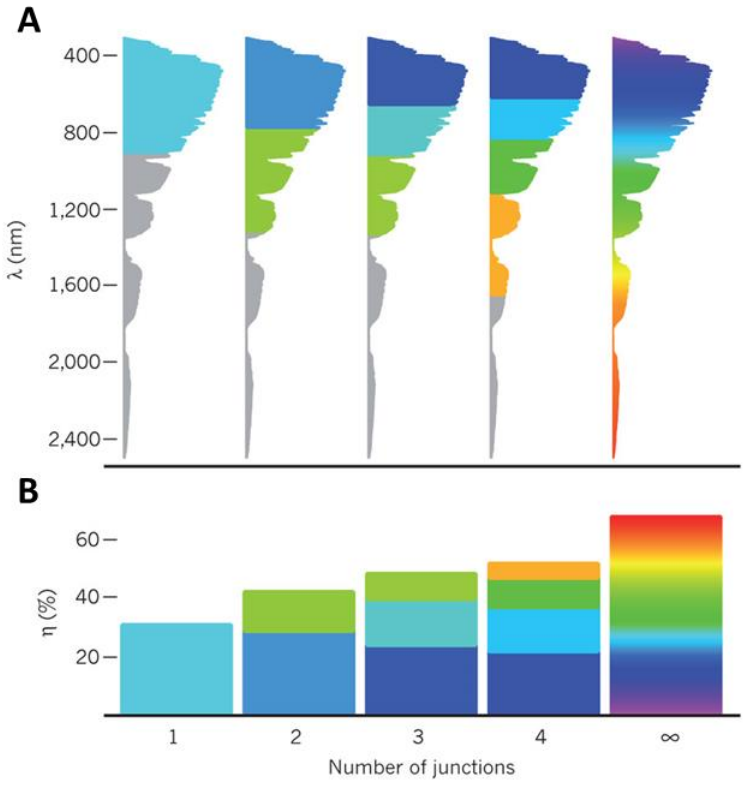

Figure 4.1 A) Schematic showing the broadband solar spectrum and the optimal bandgap regions for single junction and multi-junctions. B) Schematic for the theoretical efficiencies of PVs based on single junction and multi-junctions.[6]

In fact, researchers have attempted to fabricate tandem solar cells based on the size-quantization effect of PbS QDs, and have thus far successfully utilized QDs with E_g values of 1.6 and 1.0 eV for the first and second junctions, respectively.[149,150] The first cell absorbs photons with energy greater than 1.6 eV, while the second cell absorbs photons with energy between 1.0 and 1.6 eV. These tandem PV devices achieved an additive V_{OC} of their individual cells, and boosted the overall PCE.[149,150] Yet, light harvesting from large PbS QDs (E_g < 1 eV) remains one of the greatest challenges

precluding the development of PbS QD-based solar cells because the interfacial CT from such QDs to the most commonly used electron acceptor materials is very inefficient, if it occurs at all. The results in Chapter 3 have shown clearly that only small PbS QDs ($E_g \geq$ 1.0 eV, $d_{QD} \leq 4.3$ nm) are capable of injecting electrons to PCBM upon optical excitation, which is explained by such QDs exhibiting Type II interfacial band alignments. Similarly, only small PbS QDs were reported to demonstrate effective CT to inorganic electron scavengers such as TiO_2 nanoparticles,[77] and SnO_2 nanoparticles.[110] These findings were further supported by a considerable reduction in the device PCE when QDs with larger diameters are used;[151,152] thus limiting the energy harvested from the Sun's broad spectrum.

The hindered ability for engineering efficient wide-range tandem cells necessitates considering other electron acceptor material that enable efficient CT from both small and large QDs. In an effort to extend the effective spectral-edge of operation towards longer wavelengths, researchers have combined PbS QDs with 1-Dimensional TiO_2 nanotubes, whereby the lower conduction band potential of TiO_2 nanotubes compared to TiO_2 nanoparticles extended the effective bandgap for CT to 0.89 eV, while still excluding efficient CT from QDs of larger diameters ($E_g \sim$0.81 eV, $d_{QD} \sim$6 nm).[133] Bearing in mind that the CT is not merely dictated by the ionization potential of the donor and the electron affinity of the acceptor, but it could also be affected by donor-acceptor distances and electronic coupling,[39,40,121,153] we aim to explore the CT with other acceptor material that bring about additional surface interaction with the QDs, to

facilitate closer molecular proximity between the donor-acceptor pair. In particular, we test the interaction between negatively-charged PbS QDs and neutral or charged porphyrin units. Porphyrin-based electron acceptors were chosen for this study because of their chemical- and photo-stability,[154] their wide use in PVs,[154,155] their suitable reduction potentials,[156] and their peripheral substituents' versatility.[157] We study the CT and CS kinetics at PbS QD/porphyrin interface upon size-tuning the QDs to absorb different portions of the infrared spectral region. Quantitative data on CT dynamics can be directly resolved, with high precision, by applying broadband pump−probe spectroscopy to excite and detect the wavelengths around the first exciton absorption peak. We combine broadband fs-TA spectroscopy and PL quenching measurements to investigate the effect of QD size variations, and QD-porphyrin surface interaction, on the dynamics of CT from negatively-charged PbS QDs to neutrally and positively-charged porphyrins.

4.2 Surface Passivation and Ligand Exchange

This study requires the dispersion of PbS QDs in a polar medium to conduct the CT investigation with porphyrin units. Accordingly, exchange of oleic acid ligands for 1-thioglycerol (TG) ligands was carried out according to Fischer *et al.*,[158] to disperse the QDs in dimethyl sulfoxide (DMSO). Briefly, the solution-phase ligand exchange procedure involved dissolving TG in DMSO (25 mg/mL) and mixing it with an equal volume of oleic acid-capped QDs in octane (4 mg/mL). The biphasic system was vortexed vigorously for 30 seconds, resulting in the migration of QDs from non-polar to

polar phase. The polar phase was then separated by centrifugation, and rinsed several times to remove excess ligands. Further experimental details are available in Appendix A, section A.5. However, these TG-capped PbS QDs showed significantly lower PL and an increased GSB recovery upon bandgap excitation in TA measurements, thus signifying non-radiative recombination of charge carriers, Figure 4.2. This can be explained by the occurrence of trap states and imperfectly passivated surface upon ligand exchange.[56,59] In fact, previous studies have shown that steric hindrance among organic ligands can prevent them from reaching the whole surface of QDs, thus causing the existence of unpassivated metal surface sites.[56] Accordingly, additional surface passivation steps were required to restore the QDs' long exciton lifetime.

Halide (*e.g.* chloride, iodide, *etc.*) passivation techniques have emerged as robust passivation methods due to the compact size of atomic ligands and their resistivity towards oxidation.[50,56,159] In fact, halide atoms are sufficiently compact to infiltrate and passivate the otherwise difficult-to-access sites by bulky organic ligands.[50,56,59] For instance, researchers have found that introducing a metal halide salt during QD synthesis is effective in reducing deep trap states upon the binding of halide ligands, while the metal cation affects the shallow trap state density near the CB edge.[59] Herein, halide-passivated PbS QDs were prepared according to the method of Ip *et al.*,[56] by injecting cadmium chloride ($CdCl_2$) during the QD synthesis process. Additional experimental details are available in Appendix A, section A.4. Notably, the halide

treatment step was critical for better passivation of the surface, thus preserving the QDs' carrier lifetime after ligand exchange, Figure 4.2.

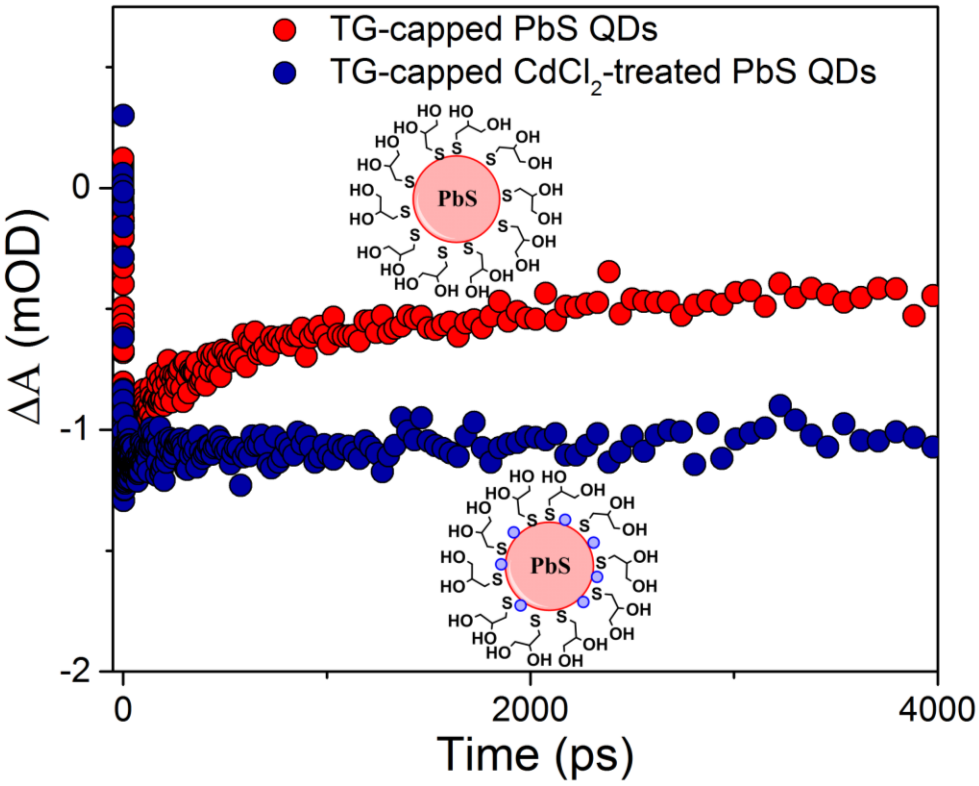

Figure 4.2 fs-TA kinetics traces at the GSB of similar-sized PbS QDs (PbS-1000) after ligand exchange to TG. Upon $CdCl_2$-treatment, the QDs show acceptable recovery kinetics after ligand exchange.[160]

The ligand exchanged $CdCl_2$ -treated QDs were characterized by XPS; experimental details are available in Appendix A, section A.7. The XPS data confirmed the binding of cadmium and chloride to the QDs (Figure 4.3C and D) in good agreement with previous reports.[56] Additionally, TG binding to the QDs was confirmed through the appearance of

an additional higher binding energy sulfur species signal with the S $2p_{3/2}$ component at 161.6 eV (Figure 4.3B), in perfect agreement with literature results.[158]

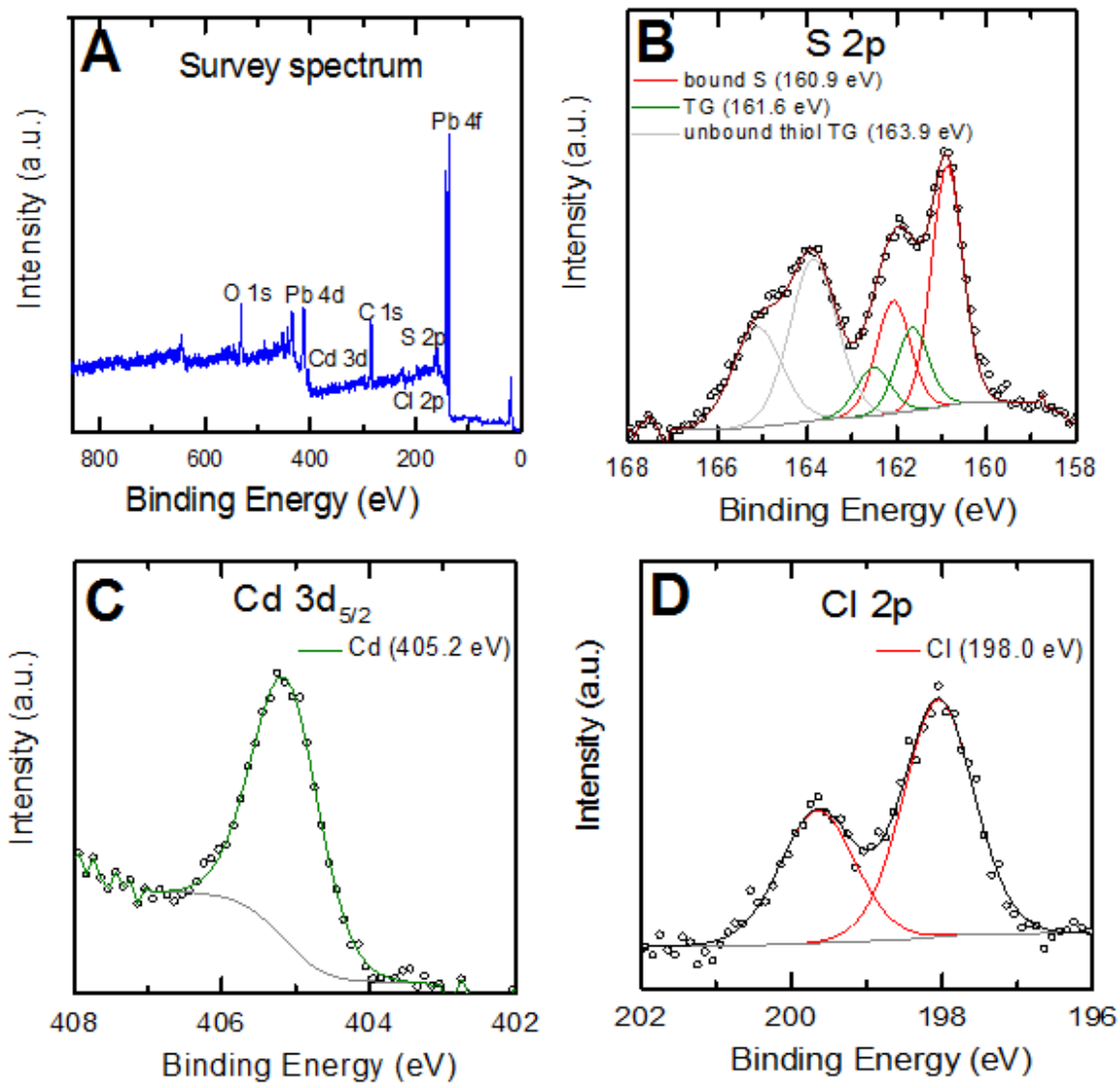

Figure 4.3 XPS data showing the composition of TG-capped $CdCl_2$-treated PbS QDs, where (A) reveals the survey XPS spectrum, while (B), (C), and (D) are peak enlargements for sulfur, cadmium, and chloride, respectively. For all the spectra, the mentioned peak positions belong to the lower binding energy components.[160]

For this study, we synthesized QDs of different sizes, as inferred from their first excitonic absorption peaks (840, 1000, 1300, 1550 nm) that correspond to E_g between 1.48 eV-0.80 eV. Herein, we refer to the QD samples based on the wavelength of the first exciton absorption peak; *i.e.* the sample with the $1S_h \rightarrow 1S_e$ peak at 840 nm is named PbS-840.

The synthesized QDs were characterized by TEM to obtain structural and size information; see appendix A, section A.8 for experimental details. The obtained images confirmed the maintenance of a uniform spherical shape and size distribution after the ligand exchange, Figure 4.4. The average core sizes of the QDs were calculated by measuring the diameter of ~150 particles. For instance, the average core diameters for PbS-1300 and PbS-1550 were found to be 4.8 ± 0.5 nm and 6.1 ± 0.4 nm, respectively. These results are in very good agreement with the model proposed by Moreels *et al.,*[125] which predicts an average size of 4.6 nm and 5.9 nm, for PbS-1300 and PbS-1500, respectively. Furthermore, the QD size distribution and average size for the different QD samples were also confirmed by dynamic light scattering (DLS) measurements. The experimental method is described in Appendix A, section A.12, while the supporting results are shown in Appendix B, section B.3.

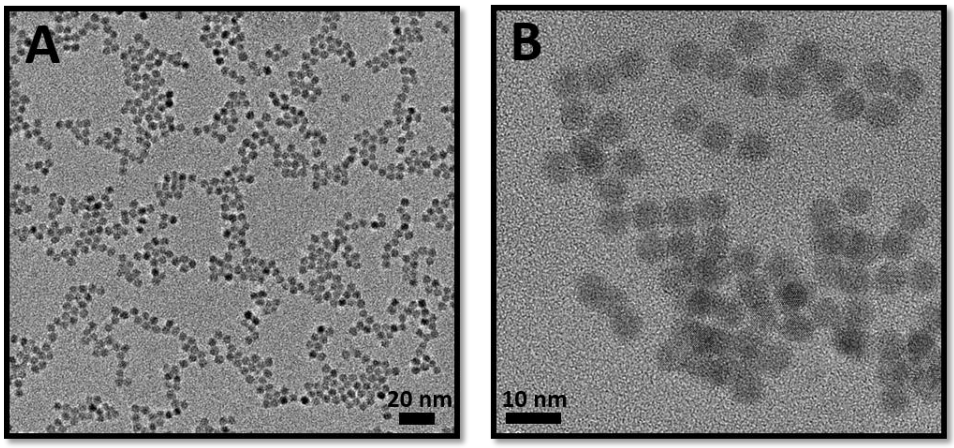

Figure 4.4 Representative TEM images of the TG-capped $CdCl_2$-treated PbS QDs where (A) and (B) are PbS-1300 and PbS-1500, respectively.

Then, we pursued a Zeta-potential measurements for the QD dispersions in DMSO, to evaluate electrostatic potential that exists at the slipping plane of a particle, which is related to both surface charge and the local environment of the particle.[161] In other words, the measurement represents the potential difference between the dispersion medium and the stationary layer of fluid attached to the dispersed QDs.[161] The experimental details are provided in Appendix A, section A.12. The Zeta-potential measurements revealed a negatively-charged surface for these QDs (Figure 4.5), in agreement with previous report by Sargent and co-workers.[158] Yet, we obtained a more negative value with our QDs compared to their reported Zeta-potential of -7.0 mV; which could be due to the extra passivation step, in which chloride ions were proven to constitute a higher percentage than cadmium ions, as indicated clearly from the atomic composition obtained by our XPS measurements, Appendix B, section B.3. Due to the

negatively-charged surface of these QDs, we test their interfacial charge transfer with neutral and positively-charged acceptor molecules, as described in the following section.

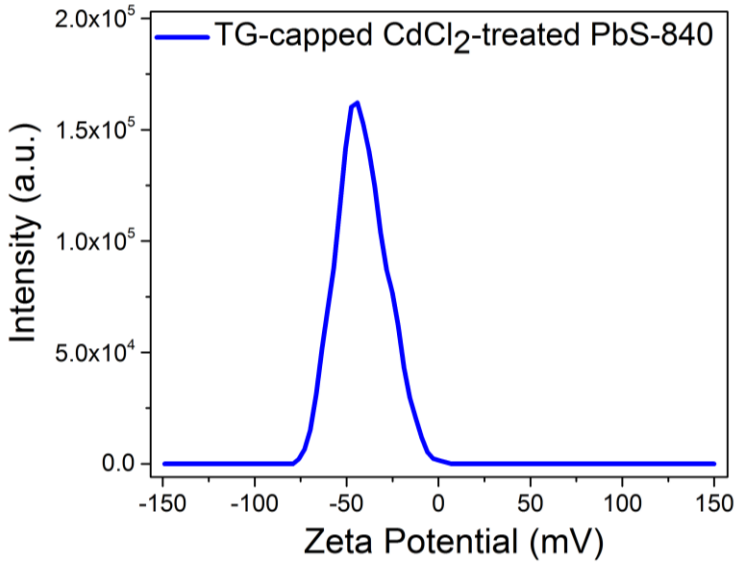

Figure 4.5 Zeta-potential measurement of TG-capped $CdCl_2$-treated PbS QDs.[160]

4.3 Interfacial Charge Transfer Measurements

Herein, we employed the positively-charged free-base porphyrin 5,10,15,20-tetra(*N*-methyl-4-pyridyl)porphyrin (TMPyP), and the neutrally-charged free-base porphyrin 5,10,15,20-tetra(4-pyridyl)porphyrin (TPyP), whose structures and absorption spectra are depicted in Appendix B, section B.1. These highly conjugated heteroaromatic compounds typically have a very intense absorption between 400–450 nm, along with moderate bands in the 500–650 nm spectral region.

For the steady-state quenching measurements, the stock TG-capped $CdCl_2$-treated PbS QDs dispersions were diluted with DMSO to maintain a constant concentration

(~1.5×10^{-6} M), as determined by the optical density at the first exciton absorption peak (*i.e.* $1S_h \rightarrow 1S_e$ transition) within a 1 cm path length quartz cuvette. Alternatively, the stock solutions were diluted with different concentrations of porphyrin (TMPyP or TPyP) in DMSO while maintaining a fixed QDs concentration. Further experimental details are available in Appendix A, section A.10.

For the transient absorption measurements, the stock PbS QDs were diluted with extra DMSO, or alternatively porphyrin (TMPyP or TPyP) in DMSO, while maintaining a fixed QD concentration (~1.5×10^{-6} M) as determined by the optical density at the first exciton absorption peak within a 2 mm path length cuvette. All TA experiments were conducted at room temperature, with constant sample stirring to avoid the photocharging of the QDs.[128,129] The absorption spectrum of each sample measured before and after TA experiments did not show any degradation. Further experimental and instrumental details are available in Appendix A, section A.11.

4.4 Results and Discussion

Figure 4.6 shows the changes in the steady-state absorption and PL spectra of small (PbS-840) and large (PbS-1300) QDs, upon the addition of different concentrations of the positively-charged porphyrin, TMPyP. The successive addition of TMPyP resulted in efficient quenching of the PL of the QDs. This result suggests that photo-induced CT occurs between the QDs and TMPyP, causing the deactivation of the exciton radiative recombination process as TMPyP concentration—[TMPyP]—is increased. It is worth pointing out that although fluorescence quenching could also be achieved by energy

transfer, we rule out this mechanism here on the basis of the lack of spectral overlap between the absorption of TMPyP and the emission of the QDs, as clarified in Appendix B, section B.1.

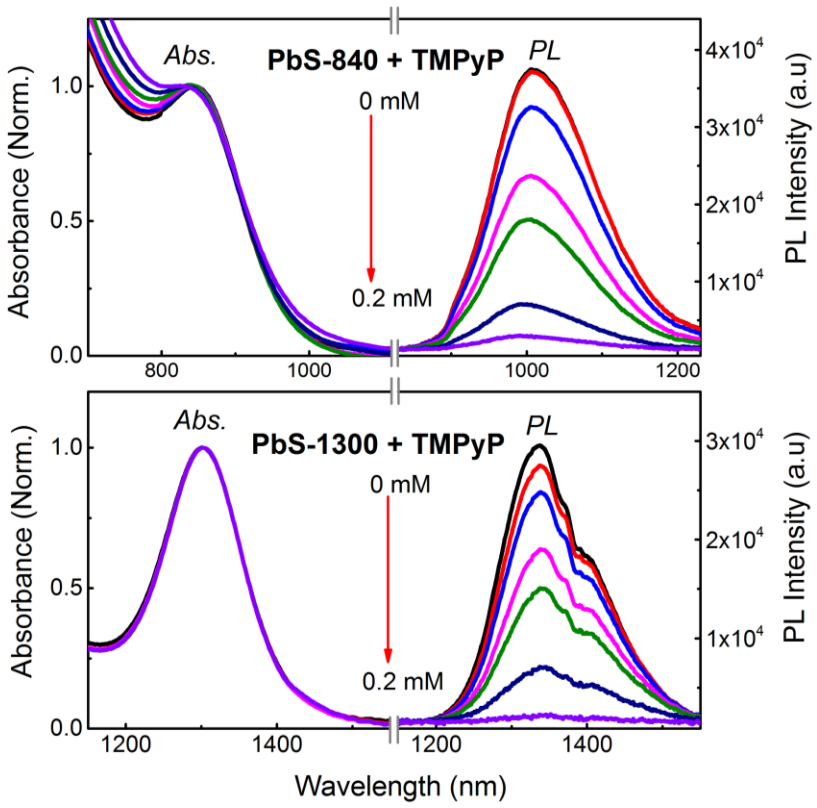

Figure 4.6 Absorbance and PL spectra of PbS-840 and PbS-1300 upon the addition of different concentrations of TMPyP, in DMSO-d_6. The PL spectra were recorded upon excitation with λ_{ex} = 840 nm and λ_{ex} = 1300 nm, respectively. The green traces signify the addition of 0.08 mM TMPyP.[160]

For PbS-840, the addition of 0.2 mM TMPyP reduced the PL emission to nearly nil and resulted in a slight blue shift of both the first exciton absorption peak (approximately 15 nm) and the PL peak (approximately 12 nm). These spectral shifts

may originate from modifications in the electronic density and confinement energy of the QDs, which are characteristic of the ground-state complex between a ground-state fluorophore and a quencher, in agreement with previous reports.[133,162] Unlike our previous study between oleic acid-capped PbS QDs and PCBM (discussed in Chapter 3), large TG-capped QDs (PbS-1300) exhibit complete PL quenching with TMPyP, Figure 4.6. Although the extents of the spectral shifts were negligible compared to those of PbS-840, the significant PL quenching implies efficient electronic coupling between TMPyP and PbS-1300 in the excited state. The minimized spectral shifts upon TMPyP addition to larger QDs could be the result of the lessened electronic coupling in the ground state as indicated by the minimized binding constants obtained from the modified Stern-Volmer plots (Appendix B, section B.2). This behavior could be explained by the reduced free-energy (–ΔG) driving force for the CT as larger QDs are employed (Appendix B, section B.3). It is worth mentioning that the energy levels of the QDs were estimated with the aid of ultraviolet photoelectron spectroscopy (UPS) measurements to take into account the effect of the ligand-induced modifications on the absolute energy levels of the QDs.[55] The experimental method is described in Appendix A, section A.7, while the supporting results are shown in Appendix B, section B.3. Interestingly, drastic PL quenching was also observed upon the addition of TMPyP to PbS-1550 (E_g = 0.8 eV, d_{QD} ≈ 6 nm) as shown in Figure 4.7. Importantly, this is the first time to report CT from such size of PbS QDs to molecular acceptor. A further consideration for donor-acceptor systems in the solution phase is whether PL quenching occurs *via* 1) static quenching, whereby a non-luminescent ground-state complex is formed, and/or 2) dynamic

quenching, which involves collision. In this regard, the Stern-Volmer (SV) plots[137] of small and large QDs revealed upward curvatures (Appendix B, section B.2), thus indicating the incorporation of both quenching mechanisms depending on the [TMPyP].[137,163]

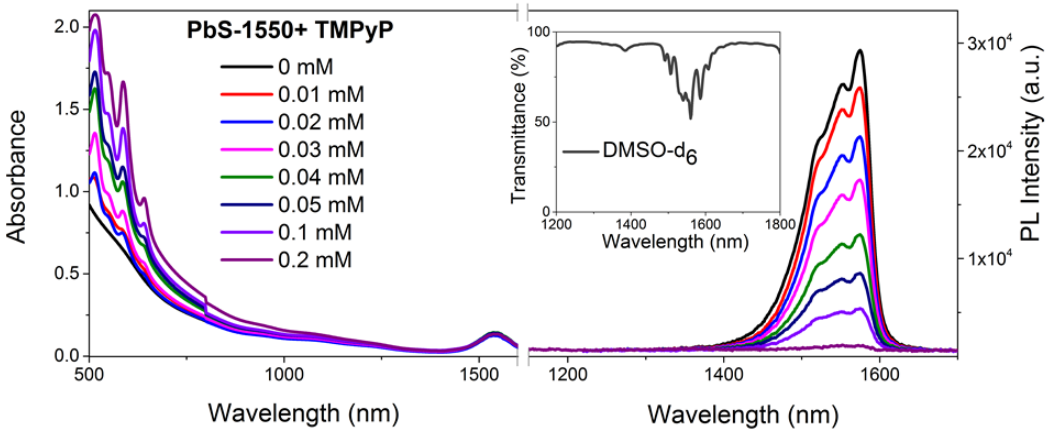

Figure 4.7 Steady-state absorption and PL spectra of PbS-1550 upon the addition of different [TMPyP], in DMSO-d_6. The PL spectra were recorded upon excitation with λ_{ex} = 1100 nm. Note: the structures in PL spectra are a result of the solvent absorption in this region, as shown in the inset transmittance profile.[160]

Next, we employed femtosecond transient absorption (fs-TA) spectroscopy to study the ground-state bleach (GSB) dynamics upon bandgap excitation of the QDs. Because the GSB signal is directly associated with the electron population in the conduction band, we used it as a convenient probe to follow the CT and CR dynamics at the QD interface. In particular, in addition to probing the formation of the porphyrin anionic species, we used the GSB signal to follow the charge recombination dynamics resulting

from the CT process. The TA measurements of different PbS QD sizes were recorded following laser pulse excitation at approximately 1.3 times the bandgap to avoid any contribution from the scattered light in the GSB signal, thus assuring high-quality data and accurate dynamics for the CT process. Further details of the TA experimental apparatus and conditions are provided in the Appendix A, section A.11. Figure 4.8A shows the fs-TA spectra of large QDs (PbS-1300) recorded as the concentration of TMPyP was increased. The pristine PbS QDs exhibited a very small decay (< 15%) of the GSB on the picosecond (ps) time scale, which is attributed to state trapping (which lies just below the first confined electron state);[142] these results are consistent with those of previous reports[115,164] and indicate that most excited QDs are in long-lived single exciton states under these experimental conditions. The addition of TMPyP to solutions of PbS QDs accelerates the GSB recovery on the picosecond time scale. The boosted bleaching recoveries suggest the presence of an alternate deactivation pathway for the separated charges: CR following a CT process.

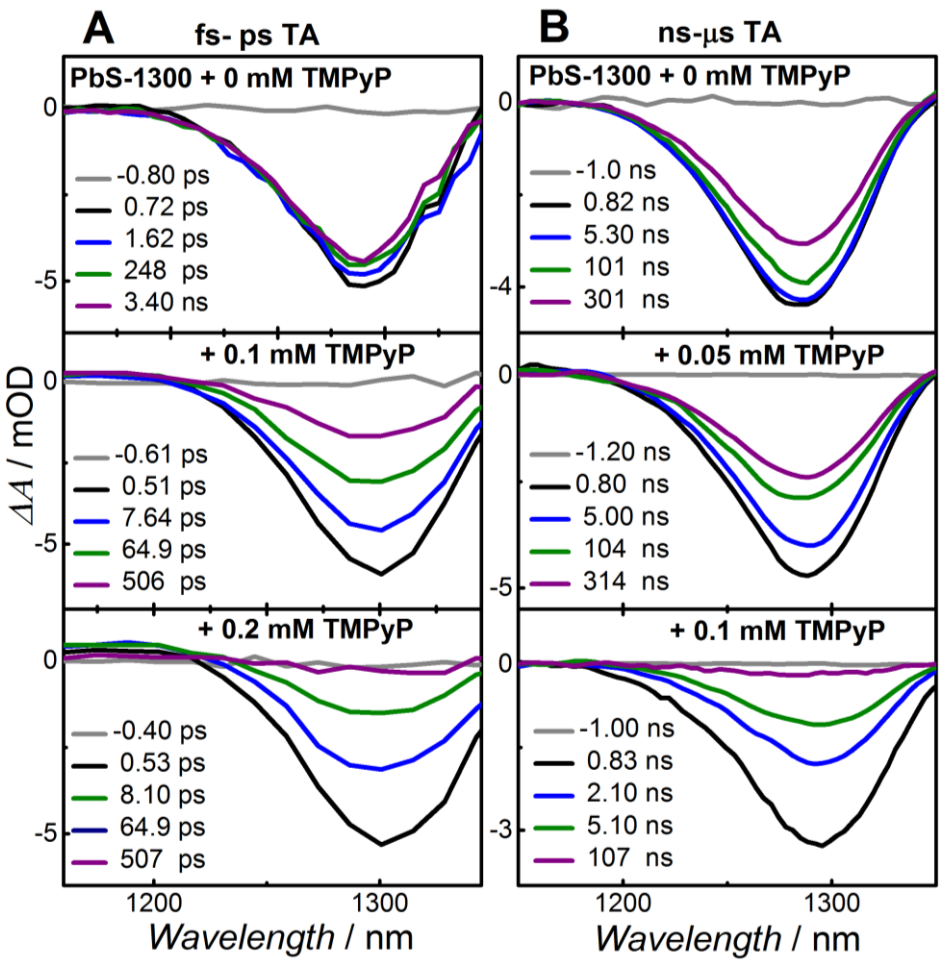

Figure 4.8 fs-ps TA (A) and ns-μs TA (B) spectra of PbS-1300 upon the addition of different [TMPyP], with $\lambda_{ex} = 1.3E_g$ in DMSO-d_6.[160]

On the basis of the energy-band alignments shown in Appendix B (section B.3), assisted by electrostatic interaction between the negatively-charged QDs surface and the positively-charged molecular acceptor, we attribute the exciton quenching to the ultrafast electron transfer from the photo-excited PbS QDs to TMPyP, which is expected to generate TMPyP anion radical species (TMPyP$\bullet^-$) with a characteristic broad peak between 700 and 800 nm.[165,166] By monitoring the fs-TA in the visible region for both

small and large QDs, we deciphered the signal for electron injection from the photo-excited PbS QDs to TMPyP through the evolution of TMPyP•⁻, with a temporal resolution of approximately 120 fs (Figure 4.9). The ultrafast electron injection to TMPyP as inferred from the formation of its anionic species, and the ultrafast CR as inferred from the ultrafast GSB recovery, are further indications of the ground-state complexation and subsequent static CT between the TG-capped PbS QDs and cationic porphyrin. This could also indicate that the molecular acceptor is likely to be adsorbed on the surface of QDs, which is consistent with previous reports.[51,114,167,168]

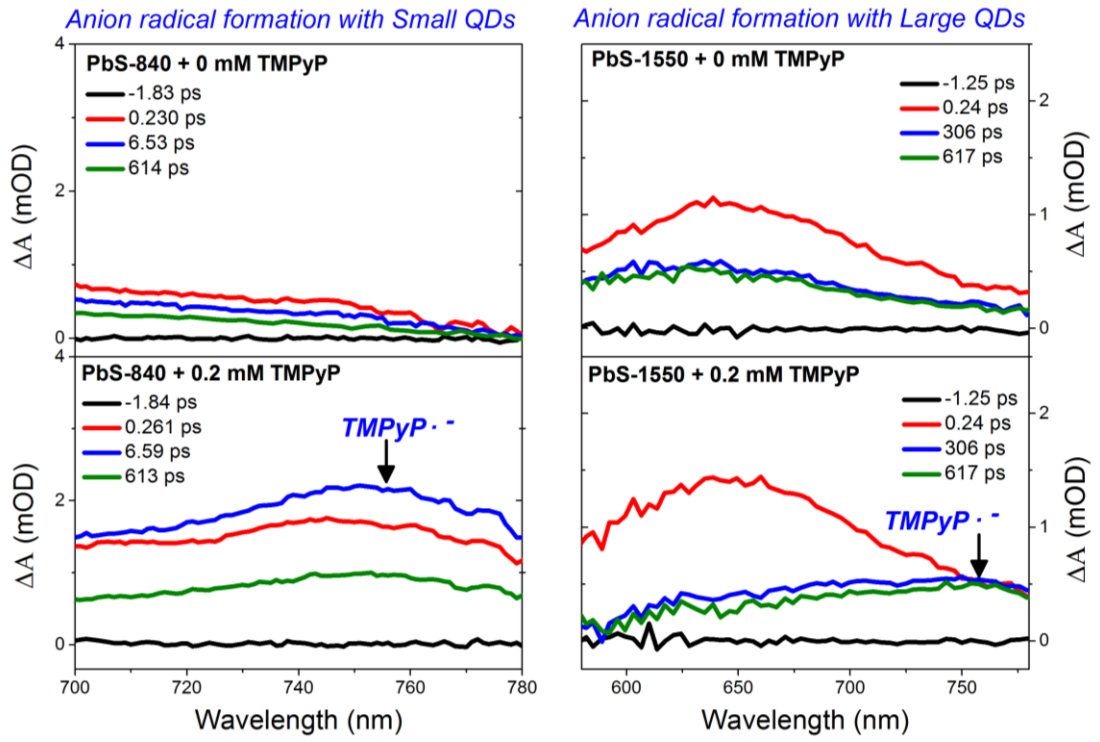

Figure 4.9 fs-TA spectra of PbS-840 and PbS-1550, in the visible region, with $\lambda_{ex} = 1.3E_g$ in DMSO-d_6. The spectra, in comparative timescales, show the evolution of TMPyP anion radical after excitation of small and large QDs in solution.[160]

Figure 4.10 shows a comparison of the kinetic traces extracted from the GSB feature within the fs-TA spectra of different PbS QD sizes upon the addition of a fixed [TMPyP]. The dynamics were fit to double-exponential functions with time constants of a few to tens of picoseconds, and tens to hundreds of picoseconds. The two observed components suggest the occurrence of two types of donor-acceptor ions pairs with different associated couplings/distances which can be differentiated by their different recombination dynamics, in accordance with previous reports on other donor-acceptor systems.[126,146,169] The fittings for the bleach recoveries of PbS-840, PbS-1000, and PbS-1300 indicate that not only is the percentage recovery greater for smaller PbS QDs, but the rate of CR is also enhanced with the smaller QD size. For instance, the recovery time constants due to carrier recombination for PbS-840 are 7.4 and 87.5 ps at 0.1 mM TMPyP, and they elongate to 25.8 and 572.2 ps for PbS-1300 with similar [TMPyP], thus indicating that the CR varies strongly as a function of QD size. The differences in the recombination rates/percentages indicate variation in the CT rates between various QD sizes and TMPyP. In addition, the system reveals a clear dependence not only on the free energy driving force between the donor and acceptor units[170] (Appendix B, section B.3); but also on the presence of the charged molecular acceptors (as clarified in below discussion with TPyP). Because of their increased bandgaps, smaller QDs are expected to have more favorable CB energies for injecting electrons into TMPyP. Notably, although we did not measure the GSB recovery kinetics for PbS-1550 because of a lack of sufficient white light in this region within our TA setup, the steady-state PL spectra (Figure 4.7) provide sufficient evidence for the CT to TMPyP.

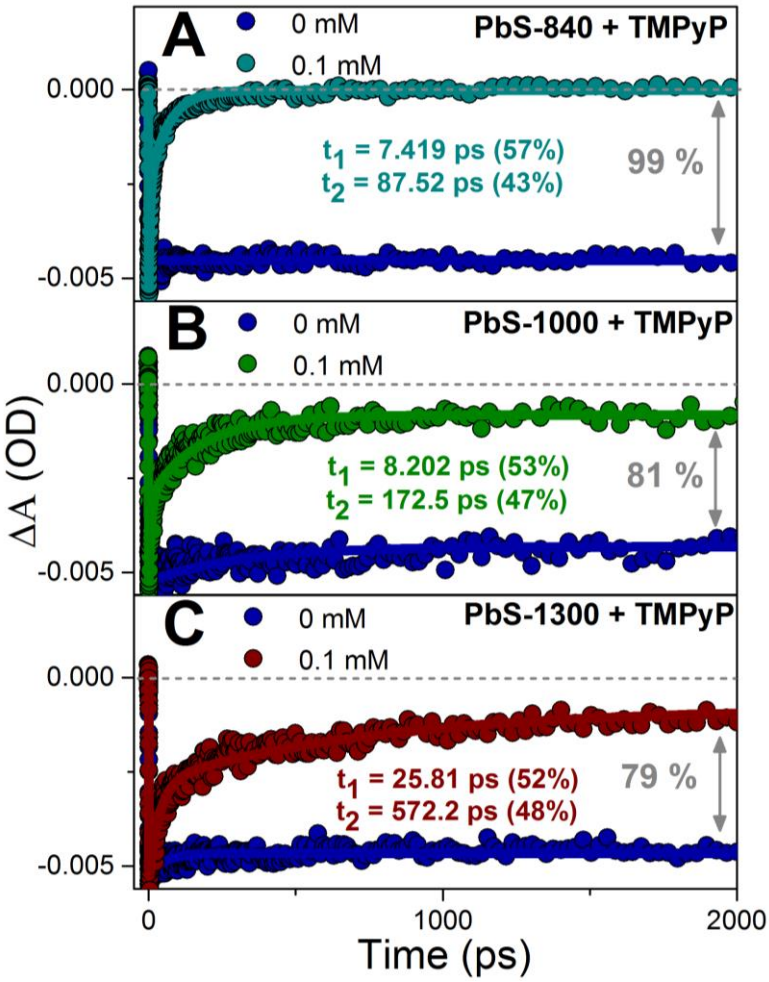

Figure 4.10 fs-TA kinetics traces at the GSB of PbS QDs with different sizes upon the addition of 0.1 mM TMPyP, with $\lambda_{ex} = 1.3E_g$ in DMSO-d_6.[160]

To explore the possibility of electron transfer through diffusion control process, we employed nanosecond (ns) TA spectroscopy to demonstrate that TMPyP quenches the excited state of the large QDs on the microsecond time scale (Figure 4.8B and Figure 4.11). The exciton quenching on the nanosecond-to-microsecond time scales is due to a dynamic mechanism, whereby collisionally gated CT occurs between the QDs and freely diffusing TMPyP molecules. This observation provides further evidence for the

involvement of both static and dynamic mechanisms in describing the overall quenching process, in agreement with other reported QD/molecular acceptor systems.[51,167] The results of the nanosecond TA studies were consistent with the results of the PL quenching measurements, as shown in Figure 4.11 and Figure 4.6, respectively. The nanosecond TA studies revealed that the addition of 0.08 mM TMPyP resulted in the evolution of a new fast decay component and maintenance of approximately 67% of the QD population with an elongated lifetime of 0.98 µs. Similarly, the PL quenching measurements revealed that, upon the addition of 0.08 mM TMPyP to PbS-1300 (green traces), approximately 64% of the QD population maintained an active PL.

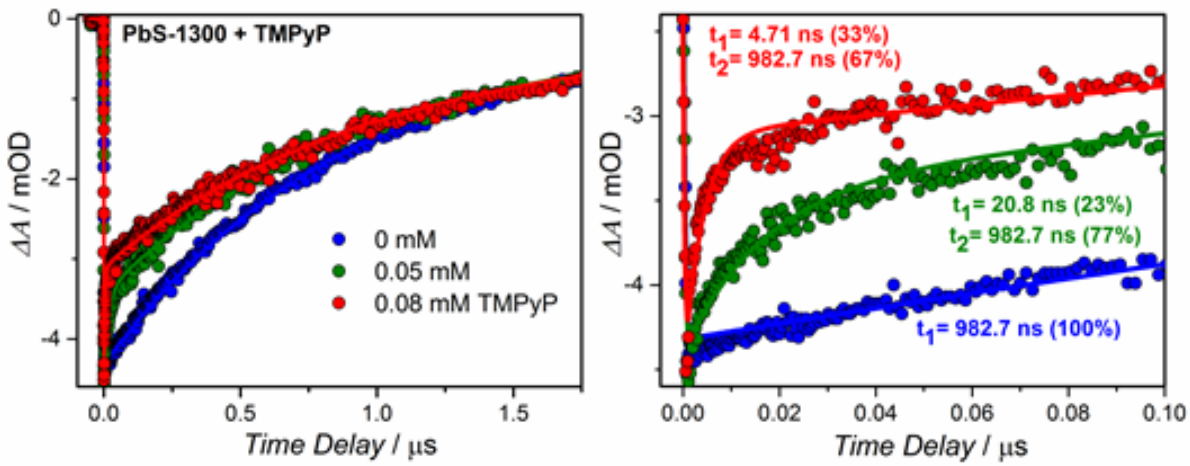

Figure 4.11 ns-µs TA kinetics at the GSB for PbS-1300 with λ_{ex} = 900 nm, in the long time-scale (Left). Upon TMPyP addition, a double exponential function arises as clarified in the short-time window (Right). By fixing t_2 value to the lifetime of pure QDs (982.7 ns), it is clarified that its amplitude decreases upon TMPyP addition.[160]

We argue that, although the CT from PbS QDs to TMPyP is facilitated by their interfacial band energy level alignment, this CT is based primarily on the prior availability of intimate contact through the electrostatic interaction between the two moieties as an additional driving force, Figure 4.12. To confirm this hypothesis, we evaluated the interaction between PbS QDs and a neutrally charged free-base porphyrin, 5,10,15,20-tetra(4-pyridyl)porphyrin (TPyP), under the same experimental conditions. In this case, whereas TPyP has energy levels similar to those of TMPyP,[170,171] it lacks the positive charges that provide electrostatic interaction with the TG-capped QDs.

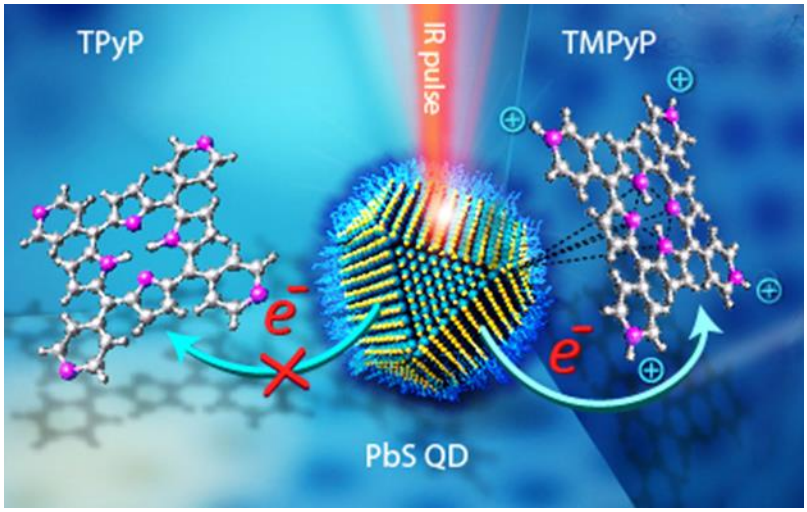

Figure 4.12 A schematic showing the presence and absence of the CT process upon IR-pulse excitation from PbS QDs to TMPyP and TPyP, respectively.[160]

Figure 4.13 shows that the addition of TPyP to PbS-1300 did not induce any PL quenching, nor significantly change the fs-TA kinetics. The complete absence of PL quenching between large PbS QDs and TPyP, and the lack of any differences in the QD's

lifetime upon TPyP addition (Figure 4.14), reveal the importance of electrostatic interaction as a key parameter in controlling the CT at QD interfaces and in providing a broader effective QD size range.

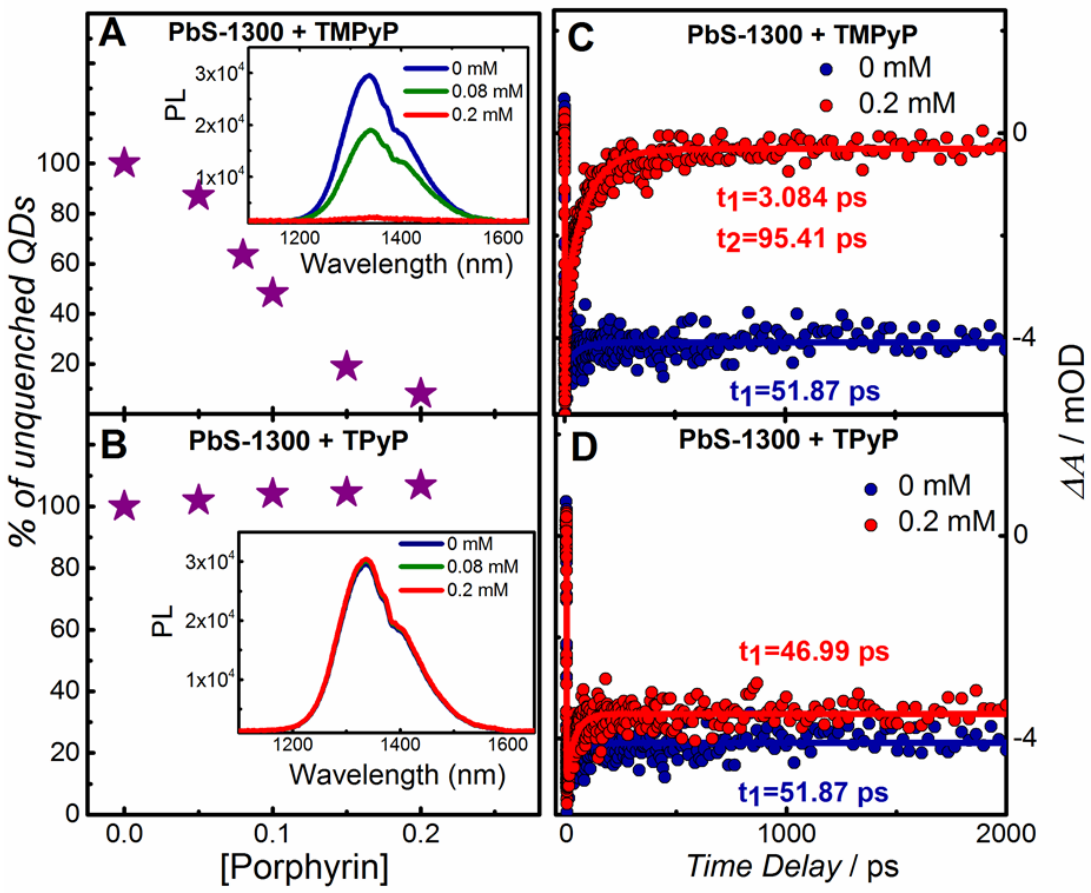

Figure 4.13 Plots of the percentage of unquenched QDs upon the addition of TMPyP (A) and TPyP (B), where the insets show the representative PL spectra. fs-TA kinetics at the GSB for PbS-1300 upon the addition of TMPyP (C) and TPyP (D).[160]

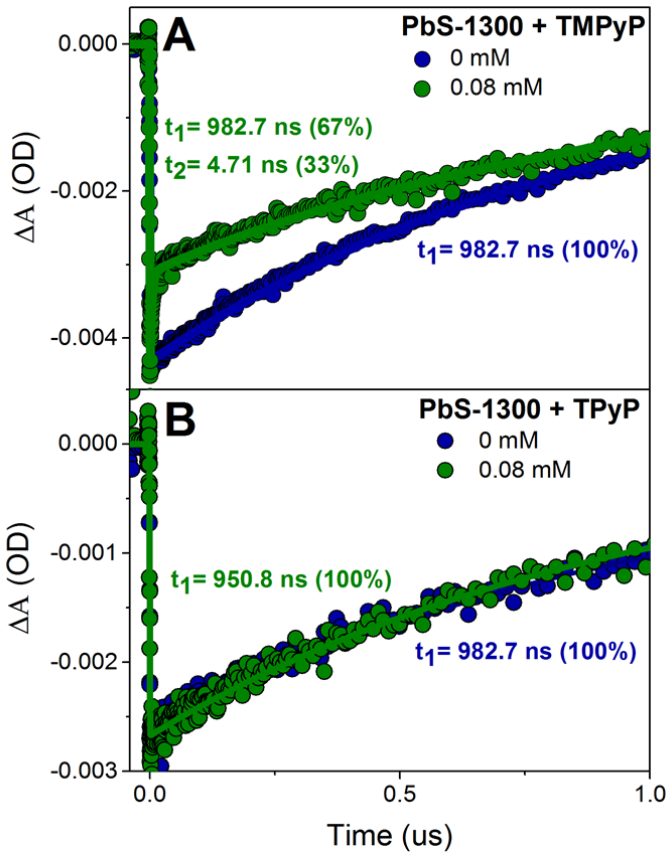

Figure 4.14 ns-µs TA kinetics at the GSB for PbS-1300 with $\lambda_{ex} = 1.3E_g$ upon the addition of TMPyP (A) and TPyP (B). The plot reveals the absence of the fast component evolution, and a nearly constant exciton lifetime when neutral TPyP is added.[160]

Moreover, the importance of the electrostatic interaction would be manifested if it can also facilitate CT at interfaces with a dis-favorable energy level alignment. Accordingly, we perform another control experiment for measuring the PL quenching upon the addition of an equally charged molecule that provides a dis-favorable energy level alignment with PbS QDs. For that purpose, we use ZnTMPyP, since the complexation of Zn^{+2} with porphyrin had been reported to induce a rise in the porphyrin

LUMO level by ~1.5 eV;[172] which should greatly inhibit CT from the QDs to the porphyrin species. Interestingly, complete PL quenching was recorded with three QD sizes (PbS-800, PbS-1300, and PbS-1500) upon the addition of ZnTMPyP (Figure 4.15), which suggests that the proximity of a cationic species could enhance charge transfer even with a slight dis-favorable energy level alignment.

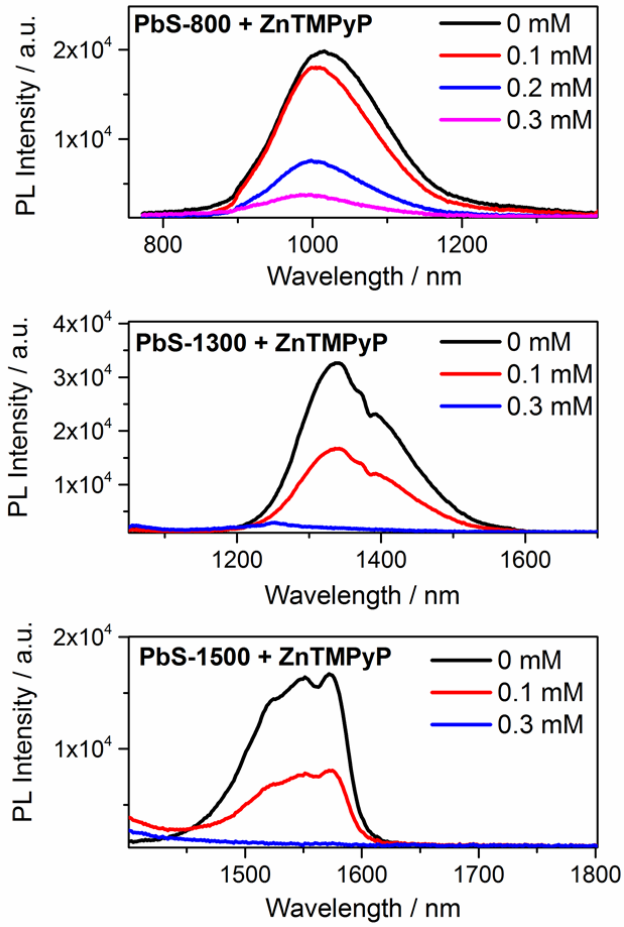

Figure 4.15 PL spectra of different PbS QD sizes upon the addition of different [ZnTMPyP], in DMSO-d_6. Complete PL quenching was recorded with the equally charged ZnTMPyP (compared to H_2TMPyP), irrespective of the dis-favorable energy level alignment with PbS QDs.[160]

Chapter 5. CONCLUSONS AND FUTURE DIRECTION

The unique properties of colloidal semiconductor QDs, such as their size-dependent electronic transition energies, their solution-processability, and their high surface-to-volume ratio, render them as promising components for various optoelectronic applications. Among the arising challenges for using QDs in solar energy conversion are the need for preparing high-quality materials on a large-scale, as well as controlling surfaces and interfaces to improve charge transfer for a wide range of QD sizes.

Notably, all prior reports of record-performance QD-based photovoltaics have been based on small-scale batch syntheses of PbS QDs. In Chapter 2, we discussed the development and optimization of a scalable synthesis methodology to obtain PbS QDs with high PLQY, narrow FWHM values, and good PV performance. Specifically, we find that only when using a dual-temperature-stage flow reactor synthesis—which serves in separating the nucleation and growth processes—are the QDs of sufficient monodispersity to achieve high PV performance. Importantly, the scalability of our optimized procedure is manifested by comparing the yield to the traditional batch synthesis. A typical dual-stage flow synthesis of PbS QDs yields approximately 2.4-2.5 g/hr, while a single batch synthesis setup yields around 0.5 g/hr. Improving the scalability and quality of these QDs through the adaption of an automated flow reactor method are key aspects of this work in order to create an industrially viable processes for producing QD-based PVs. This approach can also be extended to the synthesis of

other NCs and is thus a truly impactful process for the large-scale synthesis of materials for incorporation in devices.

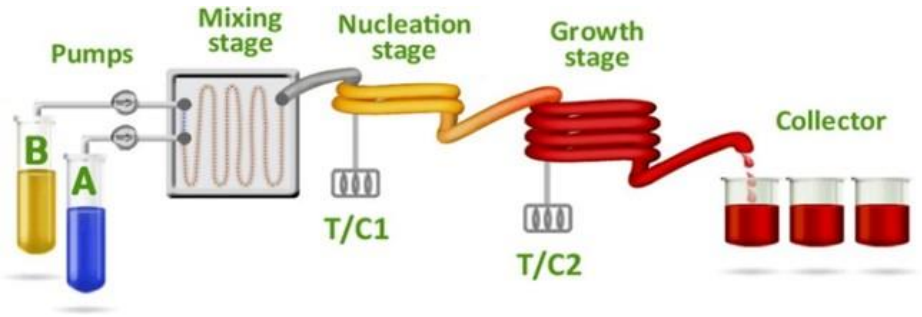

Figure 5.1 Schematic of the dual-stage flow reactor which yields scalable PbS QDs with high PLQY and narrow FWHM values, by utilizing separate nucleation and growth stages. In the schematic, A and B are lead and sulfur precursors.[98]

Importantly, the ability to size-tune the optical and electrical properties of semiconductor QDs provides vast flexibility to adjust the PV performance. Accordingly, understanding the dynamics of the electron injection at the surface of QDs is a key factor in determining the utility of these materials in such applications that principally rely on interfacial dynamics. Nevertheless, the charge transfer kinetics in the most promising QDs for PV, namely PbS QDs, remain largely unresolved. In Chapter 3, we investigated the charge transfer and separation at PbS QDs and phenyl-C_{61}-butyric acid methyl ester (PCBM) interface using a combination of fs-broadband TA spectroscopy and steady-state PL quenching measurements. We analyzed the electron injection and charge separation at PbS QD/PCBM interfaces for four different QD sizes and as a function of PCBM concentration. The results reveal that the energy band alignment,

tuned by the quantum size effect, is a key element for efficient electron injection and charge separation processes. More specifically, the data demonstrate that only small-sized PbS QDs—that satisfy a Type II interfacial band alignment with PCBM—can transfer electrons to PCBM upon light absorption; as inferred from the ultrafast formation of the anionic species (PCBM•⁻). Notably, the energy-level alignment can be controlled by tuning the size distribution of PbS QDs to achieve charge transfer kinetics ranging from highly efficient and ultrafast (< 120 fs) in small-sized QDs (E_g > 1eV), down to very low or even absent transfer for large QDs (E_g < 1 eV). Taken together, our results clearly demonstrate that charge transfer rates at QD interfaces can be tuned by several orders of magnitude by engineering the QD size distribution; thus revealing the importance of efficient size distribution engineering for the design and the understanding of QD interfaces for solar energy conversion.

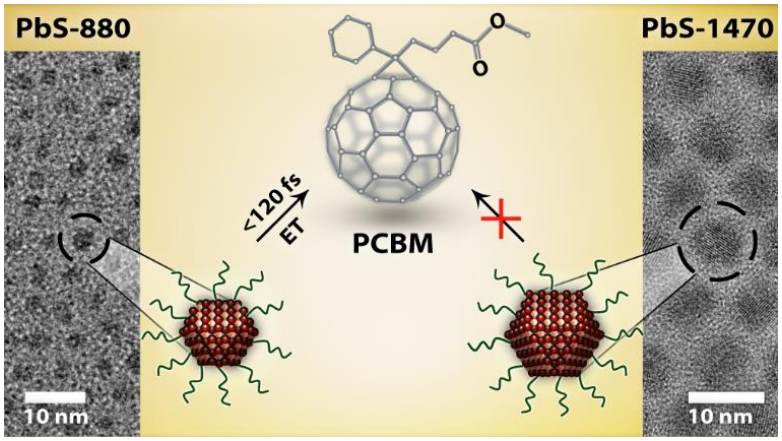

Figure 5.2 A schematic showing that quantum dot size makes a dramatic difference in tuning the electron injection at interfaces; here at PbS QD/PCBM interface.[126]

Another precluding challenge for designing QD-based PVs is the need for careful engineering of multi-junctions that harvest a wide range of the infrared solar spectral range. More specifically, it is essential to overcome the cut-off charge transfer bandgaps at PbS QDs interface by enhancing electron injection from large PbS QDs (E_g < 1 eV) to electron acceptors. In Chapter 4, we utilized ultrafast spectroscopic techniques to shine the light on the path towards employing the size-tunable QDs efficiently for charge transfer applications. In particular, we report the importance of an additional parameter, namely the electrostatic interaction, in providing suitable donor-acceptor configuration and controlling the charge transfer kinetics at QD interfaces. The interfacial electrostatic interaction between the negatively-charged PbS QDs and a positively-charged porphyrin acceptor (*i.e.* 5,10,15,20-tetra(N-methyl-4-pyridyl)porphyrin (TMPyP)) enabled widening the effective bandgap range for charge transfer from PbS QDs. We showed, for the first time, the occurance of an ultrafast and efficient electron transfer for PbS QDs of all sizes—including those with E_g < 1 eV—, as inferred from the drastic photoluminescence quenching and the ultrafast formation of the porphyrin anionic species (TMPyP•$^-$). Moreover, our time-resolved studies have shown that charge transfer at QD interfaces can be tuned by several orders of magnitude through the interplay between quantum confinement and interfacial electrostatic interaction. Upon extending the effective size range for charge transfer at the PbS QDs interface, one would be able to couple the faster electron injection rate of small QDs and the greater absorption range of large QDs to harvest different portions of the broad solar spectrum. Thus, this approach provides a new pathway for engineering

QD-based solar cells that make the best use of the diverse photons making up the Sun's irradiance spectrum.

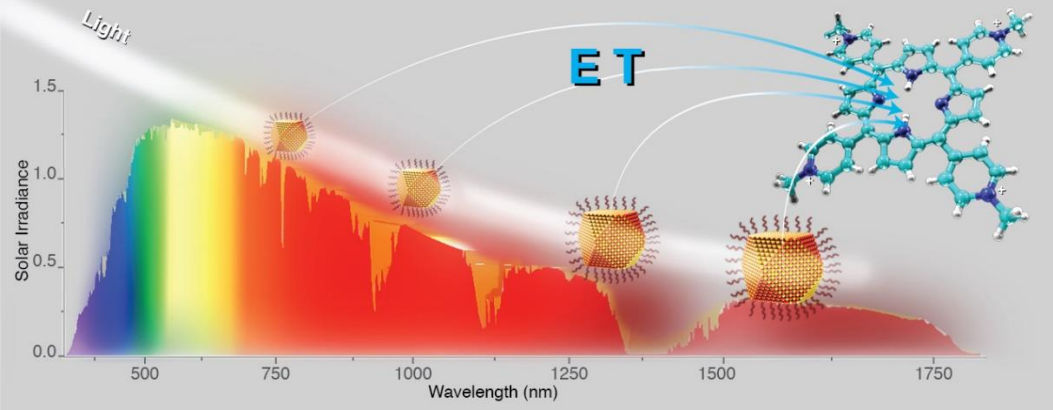

Figure 5.3 Schematic illustrating that the interfacial electrostatic interaction between the positively-charged porphyrin and the negatively-charged QDs surface enables widening the effective bandgap range for charge transfer from PbS QDs, to cover most of the infrared spectral region.[160]

Yet, in order to utilize the broad range of QD sizes in multi-junction PVs, further challenges need to be addressed in the future. In particular, the stability and photoluminescence quantum efficiency of large QDs (d_{QD} > 4 nm) have to be improved, in order to become comparable to smaller PbS QDs.[52,53,173] In fact, it has been reported that the highly-faceted large PbS QDs are more prone to surface oxidation which is evident by significant blue shifts in their excitonic peak, if stored in ambient conditions.[53] Accordingly, these large PbS QDs require a highly durable passivation technique to grant them improvements in stability and photoluminescence quantum efficiency. Over-coating the PbS QDs with a shell of another material to form core/shell

structures[174] may provide a path towards robustly-passivated QD films. The choice of the shelling material should take into account two main parameters; namely, the band offset alignment and the lattice mismatch between the core and shell.[100,174] The inorganic shell would then enable a long-lasting isolation of the core atoms from the surrounding environment, thus offering an improved long-term stability.[174] Moreover, the shell would passivate the surface traps within the core QDs, which decreases recombination centers and contributes to higher photoluminescence quantum efficiencies.[100]

Upon enhancing the stability of a wide range of PbS QD sizes that absorb within the infrared region, broadband multi-junction PVs that harvest the visible and infrared light could be engineered by incorporating active layers of visible-absorbing materials. For instance, employing tunable metal-halide perovskites (*e.g.* $CH_3NH_3PbX_3$, where X= I, Br, or Cl) could be an attractive approach since they share some of the benefits of QDs, like solution-processability, while exhibiting an excellent light-harvesting ability of the visible range of the solar spectrum.[175,176] Continued progress in the fundamental charge transfer investigations will be beneficial for ultimate device optimization. As these various opportunities and challenges are addressed, solution-processed QD-based photovoltaics are expected to proceed in achieving higher performance at lower cost, which is essential for the wide spread deployment of the solar-harvesting technology.

BIBLIOGRAPHY

(1) Lewis, N. S.; Nocera, D. G. *Proc. Natl. Acad. Sci. U. S. A.* **2006**, *103*, 15729.
(2) Eisenberg, R.; Nocera, D. G. *Inorg. Chem.* **2005**, *44*, 6799.
(3) Vennestrom, P. N. R.; Osmundsen, C. M.; Christensen, C. H.; Taarning, E. *Angew. Chem., Int. Ed.* **2011**, *50*, 10502.
(4) Schiermeier, Q.; Tollefson, J.; Scully, T.; Witze, A.; Morton, O. *Nature* **2008**, *454*, 816.
(5) Lewis, N. S. *Science* **2007**, *315*, 798.
(6) Graetzel, M.; Janssen, R. A. J.; Mitzi, D. B.; Sargent, E. H. *Nature* **2012**, *488*, 304.
(7) *Technology Roadmap: Solar Photovoltaic Energy*, International Energy Agency (IEA), 2014.
(8) Hillhouse, H. W.; Beard, M. C. *Curr. Opin. Colloid Interface Sci.* **2009**, *14*, 245.
(9) *Best Research-Cell Effeciencies*, National Renewable Energy Laboratory (NREL), 2015.
(10) Mazzio, K. A.; Luscombe, C. K. *Chem. Soc. Rev.* **2015**, *44*, 78.
(11) Debnath, R.; Bakr, O.; Sargent, E. H. *Energy Environ. Sci.* **2011**, *4*, 4870.
(12) Sargent, E. H. *Nat. Photonics* **2009**, *3*, 325.
(13) Singh, M.; Haverinen, H. M.; Dhagat, P.; Jabbour, G. E. *Adv. Mater.* **2010**, *22*, 673.
(14) Chen, L.-M.; Hong, Z.; Kwan, W. L.; Lu, C.-H.; Lai, Y.-F.; Lei, B.; Liu, C.-P.; Yang, Y. *ACS Nano* **2010**, *4*, 4744.
(15) Talapin, D. V.; Lee, J.-S.; Kovalenko, M. V.; Shevchenko, E. V. *Chem. Rev.* **2010**, *110*, 389.
(16) Luther, J. M.; Gao, J.; Lloyd, M. T.; Semonin, O. E.; Beard, M. C.; Nozik, A. J. *Adv. Mater.* **2010**, *22*, 3704.
(17) Yin, Y.; Alivisatos, A. P. *Nature* **2005**, *437*, 664.
(18) Brus, L. E. *J. Chem. Phys.* **1983**, *79*, 5566.
(19) Reed, M. A.; Randall, J. N.; Aggarwal, R. J.; Matyi, R. J.; Moore, T. M.; Wetsel, A. E. *Phys. Rev. Lett.* **1988**, *60*, 535.
(20) Klimov, V. I. *Annu. Rev. Phys. Chem.* **2007**, *58*, 635.
(21) Wang, Y.; Herron, N. *J. Phys. Chem.* **1991**, *95*, 525.
(22) Liz-Marzan, L. M.; Kamat, P. V. *Nanoscale Materials*; Kluwer Academic Publishers Dordrecht, 2003.
(23) Semonin, O. E.; Luther, J. M.; Beard, M. C. *Mater. Today* **2012**, *15*, 508.
(24) Brus, L. *J. Phys. Chem.* **1986**, *90*, 2555.
(25) Bawendi, M. C.; Steigerwald, M. L.; Brus, L. E. *Annu. Rev. Phys. Chem.* **1990**, *41*, 477.
(26) Murray, C. B.; Norris, D. J.; Bawendi, M. G. *J. Am. Chem. Soc.* **1993**, *115*, 8706.
(27) Murray, C. B.; Kagan, C. R.; Bawendi, M. G. *Annu. Rev. Mater. Sci.* **2000**, *30*, 545.
(28) La Mer, V. K.; Dinegar, R. H. *J. Am. Chem. Soc.* **1950**, *72*, 4847.
(29) Reiss, H. *J. Chem. Phys.* **1951**, *19*, 482.
(30) Peng, X.; Wickham, J.; Alivisatos, A. P. *J. Am. Chem. Soc.* **1998**, *120*, 5343.
(31) Talapin, D. V.; Rogach, A. L.; Haase, M.; Weller, H. *J. Phys. Chem. B* **2001**, *105*, 12278.
(32) Ostwald, W. *Zeit. physikal. Chem.* **1897**, *22*, 289.
(33) Liu, H.; Owen, J. S.; Alivisatos, A. P. *J. Am. Chem. Soc.* **2007**, *129*, 305.
(34) Steckel, J. S.; Yen, B. K. H.; Oertel, D. C.; Bawendi, M. G. *J. Am. Chem. Soc.* **2006**, *128*, 13032.
(35) Shah, A.; Torres, P.; Tscharner, R.; Wyrsch, N.; Keppner, H. *Science (Washington, D. C.)* **1999**, *285*, 692.
(36) Nozik, A. J. *Chem. Phys. Lett.* **2008**, *457*, 3.

(37) Tang, J.; Sargent, E. H. *Adv. Mater.* **2011**, *23*, 12.
(38) Shockley, W.; Queisser, H. J. *J. Appl. Phys.* **1961**, *32*, 510.
(39) Wrobel, D.; Graja, A. *Coord. Chem. Rev.* **2011**, *255*, 2555.
(40) Selinsky, R. S.; Ding, Q.; Faber, M. S.; Wright, J. C.; Jin, S. *Chem. Soc. Rev.* **2013**, *42*, 2963.
(41) American Society for Testing and Materials (ASTM) International: 2006.
(42) American Society for Testing and Materials (ASTM) International: 2012.
(43) Sargent, E. H. *Adv. Mater.* **2008**, *20*, 3958.
(44) Marti, A.; Araujo, G. L. *Sol. Energy Mater. Sol. Cells* **1996**, *43*, 203.
(45) Henry, C. H. *J. Appl. Phys.* **1980**, *51*, 4494.
(46) Wise, F. W. *Acc. Chem. Res.* **2000**, *33*, 773.
(47) McDonald, S. A.; Konstantatos, G.; Zhang, S. G.; Cyr, P. W.; Klem, E. J. D.; Levina, L.; Sargent, E. H. *Nature Materials* **2005**, *4*, 138.
(48) Warner, J. H.; Thomsen, E.; Watt, A. R.; Heckenberg, N. R.; Rubinsztein-Dunlop, H. *Nanotechnology* **2005**, *16*, 175.
(49) Hines, M. A.; Scholes, G. D. *Adv. Mater.* **2003**, *15*, 1844.
(50) Zhang, J.; Gao, J.; Miller, E. M.; Luther, J. M.; Beard, M. C. *ACS Nano* **2014**, *8*, 614.
(51) Knowles, K. E.; Malicki, M.; Weiss, E. A. *J. Am. Chem. Soc.* **2012**, *134*, 12470.
(52) Pichaandi, J.; van Veggel, F. C. J. M. *Coord. Chem. Rev.* **2014**, *263-264*, 138.
(53) Tang, J.; Brzozowski, L.; Barkhouse, D. A. R.; Wang, X.; Debnath, R.; Wolowiec, R.; Palmiano, E.; Levina, L.; Pattantyus-Abraham, A. G.; Jamakosmanovic, D.; Sargent, E. H. *ACS Nano* **2010**, *4*, 869.
(54) Wadia, C.; Alivisatos, A. P.; Kammen, D. M. *Environ. Sci. Technol.* **2009**, *43*, 2072.
(55) Brown, P. R.; Kim, D.; Lunt, R. R.; Zhao, N.; Bawendi, M. G.; Grossman, J. C.; Bulovic, V. *ACS Nano* **2014**, *8*, 5863.
(56) Ip, A. H.; Thon, S. M.; Hoogland, S.; Voznyy, O.; Zhitomirsky, D.; Debnath, R.; Levina, L.; Rollny, L. R.; Carey, G. H.; Fischer, A.; Kemp, K. W.; Kramer, I. J.; Ning, Z.; Labelle, A. J.; Chou, K. W.; Amassian, A.; Sargent, E. H. *Nat. Nanotechnol.* **2012**, *7*, 577.
(57) Chuang, C.-H. M.; Brown, P. R.; Bulovic, V.; Bawendi, M. G. *Nat. Mater.* **2014**, *13*, 796.
(58) Lan, X.; Voznyy, O.; Kiani, A.; Garcia, d. A. F. P.; Abbas, A. S.; Kim, G.-H.; Liu, M.; Yang, Z.; Walters, G.; Xu, J.; Yuan, M.; Fan, F.; Kanjanaboos, P.; Kramer, I.; Zhitomirsky, D.; Lee, P.; Perelgut, A.; Hoogland, S.; Sargent, E. H. *Adv Mater* **2016**, *28*, 299.
(59) Katsiev, K.; Ip, A. H.; Fischer, A.; Tanabe, I.; Zhang, X.; Kirmani, A. R.; Voznyy, O.; Rollny, L. R.; Chou, K. W.; Thon, S. M.; Carey, G. H.; Cui, X.; Amassian, A.; Dowben, P.; Sargent, E. H.; Bakr, O. M. *Adv. Mater.* **2014**, *26*, 937.
(60) Ning, Z.; Voznyy, O.; Pan, J.; Hoogland, S.; Adinolfi, V.; Xu, J.; Li, M.; Kirmani, A. R.; Sun, J.-P.; Minor, J.; Kemp, K. W.; Dong, H.; Rollny, L.; Labelle, A.; Carey, G.; Sutherland, B.; Hill, I.; Amassian, A.; Liu, H.; Tang, J.; Bakr, O. M.; Sargent, E. H. *Nat. Mater.* **2014**, *13*, 822.
(61) Kim, G.-H.; Garcia de Arquer, F. P.; Yoon, Y. J.; Lan, X.; Liu, M.; Voznyy, O.; Jagadamma, L. K.; Abbas, A. S.; Yang, Z.; Fan, F.; Ip, A. H.; Kanjanaboos, P.; Hoogland, S.; Kim, J. Y.; Sargent, E. H. *Nano Lett.* **2015**, *15*, 7691.
(62) Tisdale, W. A.; Williams, K. J.; Timp, B. A.; Norris, D. J.; Aydil, E. S.; Zhu, X. Y. *Science* **2010**, *328*, 1543.
(63) Miaja-Avila, L.; Tritsch, J. R.; Wolcott, A.; Chan, W. L.; Nelson, C. A.; Zhu, X. Y. *Nano Lett.* **2012**, *12*, 1588.
(64) Sambur, J. B.; Novet, T.; Parkinson, B. A. *Science* **2010**, *330*, 63.
(65) Nair, G.; Geyer, S. M.; Chang, L.-Y.; Bawendi, M. G. *Phys. Rev. B* **2008**, *78*, 125325/1.
(66) Schaller, R. D.; Sykora, M.; Pietryga, J. M.; Klimov, V. I. *Nano Lett.* **2006**, *6*, 424.

(67) Semonin, O. E.; Luther, J. M.; Choi, S.; Chen, H.-Y.; Gao, J.; Nozik, A. J.; Beard, M. C. *Science* **2011**, *334*, 1530.
(68) Ross, R. T.; Nozik, A. J. *J. Appl. Phys.* **1982**, *53*, 3813.
(69) Nozik, A. J. *Annu. Rev. Phys. Chem.* **2001**, *52*, 193.
(70) Nozik, A. J.; Beard, M. C.; Luther, J. M.; Law, M.; Ellingson, R. J.; Johnson, J. C. *Chem. Rev.* **2010**, *110*, 6873.
(71) Hanna, M. C.; Nozik, A. J. *J. Appl. Phys.* **2006**, *100*, 074510/1.
(72) Cademartiri, L.; Bertolotti, J.; Sapienza, R.; Wiersma, D. S.; Von Freymann, G.; Ozin, G. A. *J. Phys. Chem. B* **2006**, *110*, 671.
(73) Moreels, I.; Justo, Y.; De Geyter, B.; Haustraete, K.; Martins, J. C.; Hens, Z. *ACS Nano* **2011**, *5*, 2004.
(74) Phillips, T. W.; Lignos, I. G.; Maceiczyk, R. M.; deMello, A. J.; deMello, J. C. *Lab Chip* **2014**, *14*, 3172.
(75) Labelle, A. J.; Thon, S. M.; Masala, S.; Adachi, M. M.; Dong, H.; Farahani, M.; Ip, A. H.; Fratalocchi, A.; Sargent, E. H. *Nano Lett.* **2015**, *15*, 1101.
(76) Yang, Y.; Rodriguez-Cordoba, W.; Xiang, X.; Lian, T. *Nano Lett.* **2012**, *12*, 303.
(77) Hyun, B.-R.; Zhong, Y.-W.; Bartnik, A. C.; Sun, L.; Abruna, H. D.; Wise, F. W.; Goodreau, J. D.; Matthews, J. R.; Leslie, T. M.; Borrelli, N. F. *ACS Nano* **2008**, *2*, 2206.
(78) Cheng, P. Y.; Zhong, D.; Zewail, A. H. *J. Chem. Phys.* **1996**, *105*, 6216.
(79) Sun, J.; Yu, W.; Usman, A.; Isimjan, T. T.; Dgobbo, S.; Alarousu, E.; Takanabe, K.; Mohammed, O. F. *J. Phys. Chem. Lett.* **2014**, *5*, 659.
(80) www.samsung.com. [Online Early Access]. Published Online: 2015.
(81) Yen, B. K. H.; Gunther, A.; Schmidt, M. A.; Jensen, K. F.; Bawendi, M. G. *Angew. Chem., Int. Ed.* **2005**, *44*, 5447.
(82) Yen, B. K. H.; Stott, N. E.; Jensen, K. F.; Bawendi, M. G. *Adv. Mater.* **2003**, *15*, 1858.
(83) Yang, H.; Luan, W.; Tu, S.-t.; Wang, Z. M. *Lab Chip* **2008**, *8*, 451.
(84) Hartman, R. L.; McMullen, J. P.; Jensen, K. F. *Angew. Chem., Int. Ed.* **2011**, *50*, 7502.
(85) Malet-Sanz, L.; Susanne, F. *J. Med. Chem.* **2012**, *55*, 4062.
(86) Edel, J. B.; Fortt, R.; de, M. J. C.; de, M. A. J. *Chem. Commun.* **2002**, 1136.
(87) Nightingale, A. M.; de Mello, J. C. *Adv. Mater. (Weinheim, Ger.)* **2013**, *25*, 1813.
(88) Abdelhady, A. L.; Afzaal, M.; Malik, M. A.; O'Brien, P. *J. Mater. Chem.* **2011**, *21*, 18768.
(89) Nightingale, A. M.; de, M. J. C. *J. Mater. Chem.* **2010**, *20*, 8454.
(90) Yang, H.; Fan, N.; Luan, W.; Tu, S.-t. *Nanoscale Res. Lett.* **2009**, *4*, 344.
(91) Mirhosseini Moghaddam, M.; Baghbanzadeh, M.; Sadeghpour, A.; Glatter, O.; Kappe, C. O. *Chem. - Eur. J.* **2013**, *19*, 11629.
(92) Chan, E. M.; Alivisatos, A. P.; Mathies, R. A. *J. Am. Chem. Soc.* **2005**, *127*, 13854.
(93) Marre, S.; Jensen, K. F. *Chem. Soc. Rev.* **2010**, *39*, 1183.
(94) Nightingale, A. M.; Demello, J. C. *Adv Mater* **2012**.
(95) Shestopalov, I.; Tice, J. D.; Ismagilov, R. F. *Lab Chip* **2004**, *4*, 316.
(96) Nightingale, A. M.; Bannock, J. H.; Krishnadasan, S. H.; O'Mahony, F. T. F.; Haque, S. A.; Sloan, J.; Drury, C.; McIntyre, R.; de Mello, J. C. *J. Mater. Chem. A* **2013**, *1*, 4067.
(97) *Fluoroinert FC-70 product information*, 3M Electronic Liquids, 2000.
(98) Pan, J.; El-Ballouli, A. O.; Rollny, L.; Voznyy, O.; Burlakov, V. M.; Goriely, A.; Sargent, E. H.; Bakr, O. M. *ACS Nano* **2013**, *7*, 10158.
(99) Kramer, I. J.; Minor, J. C.; Moreno-Bautista, G.; Rollny, L.; Kanjanaboos, P.; Kopilovic, D.; Thon, S. M.; Carey, G. H.; Chou, K. W.; Zhitomirsky, D.; Amassian, A.; Sargent, E. H. *Adv. Mater. (Weinheim, Ger.)* **2015**, *27*, 116.

(100) Kim, J. Y.; Voznyy, O.; Zhitomirsky, D.; Sargent, E. H. *Adv. Mater. (Weinheim, Ger.)* **2013**, *25*, 4986.
(101) Zhitomirsky, D.; Voznyy, O.; Levina, L.; Hoogland, S.; Kemp, K. W.; Ip, A. H.; Thon, S. M.; Sargent, E. H. *Nat. Commun.* **2014**, *5*, 3803.
(102) Zhao, N.; Osedach, T. P.; Chang, L.-Y.; Geyer, S. M.; Wanger, D.; Binda, M. T.; Arango, A. C.; Bawendi, M. G.; Bulovic, V. *ACS Nano* **2010**, *4*, 3743.
(103) Berera, R.; Grondelle, R.; Kennis, J. T. M. *Photosynth. Res.* **2009**, *101*, 105.
(104) Kambhampati, P. *J. Phys. Chem. C* **2011**, *115*, 22089.
(105) Hyun, B.-R.; Bartnik, A. C.; Sun, L.; Hanrath, T.; Wise, F. W. *Nano Lett.* **2011**, *11*, 2126.
(106) Plass, R.; Pelet, S.; Krueger, J.; Graetzel, M.; Bach, U. *J. Phys. Chem. B* **2002**, *106*, 7578.
(107) Tvrdy, K.; Frantsuzov, P. A.; Kamat, P. V. *Proc. Natl. Acad. Sci. U. S. A.* **2011**, *108*, 29.
(108) Kamat, P. V. *Acc. Chem. Res.* **2012**, *45*, 1906.
(109) Robel, I.; Kuno, M.; Kamat, P. V. *J. Am. Chem. Soc.* **2007**, *129*, 4136.
(110) Leventis, H. C.; O'Mahony, F.; Akhtar, J.; Afzaal, M.; O'Brien, P.; Haque, S. A. *J. Am. Chem. Soc.* **2010**, *132*, 2743.
(111) Harbold, J. M.; Du, H.; Krauss, T. D.; Cho, K.-S.; Murray, C. B.; Wise, F. W. *Phys. Rev. B: Condens. Matter Mater. Phys.* **2005**, *72*, 195312/1.
(112) Yuan, C.-T.; Wang, Y.-G.; Huang, K.-Y.; Chen, T.-Y.; Yu, P.; Tang, J.; Sitt, A.; Banin, U.; Millo, O. *ACS Nano* **2012**, *6*, 176.
(113) Knowles, K. E.; Tagliazucchi, M.; Malicki, M.; Swenson, N. K.; Weiss, E. A. *J. Phys. Chem. C* **2013**, *117*, 15849.
(114) Knowles, K. E.; Malicki, M.; Parameswaran, R.; Cass, L. C.; Weiss, E. A. *J. Am. Chem. Soc.* **2013**, *135*, 7264.
(115) Yang, Y.; Rodriguez-Cordoba, W.; Lian, T. *J. Am. Chem. Soc.* **2011**, *133*, 9246.
(116) Szendrei, K.; Cordella, F.; Kovalenko, M. V.; Boeberl, M.; Hesser, G.; Yarema, M.; Jarzab, D.; Mikhnenko, O. V.; Gocalinska, A.; Saba, M.; Quochi, F.; Mura, A.; Bongiovanni, G.; Blom, P. W. M.; Heiss, W.; Loi, M. A. *Adv. Mater.* **2009**, *21*, 683.
(117) Jarzab, D.; Szendrei, K.; Yarema, M.; Pichler, S.; Heiss, W.; Loi, M. A. *Adv. Funct. Mater.* **2011**, *21*, 1988.
(118) Wang, D.; Baral, J. K.; Zhao, H.; Gonfa, B. A.; Truong, V.-V.; El Khakani, M. A.; Izquierdo, R.; Ma, D. *Adv. Funct. Mater.* **2011**, *21*, 4010.
(119) Guo, C. X.; Yang, H. B.; Sheng, Z. M.; Lu, Z. S.; Song, Q. L.; Li, C. M. *Angew. Chem., Int. Ed.* **2010**, *49*, 3014.
(120) Gocalinska, A.; Saba, M.; Quochi, F.; Marceddu, M.; Szendrei, K.; Gao, J.; Loi, M. A.; Yarema, M.; Seyrkammer, R.; Heiss, W.; Mura, A.; Bongiovanni, G. *J. Phys. Chem. Lett.* **2010**, *1*, 1149.
(121) Adams, D. M.; Brus, L.; Chidsey, C. E. D.; Creager, S.; Creutz, C.; Kagan, C. R.; Kamat, P. V.; Lieberman, M.; Lindsay, S.; Marcus, R. A.; Metzger, R. M.; Michel-Beyerle, M. E.; Miller, J. R.; Newton, M. D.; Rolison, D. R.; Sankey, O.; Schanze, K. S.; Yardley, J.; Zhu, X. *J. Phys. Chem. B* **2003**, *107*, 6668.
(122) Duvanel, G.; Banerji, N.; Vauthey, E. *J. Phys. Chem. A* **2007**, *111*, 5361.
(123) Herrmann, D.; Niesar, S.; Scharsich, C.; Koehler, A.; Stutzmann, M.; Riedle, E. *J. Am. Chem. Soc.* **2011**, *133*, 18220.
(124) Akaike, K.; Kanai, K.; Yoshida, H.; Tsutsumi, J. y.; Nishi, T.; Sato, N.; Ouchi, Y.; Seki, K. *J. Appl. Phys.* **2008**, *104*, 023710/1.
(125) Moreels, I.; Lambert, K.; Smeets, D.; De Muynck, D.; Nollet, T.; Martins, J. C.; Vanhaecke, F.; Vantomme, A.; Delerue, C.; Allan, G.; Hens, Z. *ACS Nano* **2009**, *3*, 3023.

(126) El-Ballouli, A. O.; Alarousu, E.; Bernardi, M.; Aly, S. M.; Lagrow, A. P.; Bakr, O. M.; Mohammed, O. F. *J. Am. Chem. Soc.* **2014**, *136*, 6952.
(127) Litvin, A. P.; Parfenov, P. S.; Ushakova, E. V.; Fedorov, A. V.; Artemyev, M. V.; Prudnikau, A. V.; Cherevkov, S. A.; Rukhlenko, I. D.; Baranov, A. V. *Proc. SPIE* **2012**, *8564*, 85641Z/1.
(128) Hardman, S. J. O.; Graham, D. M.; Stubbs, S. K.; Spencer, B. F.; Seddon, E. A.; Fung, H.-T.; Gardonio, S.; Sirotti, F.; Silly, M. G.; Akhtar, J.; O'Brien, P.; Binks, D. J.; Flavell, W. R. *Phys. Chem. Chem. Phys.* **2011**, *13*, 20275.
(129) Beard, M. C.; Knutsen, K. P.; Yu, P.; Luther, J. M.; Song, Q.; Metzger, W. K.; Ellingson, R. J.; Nozik, A. J. *Nano Letters* **2007**, *7*, 2506.
(130) Kamat, P. V. *J. Phys. Chem. C* **2008**, *112*, 18737.
(131) Ginger, D. S.; Greenham, N. C. *Phys. Rev. B: Condens. Matter Mater. Phys.* **1999**, *59*, 10622.
(132) Boulesbaa, A.; Issac, A.; Stockwell, D.; Huang, Z.; Huang, J.; Guo, J.; Lian, T. *J. Am. Chem. Soc.* **2007**, *129*, 15132.
(133) Wang, D.; Zhao, H.; Wu, N.; El Khakani, M. A.; Ma, D. *J. Phys. Chem. Lett.* **2010**, *1*, 1030.
(134) Scharber, M. C.; Muehlbacher, D.; Koppe, M.; Denk, P.; Waldauf, C.; Heeger, A. J.; Brabec, C. J. *Adv. Mater. (Weinheim, Ger.)* **2006**, *18*, 789.
(135) Altavilla, C.; Ciliberto, E. *Inorganic Nanoparticles: Synthesis, Applications, and Perspectives* Taylor and Francis Group: Boca Raton, Florida, 2011.
(136) Bernardi, M.; Lohrman, J.; Kumar, P. V.; Kirkeminde, A.; Ferralis, N.; Grossman, J. C.; Ren, S. *ACS Nano* **2012**, *6*, 8896.
(137) Lakowicz, J. R. *Principles of Fluorescence Spectroscopy* 3rd ed.; Springer: New York, 2006.
(138) Pesce, A. J., Rosen, C. G., Pasby T. *Fluorescence Spectroscopy: An Introduction for Biology and Medicine*; Marcel Dekker: New York, 1971.
(139) Dibbell, R. S.; Watson, D. F. *J. Phys. Chem. C* **2009**, *113*, 3139.
(140) Cyr, P. W.; Tzolov, M.; Hines, M. A.; Manners, I.; Sargent, E. H.; Scholes, G. D. *J. Mater. Chem.* **2003**, *13*, 2213.
(141) Morris-Cohen, A. J.; Frederick, M. T.; Cass, L. C.; Weiss, E. A. *J. Am. Chem. Soc.* **2011**, *133*, 10146.
(142) Fitzmorris, B. C.; Pu, Y.-C.; Cooper, J. K.; Lin, Y.-F.; Hsu, Y.-J.; Li, Y.; Zhang, J. Z. *ACS Appl. Mater. Interfaces* **2013**, *5*, 2893.
(143) Guldi, D. M.; Prato, M. *Acc. Chem. Res.* **2000**, *33*, 695.
(144) Liedtke, M.; Sperlich, A.; Kraus, H.; Deibel, C.; Dyakonov, V.; Filippone, S.; Delgado, J. L.; Martin, N.; Poluektov, O. G. *ECS Trans.* **2010**, *28*, 3.
(145) Mohammed, O. F.; Adamczyk, K.; Banerji, N.; Dreyer, J.; Lang, B.; Nibbering, E. T. J.; Vauthey, E. *Angew Chem Int Ed Engl* **2008**, *47*, 9044.
(146) Mohammed, O. F.; Vauthey, E. *J. Phys. Chem. A* **2008**, *112*, 5804.
(147) Sargent, E. H. *Nat. Photonics* **2012**, *6*, 133.
(148) Kramer, I. J.; Sargent, E. H. *ACS Nano* **2011**, *5*, 8506.
(149) Wang, X.; Koleilat, G. I.; Tang, J.; Liu, H.; Kramer, I. J.; Debnath, R.; Brzozowski, L.; Barkhouse, D. A. R.; Levina, L.; Hoogland, S.; Sargent, E. H. *Nat. Photonics* **2011**, *5*, 480.
(150) Choi, J. J.; Wenger, W. N.; Hoffman, R. S.; Lim, Y.-F.; Luria, J.; Jasieniak, J.; Marohn, J. A.; Hanrath, T. *Adv. Mater.* **2011**, *23*, 3144.
(151) Guchhait, A.; Rath, A. K.; Pal, A. J. *Sol. Energy Mater. Sol. Cells* **2011**, *95*, 651.
(152) Tao, L.; Xiong, Y.; Liu, H.; Shen, W. *Nanoscale* **2014**, *6*, 931.
(153) Barbara, P. F.; Meyer, T. J.; Ratner, M. A. *J. Phys. Chem.* **1996**, *100*, 13148.

(154) Hagfeldt, A.; Boschloo, G.; Sun, L.; Kloo, L.; Pettersson, H. *Chem. Rev.* **2010**, *110*, 6595.
(155) Martinez-Diaz, M. V.; de la Torre, G.; Torres, T. *Chem. Commun. (Cambridge, U. K.)* **2010**, *46*, 7090.
(156) Li, Z.; Wang, C. M.; Persaud, L.; Mallouk, T. E. *J. Phys. Chem.* **1988**, *92*, 2592.
(157) Rawson, J.; Stuart, A. C.; You, W.; Therien, M. J. *J. Am. Chem. Soc.* **2014**, *136*, 17561.
(158) Fischer, A.; Rollny, L.; Pan, J.; Carey, G. H.; Thon, S. M.; Hoogland, S.; Voznyy, O.; Zhitomirsky, D.; Kim, J. Y.; Bakr, O. M.; Sargent, E. H. *Adv. Mater.* **2013**, *25*, 5742.
(159) Tang, J.; Kemp, K. W.; Hoogland, S.; Jeong, K. S.; Liu, H.; Levina, L.; Furukawa, M.; Wang, X.; Debnath, R.; Cha, D.; Chou, K. W.; Fischer, A.; Amassian, A.; Asbury, J. B.; Sargent, E. H. *Nat. Mater.* **2011**, *10*, 765.
(160) El-Ballouli, A. a. O.; Alarousu, E.; Kirmani, A. R.; Amassian, A.; Bakr, O. M.; Mohammed, O. F. *Adv. Funct. Mater.* **2015**, *25*, 7435.
(161) Doane, T. L.; Chuang, C.-H.; Hill, R. J.; Burda, C. *Acc. Chem. Res.* **2012**, *45*, 317.
(162) Feng, W.; Qin, C.; Shen, Y.; Li, Y.; Luo, W.; An, H.; Feng, Y. *Sci. Rep.* **2014**, *4*, 3777/1.
(163) Idowu, M.; Lamprecht, E.; Nyokong, T. *J. Photochem. Photobiol., A* **2008**, *198*, 7.
(164) El-Ballouli, A. O.; Alarousu, E.; Usman, A.; Pan, J.; Bakr, O. M.; Mohammed, O. F. *ACS Photonics* **2014**, *1*, 285.
(165) Kumar, M.; Neta, P.; Sutter, T. P. G.; Hambright, P. *J. Phys. Chem.* **1992**, *96*, 9571.
(166) Neta, P. *J. Phys. Chem.* **1981**, *85*, 3678.
(167) Mandal, S.; Rahaman, M.; Sadhu, S.; Nayak, S. K.; Patra, A. *J. Phys. Chem. C* **2013**, *117*, 3069.
(168) Ahmed, G. H.; Aly, S. M.; Usman, A.; Eita, M. S.; Melnikov, V. A.; Mohammed, O. F. *Chem. Commun.* **2015**, *51*, 8010.
(169) Mohammed, O. F.; Adamczyk, K.; Banerji, N.; Dreyer, J.; Lang, B.; Nibbering, E. T. J.; Vauthey, E. *Angew. Chem., Int. Ed.* **2008**, *47*, 9044.
(170) Zhu, K.; Hu, X.; Ge, Q.; Sun, Q. *Anal. Chim. Acta* **2014**, *812*, 199.
(171) Ohmori, Y.; Itoh, E.; Miyairi, K. *Thin Solid Films* **2006**, *499*, 369.
(172) Liao, M.-S.; Scheiner, S. *J. Comput. Chem.* **2002**, *23*, 1391.
(173) Choi, H.; Ko, J.-H.; Kim, Y.-H.; Jeong, S. *J. Am. Chem. Soc.* **2013**, *135*, 5278.
(174) Reiss, P.; Protiere, M.; Li, L. *Small* **2009**, *5*, 154.
(175) Stranks, S. D.; Snaith, H. J. *Nat. Nanotechnol.* **2015**, *10*, 391.
(176) Kojima, A.; Teshima, K.; Shirai, Y.; Miyasaka, T. *J. Am. Chem. Soc.* **2009**, *131*, 6050.
(177) Sardela, M. *Practical Materials Characterization*; Springer: New York, 2014.
(178) Wang, Z. L. *J. Phys. Chem. B* **2000**, *104*, 1153.
(179) Cademartiri, L.; Montanari, E.; Calestani, G.; Migliori, A.; Guagliardi, A.; Ozin, G. A. *J. Am. Chem. Soc.* **2006**, *128*, 10337.
(180) Klimov, V. I. *J. Phys. Chem. B* **2000**, *104*, 6112.
(181) Jhonsi, M. A.; Renganathan, R. *J. Colloid Interface Sci.* **2010**, *344*, 596.
(182) Kim, D. I.; Islam, M. A.; Avila, L.; Herman, I. P. *J. Phys. Chem. B* **2003**, *107*, 6318.

APPENDICES

A. Methods and Experimental Procedures

A.1 Chemicals

The precursors employed to perform experimental synthesis for this dissertation were lead(II) oxide powder (PbO, J. T. Baker, 99%), oleic acid (OA, Alpha Aesar, technical grade 90%), bis(trimethylsilyl) sulfide (TMS, Acros Organics, 95% purity), cadmium(II) chloride ($CdCl_2$, Alpha Aesar, anhydrous 99%), tetradecylphosphonic acid (TDPA, Alfa Aesar, 98%), oleylamine (Sigma-Aldrich, technical grade 70%), and 1-thioglycerol (TG, Sigma-Aldrich, ≥ 97%). The solvents used including 1-octadecene (ODE, technical grade 90%), toluene (anhydrous, 99.8%), octane (anhydrous, ≥ 99%), acetone (ACS reagent, ≥ 99.5%), methanol (HPLC grade, > 99%), acetonitrile (anhydrous, 99.8%), 1,2-diclorobenzene (HPLC grade, 99%), and dimethylsulfoxide (DMSO, anhydrous, 99.9%) were purchased from Sigma-Aldrich. Deuterated DMSO (DMSO-d_6, 99.5% isotopic) and fluoroinert electronic liquid (FC-70) were obtained from Thermo Fisher Scientific. 5,10,15,20-Tetra(4-pyridyl)porphyrin (TPyP) and phenyl-C61-butyric acid methyl ester (PCBM, > 99% purity) were purchased from Sigma-Aldrich, while 5,10,15,20-Tetra(N-methyl-4-pyridyl)porphyrin tetrachloride (TMPyP) was obtained from Frontier Scientific. ODE was degassed by pumping at 100 °C overnight before use, while the other chemicals were used as received without further purification.

A.2 Batch Synthesis of PbS QDs

The QD synthesis was performed in a three-neck round bottom flask with Schlenk line setting using lead oleate and TMS as precursors in ODE, according to Hines and Scholes.[49] Lead oleate was prepared by pumping a mixture of PbO (0.9 g) and OA (3 mL) in ODE (6 mL) for 16 hours at 100 °C. Then, the resulting solution was stirred vigorously under nitrogen for about 30 min, while being heated to certain temperatures ranging between 67 °C -130 °C depending on the required QD size. Inside a glovebox, the sulfur precursor was prepared by mixing TMS with ODE. This mixture was rapidly injected into the reaction flask at the required injection temperature (i.e. 67 °C for smaller QDs and 130 °C for larger QDs). After TMS injection, slow cooling was allowed to facilitate size focusing and help narrowing the size distribution. Once 35 °C was reached, acetone was injected to isolate the oleate-capped PbS QDs by precipitating them from solution. The precipitate was washed twice with toluene/acetone as solvent/antisolvent mixture, followed by redispering in toluene. Then, the washing procedure was repeated twice again with toluene/methanol mixture, and finally dissolved in octane (50 mg/mL).

A.3 Flow Synthesis of PbS QDs

Continuous flow synthesis was performed using a commercially available continuous flow reactor, the FlowSyn Multi-X system (Uniqsis Ltd, Cambridge UK). The lead oleate precursor was prepared by dissolving PbO (0.9 g) and OA (3 mL) in ODE (6 mL) and pumping the solution for 16 hours at 100 °C. Then, 30 mL ODE and 20 mL FC-70 were added to the lead precursor solution. The mixture was transferred to a bottle and

maintained at 60 °C to prevent solidification of the precursor. A stock solution of the sulfur precursor was prepared by mixing TMS (360 µL) with ODE (20 mL) and FC-70 (20 mL) in a glovebox. Both bottles were maintained under continuous vigorous stirring (to maintain a homogenous mixture between the different liquid phases) and nitrogen purging throughout the reaction. The nucleation temperature was varied in the range of 80 -150 °C, while the growth temperature was set between 50 and 100 °C. The employed coil reactor were made of perfluoroalkoxy (PFA) tubings. The length of the nucleation coil was fixed to 100 cm, while the length of the growth coil was 290 cm. The flow rate was varied within the range 1−3 mL/min to control the total residence time within the reactor. After passing through the mixing and thermal stages, the product was collected in vials containing acetone to quench the reaction. The QDs were washed several times by precipitation with acetone and redispersion in toluene. Further QDs purification was done by precipitation with methanol and redispersion in octane (50 mg/mL).

A.4 Additional Passivation Steps during Synthesis of PbS QDs

Extra surface passivation with $CdCl_2$ treatment was performed during the batch synthesis of PbS QDs which is described above. After TMS injection at the required temperature, slow cooling was allowed to facilitate size focusing and help narrowing the size distribution. Once 60 °C was reached, $CdCl_2$ treatment ($CdCl_2$-TDPA-Oleylamine) was introduced according to Ip *et al*..[56] Slow cooling was continued until 35 °C is reached whereby acetone was added to precipitate the QDs from solution. After centrifugation,

the OA-capped $CdCl_2$-treated PbS QDs were purified twice by dispersion in toluene and re-precipitation with acetone/methanol (1:1 volume ratio), and finally dissolved in octane (150 mg/mL).

A.5 Solution-Phase Ligand Exchange

The solution-phase ligand exchange was done according to a modified literature method.[158] Shortly, 100 µL of the OA-capped $CdCl_2$-treated QDs (150 mg/mL) were dispersed in 4 mL of octane. The mixture was added to a solution of TG (90 µL, 0.112 g) in DMSO (4 mL). The biphasic system was vortexed vigorously for 30 seconds, resulting in the migration of QDs from non-polar to polar phase. After centrifugation at 5000 rpm for one minute, the polar phase was separated from the clear non-polar phase. The polar QD dispersion was rinsed four more times with an equal volume of octane, followed by vortexing, and centrifugation. Finally, acetonitrile was added in 4:1 volume ratio to induce precipitation and remove excess ligands, followed by centrifugation, and isolation. The TG-capped $CdCl_2$-treated QDs were then dried under vacuum overnight, dispersed in DMSO, and centrifuged at 15000 rpm for five minutes to remove any aggregates.

A.6 Optical Characterization

The steady-state absorption spectra were measured using a Cary 5000 UV-VIS-NIR spectrophotometer (Varian Inc.), while the steady-state photoluminescence spectra were measured using a Jobin-Yvon-Horiba Nanolog spectrofluorometer. Quartz cuvettes

with a path length of 1 cm were used. Photoluminescence quantum efficiency (PLQE) measurements were performed within an integrating sphere setup using a 640 nm diode laser for excitation and an InGaAs array detector (Ocean Optics NIR-512). The measurements were done using 1 mm cuvettes with solutions of low concentration to guarantee low reabsorption by the sample of the emitted photoluminescence signal.

A.7 Photoelectron Spectroscopy

Photoelectron spectroscopy involves determining the energy of photoelectrons which are emitted from a material *via* the photoelectric effect.[177] In this technique, a sample is bombarded with photons which eject electrons out from the sample's atoms. The excited electrons are then collected and their kinetic energy is measured. The difference between the photoelecton's kinetic energy and the incident photon's energy defines the binding energy of the sample's electrons; which provides useful information about the material's chemical composition and electronic structure.[177] Depending on the source of ionization energy, photoelectron spectroscopy is classified into X-ray Photoelectron Spectroscopy (XPS) and Ultraviolet Photoelectron Spectroscopy (UPS).[177] XPS is an analytical technique which utilizes high energy X-rays (1000-1500 eV) as an excitation source, and is thus capable of probing core electrons and identifying chemical compositions.[177] On the other hand, UPS employs ultraviolet rays (<41 eV) which are only sufficient for ejecting electrons from the valence orbitals; thus offering insight into the electronic structure of the material.[177]

In a typical XPS measurement, a survey scan is first performed to identify the energy peaks corresponding to different elements within a sample. A detailed scan is then performed of specific regions to obtain higher-resolution peaks. The XPS measurements were carried out within an ultrahigh vacuum (UHV, pressure < 10^{-9} millibar) chamber equipped with a hemispherical energy analyzer (SPHERA U7). The incident X-ray photons were from a monochromated Al K α X-ray source (1486.6 eV) with a total energy resolution of 0.1 eV. The survey spectrum was acquired at a pass energy of 40 eV, while the high resolution core level peaks for the various elements were obtained at a pass energy of 20 eV. The spectra were referenced to the C1s core level peak with its C-C chemical bond component neutralized at 285.0 eV. The QD dispersions were deposited on tin-doped indium oxide (ITO) coated glass by spin-coating (for dispersions in octane), or by drop-casting (for dispersions in DMSO) followed by mild heating at 35 °C to accelerate the drying process. As for the UPS measurements, Helium I photons (21.2 eV) were used to acquire the spectra at normal emission. The photon line width was ∼250 eV and the minimum spot size was ∼1mm.

A.8 Transmission Electron Microscopy (TEM)

Transmission Electron Microscopy (TEM) is a powerful technique that adopts high-energy electrons to interact with an ultra-thin specimen and provide structural and crystallographic information about the sample.[177,178] The electron beam is produced by an electron gun (e.g. Lanthanum Hexaboride, LaB_6) located at the top of the microscope, and then focused on the sample by condenser lenses.[178] Upon interaction with the

sample, the transmitted beam is directed towards a magnification system which consists of several lenses.[177,178] A phosphor screen is employed to convert the electron images into photo images which are detected by a charge-coupled diode (CCD) camera to obtain digital images that facilitate data processing.[177,178] High-resolution TEM uses directly transmitted beams and diffracted ones to produce an image of the sample that reflects the periodicity of the lattice with high resolution (sub-Å level); which enables studying the atomic-level crystal structure and defects.[177]

High-resolution TEM measurements were carried out on a TitanG2 80-300 instrument operating at 300 kV. The OA-capped PbS QD solutions in octane were deposited onto 300 mesh gold grids with holey carbon film, and dried in air for at least one hour before imaging. The average size of the QDs was calculated by measuring the diameter of ~300 particles with *ImageJ* program. The TG-capped PbS QDs dispersions in DMSO were similarly deposited and dried in air for at least five hour before imaging.

A.9 Device Fabrication and Characterization

The PbS QD film was deposited in a layer-by-layer fashion by spin-casting the PbS QDs in octane (50 mg/mL)- through a 0.2 µm polytetrafluoroethyelene (PTFE) filter- on glass substrates topped with fluorine-doped tin oxide (FTO) and TiO_2 NCs film. Spin-casting was done at 2500 rpm for 10 seconds for each layer, forming a total of 10 layers. Solid-state ligand exchange to 3-mercaptopropionic acid (MPA) was achieved on each layer by dispensing a 1% v/v MPA:methanol solution to cover the entire substrate, then spinning after 3 seconds at 2500 rpm for 5 seconds. Two rinses with methanol were

applied for each layer. A top electrode consisting of MoO_3 (7.5 nm), Au (50 nm), and Ag (120 nm) was deposited inside an angstrom engineering (Åmod) deposition system within a glovebox at deposition rates of 0.2 Å/s, 1.5 Å/s, and 3 Å/s respectively. At the end of the process, the edges of the substrate were scratched to allow electrical contact with the FTO underneath.

The current–voltage (J-V) characteristics were measured in an inert nitrogen environment under 100 mW cm^{-2} simulated AM1.5 illumination (ScienceTech Xenon lamp), using a digital multimeter (Keithley 2400). The active area of the solar cell was illuminated through a circular aperture with an area of 0.049 cm^2. The source intensity was measured using a Melles–Griot broadband power meter (responsive from 300-2000 nm). The test cell was mounted in a thermoelectric holder with temperature feedback to be stabilized at 25.0 ± 0.1 °C during measurements.

A.10 Steady-state Quenching Measurements

The stock OA-capped PbS QDs solutions (in octane) were diluted with 1,2-dichlorobenzene to maintain a constant concentration (~1.5×10^{-6} M), as determined by the optical density (OD) at the first exciton absorption peak (*i.e.* $1S_h \rightarrow 1S_e$ transition) within a 1 cm path length quartz cuvette, where $\varepsilon_{pbs\ QD} = 19600 * r^{2.32}$.[179] Alternatively, the stock solutions were diluted with different concentrations of PCBM in 1,2-dichlorobenzene while maintaining a fixed QDs concentration. The steady-state absorption and PL spectra of these solutions were then measured as described above (Section A.6)

Similarly, the stock TG-capped $CdCl_2$-treated PbS QDs (in DMSO) were diluted with extra DMSO, or alternatively porphyrin (TPyP or TMPyP) in DMSO, while maintaining a constant QD concentration ($\sim 1.5 \times 10^{-6}$ M), as determined by the OD at the first exciton absorption peak within a 1 cm path length quartz cuvette.

A.11 Transmission Absorption (TA) Spectroscopy

The stock PbS QDs (in octane or DMSO) were diluted with the required solvent to maintain a constant concentration ($\sim 1.5 \times 10^{-6}$ M), as determined by the optical density at the first exciton absorption peak within a 2 mm path length cuvette, where $\varepsilon_{pbs\ QD} = 19600 * r^{2.32}$.[179] Alternatively, the stock solutions were diluted with a certain concentration of the quencher (*e.g.* PCBM, TMPyP, TPyP) while maintaining a fixed QD concentration. All TA experiments were done at room temperature, with constant sample stirring to avoid the photocharging of the QDs.[128,129] The experiments were performed at low pump fluence to ensure that the photoexcited QDs are due to single-photon absorption and to prevent contributions from Auger decay pathways.[180] The absorption spectrum of each sample was measured before and after TA experiments to ensure the abscence of any degradation.

Femtosecond and nanosecond TA spectroscopy measurements were done with Ultrafast Systems, HELIOS and EOS setups, respectively. The fundamental laser is provided by a Ti:Sapphire femtosecond regenerative amplifier (Spectra-Physics Spitfire Pro 35F-XP) which produces 35 fs pulses at 800 nm with 4 mJ of energy/pulse, and a repetition rate of 1 kHz. The pump (excitation) beam is tuned by passing 1 mJ of the

fundamental (λ=800 nm) through an optical parametric amplifier (TOPAS-C stage) to tune its wavelength (λ=240-2600 nm), and selectively excite specific electronic transitions within a sample. As for the probe beam, a small portion of the fundamental (≈ 60 μJ) is routed *via* a computer-controlled delay line, adjustable pinholes, focusing lens, and variable neutral density filter to a crystal for white light continuum (WLC) generation. The white probe beam is then directed towards the sample *via* a focusing mirror. The delay between the pump and probe pulses can be varied to allow TA measurements within 5.8 ns (HELIOS) and 400 μs (EOS) time windows. The pump and probe beams are adjusted to overlap spatially and temporally on the sample. Following interaction with the sample, the probe beam is directed towards a near-infrared spectrometer (InGaAs-NIR) covering the range of 800-1600 nm with 3.5 nm resolution at 7900 spectra/s, or a visible spectrometer (CMOS VIS) covering the range of 350-800 nm, with 1.5 nm resolution at 9500 spectra/s. The probe beam is collected by the chosen spectrometer after passing through wave pass filters that attenuate the white light around the Spitfire fundamental at 800 nm. For both Helios and EOS systems, a two-channel probe (probe-reference) method is used. In this method, the probe pulse is passed through a beam-splitter before reaching the sample, in order to split the beam into two-channels (sample and reference). In this way, a portion is sent directly to the sample, while the other is directed to the detector to act as a reference. This technique allows dividing out any fluctuations in the probe beam intensity during the experiment. The TA spectra are usually averaged until the desired signal-to-noise ratio is achieved.

Global analysis fitting procedures are then applied to extract the kinetics of dynamical processes from the TA spectra.

A.12 Dynamic Light Scattering (DLS) and Zeta-potential Measurement

Dynamic light scattering (DLS) is a spectroscopic technique which can be used to characterize the hydrodynamic radia and size distributions of nanoparticles in solution. The technique is based upon irradiating the sample with a monochromatic laser light, and measuring the intensity of the diffracted light by a detector which is placed at a known scattering angle. The intensity of diffracted light is then related to the hydrodynamic size of the particles, to obtain the size distribution. For our measurments, the QD samples in DMSO were diluted to low concentrations, and centrifuged at high speed (13K rpm) to remove any aggregates that could contribute to the light scattering. The measurements were performed using a Zetasizer Nano (Malvern) at 20˚C in a 1 cm path length quartz cuvette, with back-scattering mode.

The Malvern-Zetasizer Nano instrument was also used to measure the Zeta-potential of the QDs, by the front-scattering detection mode. The technique is based upon measuring the mobility of the charged particles that are immersed in a liquid, under the effect of an external electric field.[161] In other words, the method is described as an electrophoretic light scattering technique.[161] Our measurments were done at 20˚C within 1 cm path length electrophoresis cell.

B. Supporting Information

B.1 Donor-Acceptor Spectral Overlaps

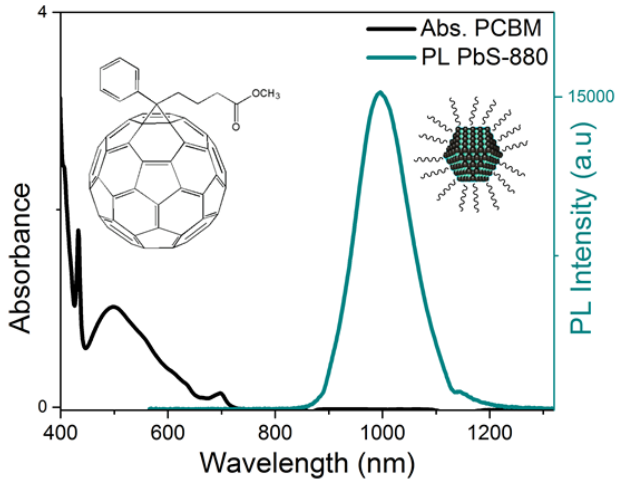

Figure SI.1 Absorbance of PCBM (in 1,2-dichlorobenzene) shows no spectral overlap with the PL spectra of small PbS QDs; which rules out the possibility of energy transfer.

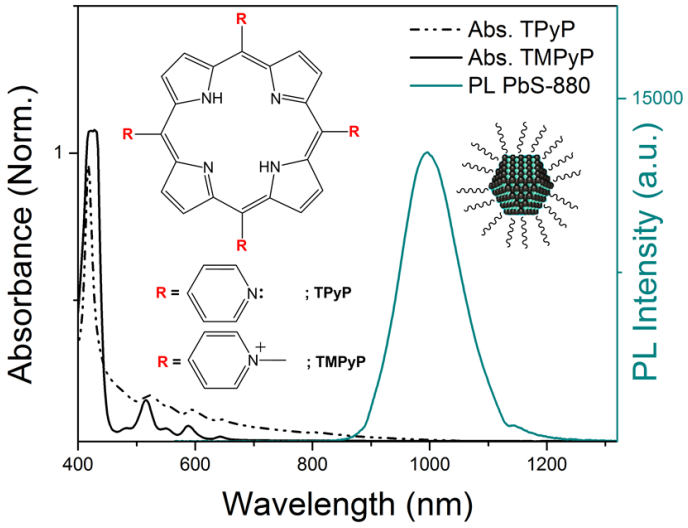

Figure SI.2 Absorbance of TPyP and TMPyP (in DMSO-d_6) shows no spectral overlap with the PL spectra of small PbS QDs; which rules out the possibility of energy transfer.

B.2 Stern-Volmer (SV) Plots

The PL quenching data can be presented as a plot of PL_0/PL versus the quencher concentration *i.e.* [quencher], where PL_0 and PL are the fluorescence intensities in the absence and presence of the quencher.[137] Such plots are named Stern-Volmer (SV) plots, and they enable exploring the kinetics of the deactivation process.[137] A linear SV plot generally indicates the existence of a single class of fluorophores, all being equally accessible to the quencher.[51,137] While if a portion of the fluorophore population is not accessible (or less accessible) to quencher, then the SV plot typically deviates from linearity toward the x-axis (*i.e.* downward curvature).[137] SV plots that reveal an upward curvature (*i.e.* towards the y-axis) typically indicate the occurrence of multiple quenching processes depending on the amount of quencher added.[137] For instance, collisional (dynamic) and static (ground-state complex formation) quenching mechanisms could be involved.[137,139] A modified SV plot (*i.e.* log (PL_0 – PL /PL) versus log [quencher]) determines the binding constants between the fluorophore and the quencher in the case of static quenching.[181]

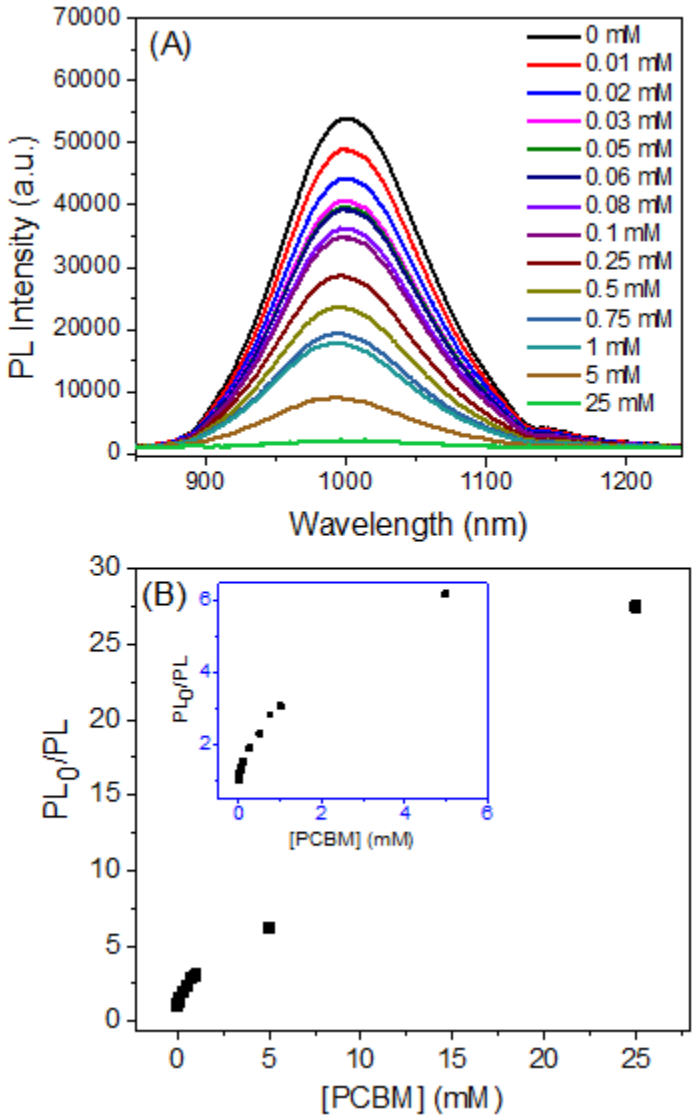

Figure SI.3 A) Photoluminescence spectra of PbS-880 upon the addition of a larger range of PCBM concentrations (0.01-25mM), in 1,2-dichlorobenzene. B) SV plot for PbS-880 and PCBM system revealed a deviation from linearity, towards a downward curvature.[126]

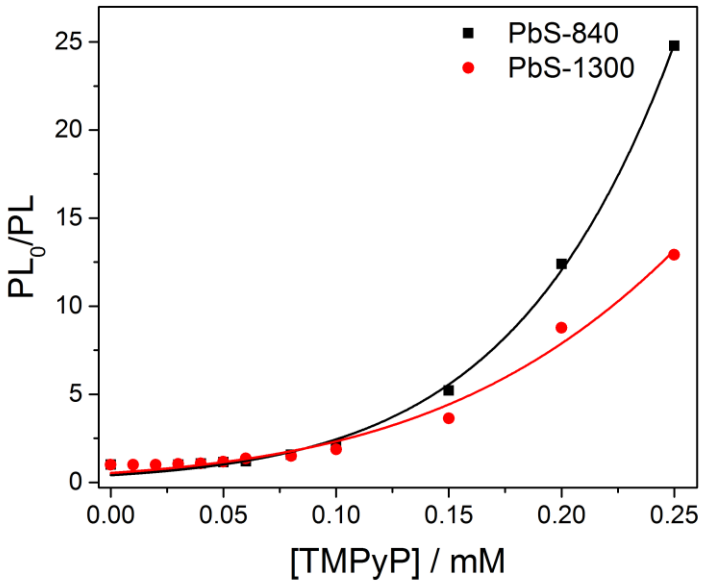

Figure SI.4 SV plots for TMPyP addition to small and large QDs. Both plots reveal an upward curvature indicating the presence of complex quenching processes depending on the [TMPyP]. The plots could be based upon the equation: $PL_0/PL = (1 + K_{sv}\,[TMPyP])\,(1 + K_{Assoc}\,[TMPyP])$; thus presenting a combination of static and dynamic quenching.[160]

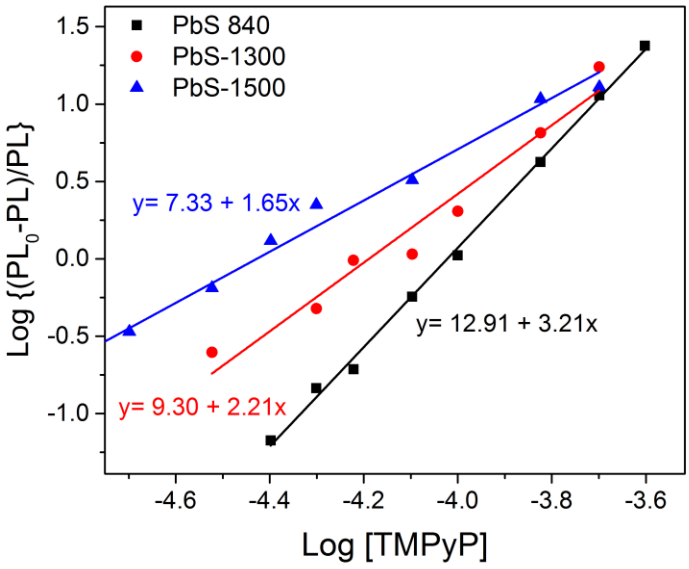

Figure SI.5 Modified Stern-Volmer plot representing the static quenching according to the equation: log {(PL_0-PL)/PL} = Log K_b + n Log [Q], for different QD sizes upon TMPyP addition. The plot reveals a significant decrease in the intercept as the QD size increases, which translates to a reduced binding constant for larger QDs.[160]

Table SI.1 Calculated binding constants between different QD sizes and TMPyP based on the modified SV plots.[160]

PbS size + TMPyP	Intercept = log (K_b)	Slope = n	K_b (M^{-1})
PbS-840	12.91	3.21	$8.13 * 10^{12}$
PbS-1300	9.30	2.21	$2.00 * 10^{9}$
PbS-1500	7.33	1.65	$2.14 * 10^{7}$

B.3 Further QD characterization

This section contains additional supporting information for the characterization of TG-capped $CdCl_2$-treated PbS QDs, which were used in Chapter 4.

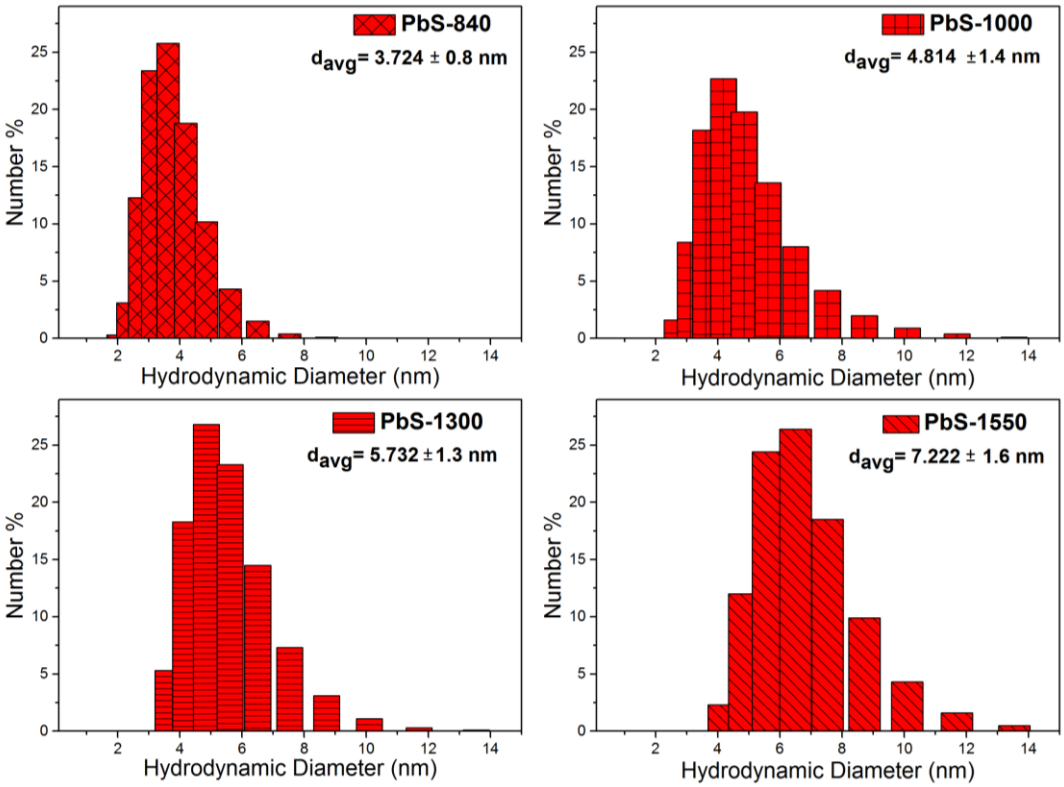

Figure SI.6 Size distributions of the different sizes of TG-capped $CdCl_2$-treated PbS QDs, based on the hydrodynamic diameter obtained by DLS.[160]

Table SI.2 Comparison between the hydrodynamic diameter obtained by DLS, the calculated QD core diameter without the surface ligands, and the theoretical core diameter. The table shows an agreement between the theoretical core diameters obtained by Moreels equation, and the calculated core diameters upon subtracting the ligand size from the hydrodynamic diameter.

QD Sample	Hydrodynamic diameter (HD) from DLS	Calculated core diameter (HD - 2 ligand layers of TG, where TG = 0.76 nm)[182]	Theoretical core diameter based on Moreels *et al*.[125]
PbS-840	3.7 ± 0.8 nm	2.2 ± 0.8 nm	2.6 nm
PbS-1000	4.8 ± 1.4 nm	3.3 ± 1.4 nm	3.3 nm
PbS-1300	5.7 ± 1.3 nm	4.2 ± 1.3 nm	4.6 nm
PbS-1550	7.2 ± 1.6 nm	5.7 ± 1.6 nm	5.9 nm

Table SI.3 Relative atomic ratio of cadmium and chloride ligands within the QDs composition as obtained by XPS.

Elements	Pb	:	Cl	:	Cd
Atomic ratio	1	:	0.189	:	0.037

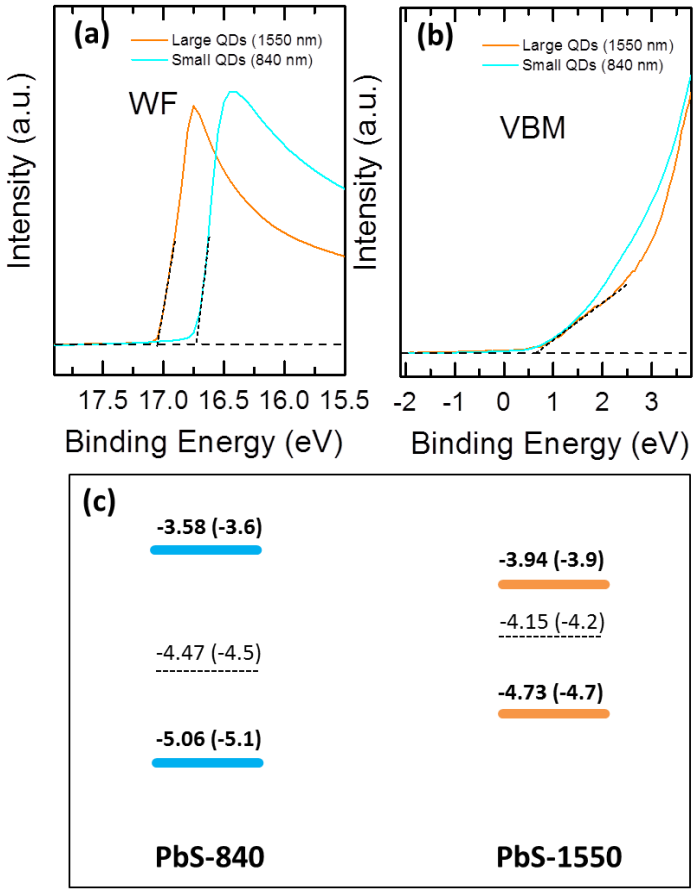

Figure SI.7 (A) Secondary electron cutoff and (B) valence band regions for large (PbS-1550) and small (PbS-840) QDs as obtained by UPS. Electronic band structures for the QDs are shown in (C).[160] The conduction band minima are plotted by adding the optical band gaps, as determined from the first exciton absorption peak. The values shown in brackets are the rounded figures for the energy levels, commensurate with the ~0.1 eV energy resolution of the analyser.

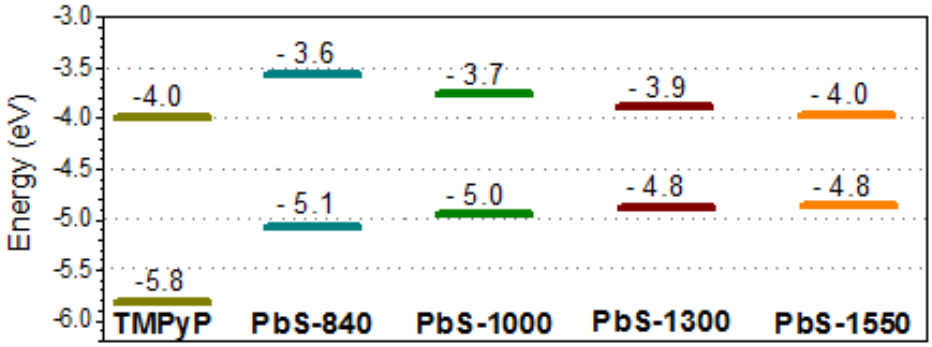

Figure SI.8 A sketch of the energy band alignments of QD donors and TMPyP acceptor employed in this work.[160] The figure clarifies the reduced free energy driving force for the CT as larger QDs are employed. The valence band edges of the different QD sizes were determined by UPS. The conduction band edges were calculated by adding the optical bandgap energy, as determined from the first exciton absorption peak. The TMPyP HOMO and LUMO were obtained from literature.[170] The binding energy values were rounded to the nearest 100 meV value in accordance with the overall energy resolution.

C. Published Papers

C.1 Papers Discussed in Dissertation

- Pan, J.; **El-Ballouli, A. O**.; Rollny, L.; Voznyy, O.; Burlakov, V.; Goriely, A.; Sargent, E. H; Bakr, M. O. "Automated Synthesis of Photovoltaic-Quality Colloidal Quantum Dots using Separate Nucleation and Growth Stages", *ACS Nano*, **2013**, *7*, 10158–10166.
- Bakr, O.; Pan, J.; **El-Ballouli, A. O.;** Knudsen, K. R.; Abdelhady, A. L. "System and method of making quantum dots", *U.S. Patent*, **2015**, WO 2015/075564.
- **El-Ballouli, A. O**.; Alarousu, E.; Bernardi, M.; Aly, S. M.; Lagrow, A. P.; Bakr, O. M.; Mohammed, O. F. "Quantum Confinement-Tunable Ultrafast Charge Transfer at the PbS Quantum Dot and PCBM Fullerene Interface", *JACS*, **2014**, *136*, 6952–6959.
- **El-Ballouli, A. O**.; Alarousu, E.; Kirmani, A.; Amassian, A.; Bakr, O. M.; Mohammed, O. F. "Overcoming the Cut-off Charge Transfer Bandgaps at the PbS Quantum Dot Interface", *Advanced Functional Materials*, **2015**, *25*, 7435-7441.

C.2 Other Paper Contributions

- **El-Ballouli, A. O.**; Alarousu, E.; Usman, A.; Pan, J; Bakr, O. M.; Mohammed, O. F. "Real-Time Observation of Ultrafast Intraband Relaxation and Exciton Multiplication in PbS Quantum Dots", *ACS Photonics*, **2014**, *3*, 285-292.
- Eita, M.; Usman, A., **El-Ballouli, A. O.**; Alarousu, E.; Usman, A.; Bakr, O. M.; Mohammed, O. F. "A Layer-by-Layer ZnO Nanoparticle–PbS Quantum Dot Self-Assembly Platform for Ultrafast Interfacial Electron Injection", *Small*, **2014**, *11*, 112-118.
- Demeler, B.; Nguyen, T. L.; Gorbet, G. E.; Schirf, V.; Brookes, E. H.; Mulvaney, P.; **El-Ballouli, A. O.**; Pan, J.; Bakr, O. M.; Demeler, A.; Uribe, B. H.; Bhattarai, N.; Whetten, R. L. "Characterization of Size, Anisotropy, and Density Heterogeneity of Nanoparticles by Sedimentation Velocity", *Anal.Chem.* **2014**, *86*, 7688−7695.